High Frequency Dynamic Tuning of Photonic Crystal Nanocavities by Means of Acoustic Phonons

Daniel A. Fuhrmann

Dissertation zur Erlangung des Doktorgrades der

Mathematisch-Naturwissenschaftlichen Fakultät

der Universität Augsburg

Universität Augsburg University

nim nanosystems initiative munich

Bayerische Forschungsstiftung

Erster Gutachter: Prof. Dr. A. Wixforth

Zweiter Gutachter: Prof. Dr. J. Finley

Mündliche Prüfung: 24.06.2014

Abstract

This thesis discusses original experiments performed in the context of solid-state cavity quantum electrodynamics (cQED). The manipulation of the resonance condition of a photonic crystal membrane nanocavity coupled to self-assembled InAs quantum dots by a coherent beam of acoustic phonons is demonstrated. Photonic crystals (PC) are artificial materials designed to control the propagation of light and spontaneous emission properties of embedded emitters[1]. The PCs studied here are created by pattering a thin membrane of GaAs with a hexagonal array of holes as shown in Fig. 0.1. A defect in the hole array constitutes a nanocavity which confines light. In analogy to a drum, the resonance of the cavity is defined by its geometry/dimensions and the propagation velocity of light/sound of its medium. Successful approaches of tuning the resonance of a PC cavity include variation of the PC temperature or adsorption of inert gas. These are slow processes, which change the optical properties on a timescale of seconds. For cQED, tuning of the resonance wavelength can be required to match the resonance of an optical emitter. The timescale of intended coupled system is determined by the

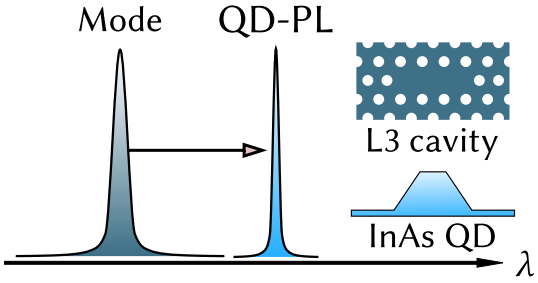

Figure 0.1 – Spectrally tuning the L3 nanocavity mode of a photonic crystal membrane to the wavelength of the quantum dot (QD) photoluminescence (PL). At resonance, the InAs QD, an artificial two-level atom, and the L3 photonic cavity mode form a coherent superposition of quantum states.

spectral lifetime of the emitter ranging in the picosecond regime and the *Q*-factor of the cavity. The *Q*-factor is the measure of the optical confinement quality of the cavity. Here, a fast and efficient tuning mechanism of the PC cavity resonance is presented and investigated enabling high frequency tuning rates while maintaining the cavity *Q*-factor. Electrically generated surface acoustic waves (SAW) deforming the PC membrane are shown to shift the resonance wavelength by more than 8 times its linewidth at a rate of more than 1.7 GHz. Using finite-difference time domain (FDTD) simulation the implications of SAW wavelength and amplitude are investigated focusing on spectral tuning range, spatial mode profile and *Q*-factor. A comparison to a simple model of a Fabry-Perot resonator with variable resonator length is made. Additionally to the fundamental mode of the cavity the effect on higher order cavity modes is studied. Tuning the fundamental mode resonantly pumped through a higher-order mode is evaluated. The simulations show that spectral overlap of a higher order mode with the exciting laser can be maintained while the fundamental mode oscillates over several nanometers.

Experimentally, the SAW tuning mechanism is investigated in time-integrated and time-resolved measurements. In time-integrated measurements the spectral tuning range and optical properties of a cavity for different SAW wavelengths and SAW amplitudes are studied. The experiments show in accordance with the simulation that the spectral tuning range increases linearly with the hole displacement. Moreover, the increased spectral tuning range of shorter SAW wavelengths and the preservation of the *Q*-factor are confirmed. Time-resolved investigations show that the coupling of the emitter and the cavity mode can be tuned within the spectral lifetime of the emitter. The optical density of states available to the emitter is efficiently controlled in the experiments.

Serving as an outlook as well as concluding this thesis the final chapter treats SAW-controlled coupling of two cavities. Evaluating the merits of solid-state cQED in an implementation of on-chip quantum computation[2] the control of the coupling strength of two cavities could serve for routing quantum information. Worldwide research groups are working on the goal of a quantum computer which will dramatically increase computation speed and facilitate new applications.

Contents

Introduction

In 2012 the semiconductor chip maker Intel started selling processors for personal computers with an average half-pitch of 22 nm, i.e. the distance between identical features. The *Tri-Gate* transistor[3] introduced for this processor generation ensures well defined switching behavior by connecting on three sides to the conducting channel. In an ideal field effect transistor the current between source and drain is controlled via the gate voltage depending on the capacitance of the channel. This capacitance is determined by the distance between source and drain and the dielectric properties and thickness of the layer insulating the gate electrode from the conducting channel. The planar transistor has been the standard for mass production of integrated circuits for more than 50 years. Shrinking the lateral size of the transistor causes the switching behavior to be increasingly affected by the drain voltage as the capacitance of the drain becomes comparable to the gate capacitance. The *Tri-Gate* transistor uses a channel protruding from the surface in a ridge which can be connected by the gate on three sides for better control of the conducting channel between source and drain. Smaller feature size not only allows more transistors to be placed on a wafer but also increases the switching frequency and improves power consumption. The International Technology Roadmap for Semiconductors projects a half-pitch of 14 nm to be established by 2014. Compared to the 130 nm technology, which was state of the art in 2000-2001 this is a size reduction of almost an order of magnitude in less than 15 years. As the dimensions decrease in pursue of Moore's law quantum-mechanical effects will be become more important. One path which can be taken to face this challenge embraces the quantum-mechanical nature by encoding information in quantum-mechanical states of photons or atoms. Quantum computing, initially proposed by

Richard Feynman 1982 for simulating quantum systems, and the broader field of quantum information processing have unique properties which are not inherent in classic systems[4]. The classical bit is represented by a switch, e.g. a transistor, either in the '0'- or '1'-position. A quantum bit or qubit is realized by a physical system with two orthogonal states, $|0\rangle$ and $|1\rangle$. Examples are a photon's orthogonal linear polarizations, the spin up and spin down of an electron, or the ground and excited state ($|g\rangle$ and $|e\rangle$) of an atom. The state of the qubit is defined by the system's wavefunction $|\Psi\rangle$ with amplitude coefficients c_0 and c_1:

$$|\Psi\rangle = c_0|0\rangle + c_1|1\rangle \tag{0.1}$$

Coherent superposition of the two states allows the qubit to be in both states at the same time. When looking at a system of two interacting qubits the system can be in a superposition of all four states. To describe the state of this system four amplitude coefficients are needed which store the quantum information. The information needed to describe a system with N interacting qubits is given by 2^N. This exponential increase in information storage is contrary to the linear increase of a classical register. Unfortunately, this wealth of data cannot be read out directly since measurement on any qubit can change the states of the others. The opportunity given by this interaction is massively parallel computing, i.e. 'quantum parallelism'[5]. Consequently, quantum computation can transform tasks which scale exponentially with the number N of inputs on a classical computer into tasks that increase polynomially (N^x) with size. The Deutsch-Jozsa algorithm[6] is a good example for the efficiency of a quantum computer. The task is to determine whether a binary function $f(x)$ is constant, i.e. returns the same result for either binary input, or whether it is balanced. A balanced function will return $f(0) \neq f(1)$. A classical computer needs to perform two calls whereas a quantum computer is able to answer after a single measurement on the superposition of both inputs. Another example is Grover's algorithm[7] which enables a quantum computer to perform a search in a database with N entries much more effective than a classical computer. Grover shows that a quantum computer would need $\sim \sqrt{N}$ operations while the classical counterpart finds the desired entry after $\sim N/2$ operations.
A practical implementation of a quantum computer would need to fulfill the fol-

lowing criteria by D. DiVincenzo[8]:

1. A scalable network of well-defined qubits.
2. Reliable state preparation.
3. The decoherence time needs to be longer than the quantum gate operation time.
4. Demonstration of single- and two-qubit quantum gates.
5. Reliable measurement of the output-state of each qubit.

Single- and two-qubit operation have been demonstrated in several systems, including NMR systems[9], ion traps[10], superconducting systems[11], all-optical systems[12] and solid-state cavity QED systems[13]. Photons easily fulfill the qubit decoherence criterion. The field of astronomical interferometry lives on the fixed phase-relation of light that traveled hundreds of light years. In principle integrated optics, i.e. on-chip photonic devices connected by a network of waveguides[14][15], can be arbitrarily scaled. Furthermore, if light is confined in a cavity with cubic-wavelength volume light-matter interaction is greatly enhanced. Strong interaction between qubits is a prerequisite for working two-qubit gates. As a result semiconductor quantum dot emitters coupled to a photonic crystal membrane nanocavity form a promising platform for quantum information networks and computing[16].

To control the QD-cavity interaction different approaches have been demonstrated. Examples are temperature tuning[17], gas adsorption[18] and by means of electrical fields[19]. A control mechanism for the interaction between emitter and the cavity needs to be effective, i.e. it should detune the cavity and the emitter resonance by several linewidths of the cavity resonance. Moreover, the tuning needs to be fast compared to the timescale of processes in the system, i.e. the radiative lifetime of the excited emitter. In addition, the optical confinement of the cavity should not decrease at best. While striving for efficient spectral tuning the spatial electromagnetic distribution of the cavity mode should not change. Spatial overlap of the emitter and an anti-node of the cavity mode has a strong influence on the

coupling. Clearly, temperature tuning and adsorption of gas can be regarded as quasi-static processes in respect to a radiative emitter lifetime of less than 150 ps corresponding to a spontaneous emission rate of more than 6.5 GHz[20]. In [19] a pair of lateral electrodes integrated around the cavity demonstrated control of the QD emission wavelength via the quantum confined stark effect. A maximum tuning rate of 150 MHz was established limited by the RC constant of the device. In this thesis a tuning mechanism based on surface acoustic waves is introduced fulfilling previously mentioned requirements and demonstrating tuning rates of more than 1.7 GHz. This tuning mechanism is based on mechanical deformation of the photonic crystal membrane by the SAW. The tuning rate has been chosen according to the results of finite-difference time-domain (FDTD) electromagnetic field simulations of the deformed nanocavity and is not limited to this frequency. SAW frequencies of more than 24 GHz are feasible and have been demonstrated[21]. If mechanical modes of the photonic crystal membrane are excited resonantly by the SAW even more pronounced effects are expected. This approach can be extended to coherently control optomechanical crystals[22] based on photonic crystal membranes[23] with SAW. Recent experiments have demonstrated the confinement of optical and mechanical localized modes inside a planar photonic crystal nanocavity[24].

This thesis is structured in the following way: After an introductory part which covers the basic theory on cQED, photonic crystals, self-assembled InAs quantum dots and surface acoustic waves - time-integrated measurements and FDTD simulations will demonstrate the potential of a surface acoustic wave tuning approach. Subsequently, the results of full time domain stroboscopic and time-resolved measurements are presented. Furthermore, an outlook and motivation to potential future experiments with single quantum dots and coupled nanocavities is given. Detailed information on sample preparation and the experimental setup is found in the appendix.

1 Theory: Cavity QED and SAW

1.1 Motivation

Electrodynamics - in a classical picture drawn with the famous Maxwell equations an electromagnetic wave can be pictured having any energy value, i.e. two waves can be found with infinitesimal small difference in frequency. In the quantum picture the granularity of the energy scale of light is defined by $\hbar$. A photon's energy is given by an integer multiple of the Planck constant. The quantum nature of light is even more prominent for light being confined to a resonator. Similar to a musical instrument the geometry of the body, i.e. the acoustic cavity, defines and limits the range of tones which can be produced. Likewise, the electromagnetic modes of an optical cavity show a geometry-dependent frequency spectrum, i.e. the density of optical modes depends on the size of the resonator. The density of optical modes differs from the free space distribution. Consequently, the decay dynamics, i.e. the rate of spontaneous emission, of an emitter (e.g. an atom) inside a cavity change proportionally. At the resonance energy of the cavity the density of modes exceeds the free space state. Hence, the spontaneous emission rate increases if the transition energy of the emitter coincides. For the description of the spontaneous emission dynamics of an emitter it is necessary to describe the emitter within its environment. As the optical emitter returns to its ground state inside the cavity the emitted photon can be confined for several optical periods and ultimately re-excite the emitter. This reversible and coherent process occurs when the emitter-light coupling strength exceeds the loss rate of the cavity and the non-radiative decay rate of the emitter. This is the prerequisite for the so-called strong-coupling regime of cavity quantum electrodynamics (cQED). The

frequency with which cavity and emitter exchange energy, the vacuum Rabi oscillations, is referred to as the Rabi frequency. It is the difference of the quantum entangled atom-cavity eigenfrequencies and will be described in more depth in the next chapter. The multitude of different systems in which these effects are investigated stem from research efforts of the past decades. Initial observation of strong coupling of single Cs atoms to a mode in high finesse macroscopic Fabry-Perot resonators[25] were followed by solid-state systems with atom-like emitters, i.e. InAs quantum dots (QD), in nanometer-scale cavities. Fabry-Perot type cavities implemented by epitaxially grown distributed Bragg reflectors or highly reflective mirrors for coupling of ultra-cold atoms, etched microdiscs, microspheres, microtoroids and photonic crystal nanocavities are notable examples (see Fig. 1.1).

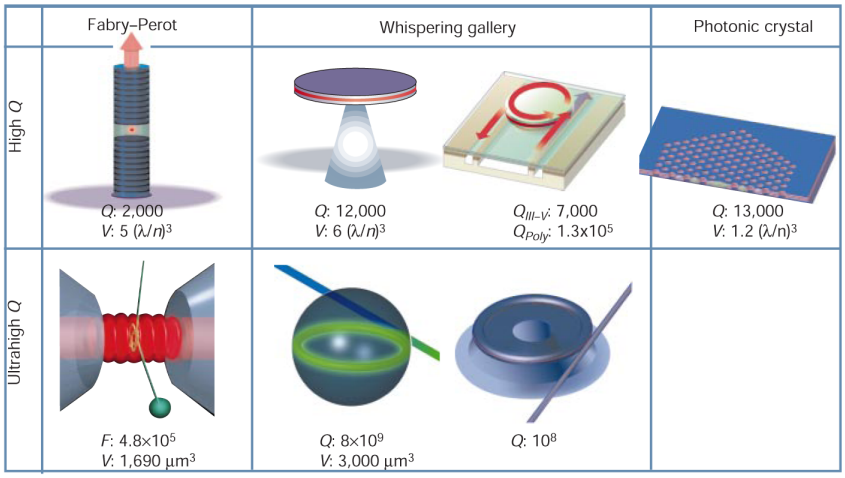

Figure 1.1 – Strong coupling and cQED applications are investigated in various implementations. This figure, taken from [26], displays prominent variants of optical microresonators, i.e. micropost, microdisk, polymer add/drop filter, photonic crystal cavity (upper row) and Fabry-Perot bulk optical cavity, microsphere, microtoroid (lower row). The *Q*-factor and the finesse *F* are proportional to the number of oscillations of the electromagnetic field while the cavity confines a photon. For smaller cavity volumes, expressed in multiples of the cubic resonance wavelength in the medium, light-matter interaction is intensified.

Targeting integrated implementations of combined photon generation and manipulation using light-matter interaction photonic crystal membrane (PCM) nanocav-

ities have been chosen by many research groups as the preferred platform. PCM processing is compatible with established planar wafer processing methods. Furthermore, the resonance wavelength of photonic crystal nanocavities is easily tailored to match the desired wavelengths, e.g. those relevant for optical transmissions used in telecommunication. Combined with InAs QDs grown in a GaAs-matrix emitting in the near-infrared part of the electromagnetic spectrum this platform offers promising potential. QDs are two-level emitters with optical properties also observed for single atoms (see Chap. 1.4). Accordingly, in the following general description of cQED the term 'QD' is used interchangeably with the concept of a single two-level emitter. This thesis as well as the experiments and simulations performed in its context focus on this platform. The description of the properties and prospects of a tunable and highly dynamic optical resonator using surface acoustic waves (SAW) is preceded by the introduction of cQED and the individual building blocks, i.e. photonic crystals and QDs as well as SAW.

1.2 Cavity Quantum Electrodynamics

The ”Dressed-Atom-Model” or ”Jaynes-Cummings-Model”[27] presented in the following chapter not only applies to the system studied here but can be applied to all emitters inside a resonator, e.g. an ultra-cold atom optically trapped. The photonic crystal cavity membrane (PCM) nanocavity mode and the two-level system of a quantum dot are both quantum mechanical systems. Thus a combination of both exhibits new qualities which are not just the sum of the individual contributions.

1.2.1 Emitter-cavity coupling

An excited two-level emitter inside an optical cavity returns to the ground state by emitting a photon. The emitter is perfectly aligned with an anti-node of the electric field inside the cavity. If the emitter's transition energy is not in resonance with one of the cavities resonant modes the photon is lost. In case of resonance the photon is either confined inside the cavity long enough for the emitter to be excited again. In this scenario the system is in the regime of strong coupling. In the weak coupling regime the photon is not confined long enough to re-excite the emitter and eventually escapes the cavity.
The coupling regime of the system depends following parameters:

- κ: the cavity decay rate
- γ: the non-resonant emitter decay rate
- g_0: emitter-photon coupling rate

Theses parameters determine how fast energy is dissipated from the emitter-cavity system and how the photon emission rate of the emitter is altered due to the presence of the cavity (see Fig. 1.2).
The cavity photon decay rate κ quantifies the losses of the cavity. For a planar cavity consisting of two opposing mirrors this rate is equal to the spectral width of the mode $\Delta\omega$. κ is inversely proportional to the quality factor Q. The Q-factor

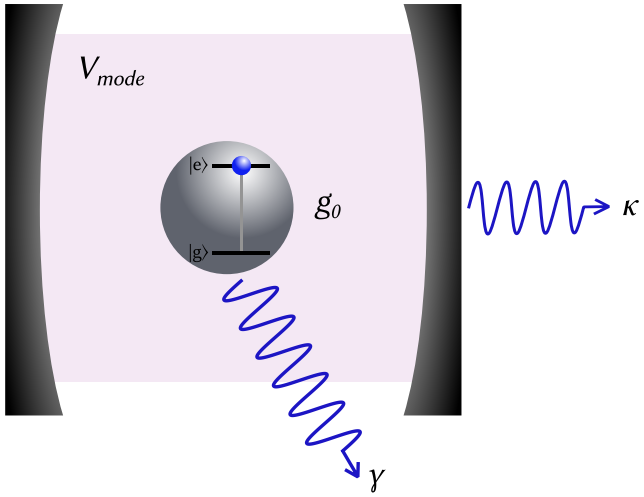

Figure 1.2 – Schematic depiction of the loss rates of cavity and emitter: Cavity decay rate κ and the non-resonant emitter decay rate γ. g_0 is the emitter-photon coupling rate quantifying the interaction between emitter and the light field with mode volume V_{mode}.

is proportional to the number of oscillations of the electromagnetic field while the cavity confines a photon.

$$Q = \frac{\omega}{\Delta\omega} = \frac{\omega}{\kappa} \tag{1.1}$$

Here, ω denotes the angular frequency of the mode. A cavity with a high Q-factor will exhibit a low loss rate. The non-resonant decay rate of the emitter γ quantifies any transition of the emitter from an exited state $|e\rangle$ to its ground state $|g\rangle$ not affected by the cavity. These processes include the non-radiative decay and transitions which are not in resonance with cavity mode. Emission in a direction of low cavity confinement will also contribute to the non-resonant decay rate.

The emitter-photon coupling rate g_0 is a measure of the interaction between the emitter and the vacuum field inside the cavity. It is therefore dependent on the alignment of electric dipole moment μ in respect to the cavities electromagnetic mode profile[28]:

$$g_0 = \left(\frac{(\mu_{eg})^2\omega}{2\epsilon_0\epsilon_r\hbar V_{mode}}\right)^{\frac{1}{2}} \tag{1.2}$$

$\mu_{eg} = -e\langle e|x|g\rangle$ is the electric dipole matrix element of the emitter's transition from the excited state to the ground state for the cavity polarization. ϵ_0 and ϵ_r are the electric constants of the vacuum and the cavity material. V_{mode} is the mode

volume of the mode with angular frequency ω. Essentially g_0 describes the interaction of the emitter with the vacuum energy of the electro-magnetic field inside the cavity E_{vac}. The interaction energy is given by:

$$\Delta E_{vac} = \hbar g_0 \propto \frac{1}{V_{mode}} \tag{1.3}$$

A small mode volume V_{mode} is required for strong light-matter interaction. The mode volume is given by[29]:

$$V_{mode} = \frac{\int \epsilon(\vec{r})|E(\vec{r})|^2 \, d^3\vec{r}}{max(\epsilon(\vec{r})|E(\vec{r})|^2)} \tag{1.4}$$

where $E(\vec{r})$ is the electric field and $\epsilon(\vec{r})$ the refractive index at the position $\vec{r}$. The mode volume is measured in cubic mode half-wavelengths in the solid, i.e. $(\lambda_c/n)^3$ with n being the refractive index of the cavities medium. With Q being determined by the cavity loss rate (see Eq. 1.1), the ratio of Q/V_{mode} quantifies the cavity interaction strength. A high Q/V_{mode} ratio is therefore the key goal of cavity design and processing.

The emitter-photon coupling rate g_0 will have to exceed the non-resonant emitter decay rate and the cavity loss rate for a photon to re-excited the resonant emitter coherently. This condition distinguishes the system's coupling regimes:

(i) $g_0 > \gamma, \kappa$: strong coupling

(ii) $g_0 < \gamma, \kappa$: weak coupling

The emitter-cavity system investigated experimentally in this thesis is in the weak coupling regime since condition (ii) applies: $g_0 < \kappa$. Under these conditions the emitter's relaxation is irreversible. The Purcell effect[30] is a consequence of the weak coupling regime. This effect describes an increased recombination rate, i.e. a shortened spectral lifetime, of an emitter inside a resonator. According to Fermi's Golden Rule (see Eq. 1.5), the excited two-level emitter can only return to the ground-state if photonic states $D(\omega)d\omega$ are available for the photon with energy $\hbar\omega$ generated in this process. $D(\omega)$ is the photonic density of states (DOS) which is $\propto \omega^2$ in free space. The transition rate W_{cav} is[28]:

$$W = \frac{2\pi}{\hbar}|M_{ge}|^2 D(\omega) \tag{1.5}$$

$M_{g\,e} = \langle e|H'|g\rangle$ is the matrix element of the transition between the ground and the excited state caused by perturbation H', i.e. the interaction of the emitter and a photon in the cavity. No states are available for transistion frequencies which are not in resonance with the cavity modes[31]. A Lorentzian describes the DOS around the cavity mode's angular frequency ω_c:

$$D(\omega) = \frac{2}{\pi\Delta\omega_c}\frac{\Delta\omega_c^2}{4(\omega-\omega_c)^2+\Delta\omega_c^2} \tag{1.6}$$

If the emitter's angular frequency ω_{QD} coincides with the mode the density of states is:

$$D(\omega_{QD}) = \frac{2}{\pi\Delta\omega_c} = \frac{2Q}{\pi\,\omega_{QD}} \tag{1.7}$$

The number of states available in resonance is proportional to the Q-factor. The Purcell factor F_p is the rate of spontaneous emission of the emitter inside the cavity W_{cav} in respect to the rate in vacuum W_{vac} [28]:

$$F_p = \frac{W_{cav}}{W_{vac}} = \frac{3Q}{4\pi^2 V_0}\frac{|\vec{p}\cdot\vec{\mathrm{E}}|}{|\vec{p}||\vec{\mathrm{E}}|}\frac{\Delta\omega_c^2}{4(\omega_{QD}-\omega_c)^2+\Delta\omega_c^2} \tag{1.8}$$

The Purcell factor's dependence on the alignment of the emitter's dipole and the vacuum field E is expressed by the normalized dipole orientation factor ξ:

$$\xi = \frac{|\vec{p}\cdot\vec{\mathrm{E}}|}{|\vec{p}||\vec{\mathrm{E}}|} \tag{1.9}$$

In the case of resonance and perfect alignment of dipole along the field Eq. 1.8 becomes:

$$F_p = \frac{3Q}{4\pi^2 V_{Mode}} \tag{1.10}$$

A fast recombination rate of the emitter can thus be achieved by optimizing the cavity's quality factor and reducing the mode volume. The Purcell effect can allow an emitter, i.e. a QD (see Chap. 1.4), to recombine faster than its dephasing time which is important for the efficiency of the emitter as a light source, e.g. single photon sources[32]. Likewise, laser application benefit from the control over the spontaneous emission. By suppressing spontaneous emissions which are not coupled to the lasing mode ultra-low lasing thresholds are realized[33]. Another

benefit from placing the emitter inside a cavity is that the losses are direction-dependent. Suppression of light propagation in the horizontal plane of the cavity causes the emission to be redistributed in the vertical direction. The control of the emission direction allows for optimized LEDs and solar cells.

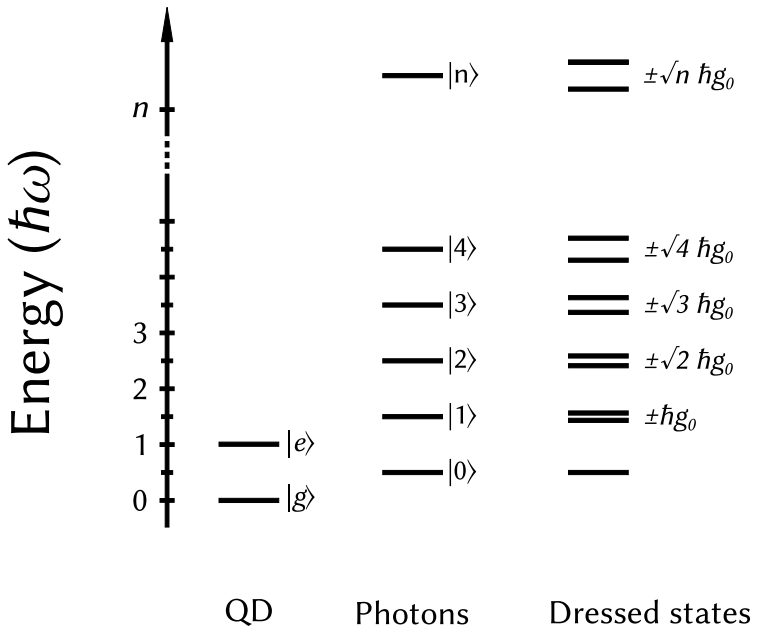

Figure 1.3 – The formation of the dressed states, i.e. the Jaynes-Cummings ladder, is the consequence of the strong coupling between QD and cavity.

When the losses of the cavity and the emitter are smaller than the coupling constant g_0 they are strongly coupled. The coupled system is described as that of two coupled harmonic oscillators. The bare states of the uncoupled system $\Psi = |\Psi_{QD}, n\rangle$ are defined by the state of the emitter Ψ_{QD} and the number of photons n. The ground state $\Psi_0 = |g; 0\rangle$ of the coupled system describes a QD in the ground state and no photons in the cavity. The ground state has the energy of $E_0 = \frac{\hbar\omega}{2}$ because of the zero-point energy of the vacuum field in the cavity. ω describes the cavity resonance frequency as well as the transition energy $\hbar\omega$ of the QD. The excited states are doubly degenerate. The excited states of the first manifold of the Jaynes-Cummings ladder are $|g; 1\rangle$ and $|e; 0\rangle$ with one photon in the cavity and a QD in the ground state and no photon in the cavity and an excited emitter respectively (see Fig. 1.3). The first excited dressed state is:

$$\Psi^{\pm} = \frac{1}{\sqrt{2}}(|g; 1\rangle \mp |e; 0\rangle) \tag{1.11}$$

With the eigenenergies of:

$$E_1^{\pm} = \frac{3}{2}\hbar\omega \pm \hbar g_0 \tag{1.12}$$

The term *dressed* refers to the coupling of the single systems' bare states. The Jaynes-Cummings model[27] describes the formation of a quasi-particle, i.e. a polariton. In the strong coupling regime with emitter and the cavity mode in perfect resonance their individual states can no longer be distinguished. The system is in a state of coherent superposition, it oscillates between two new states with an energy difference of $\Delta E_n = 2\sqrt{(n)}\hbar g_0$, the vacuum Rabi splitting[34]. Spectrally the strongly coupled system features a double peak with a splitting of ΔE_n. If either of the two, i.e. mode or emitter, is spectrally tuned through the resonance of the other the emission lines will not cross (see Fig. 1.18). This anti-crossing is an indicator of the strong coupling regime.

1.2.2 The planar cavity

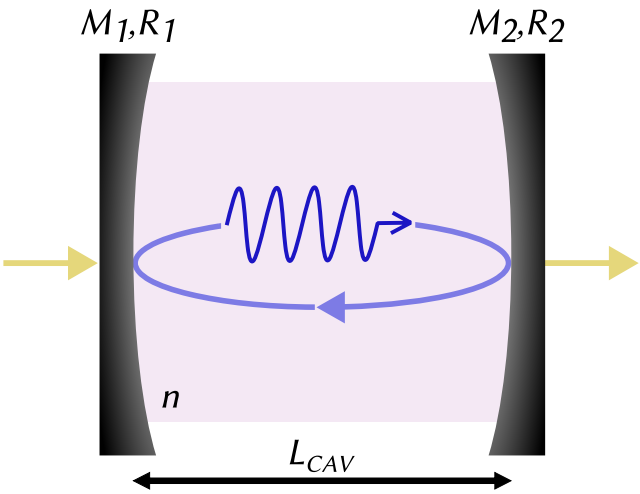

Figure 1.4 – The one dimensional cavity consists of two mirrors M_1 and M_2 with reflectivity R_1 and R_2 separated by L_{CAV}. The medium inside the cavity has the refractive index n.

The Fabry-Perot resonator or planar cavity depicted in Fig. 1.4 not only serves as a good example of a generic cavity. Moreover, the findings of tuning photonic crystal membrane nanocavities with surface acoustic waves can be related to such a resonator with oscillating length $L_{CAV}(t) \propto sin(\omega_{SAW}t)$ which will be discussed

in Chap. 3.2. Light inside a planar cavity with cavity length L_{CAV} is reflected at either side by mirrors M_1 and M_2 with reflectivity R_1 and R_2.

If integer multiples m of the half-wavelength $\frac{\lambda}{2}$ of the light fit inside the cavity the resonance condition $m\frac{\lambda}{2} = nL_{cav}$ is fulfilled. m is the index of the mode whereas n denotes the refractive index of the cavity medium. The modes ($m = 1, 2, 3, ..$) of the lightfield are in phase after every round-trip in the cavity. Therefore, the light of these resonant modes interferes constructively. Light which does not fulfill the resonance condition will have significant lower amplitudes. A prime example of such an optical resonator is found in every laser in which the resonator length determines the energy of the photons emitted. The transmission through the cavity is given by the Airy function[35]:

$$T = \frac{1}{1 + (4F^2/\pi^2)sin^2(\Phi/2)} \tag{1.13}$$

in which F is the finesse of the cavity depending on the mirror reflectivity R_1 and R_2.

$$F = \frac{\pi(R_1R_2)^{1/4}}{1 - \sqrt{R_1R_2}} \tag{1.14}$$

The transmission will be unity if the resonance condition is met, i.e. the round-trip phase shift is:

$$\Phi = \frac{4\pi nL_{cav}}{\lambda} = 2\pi m \tag{1.15}$$

Light not fulfilling the resonant condition will interfere deconstructively. In this case the probability of leaving the cavity is small. Fig. 1.5 depicts the transmission spectrum of the cavity with finesse $F = 40$. The full width at half maximum $\Delta\Phi_{FWHM}$ of the maxima of the transmission spectrum depends on the finesse:

$$\Delta_{FWHM} = 2\pi/F \tag{1.16}$$

The angular frequency of the resonant modes $\omega_m = m\frac{\pi c}{nL_{CAV}}$ are given by the dispersion relation $2\pi c = \lambda\omega$ with c being the speed of light inside the cavity. The spectral width $\Delta\omega$ relates to the properties of the cavity, i.e. the finesse and cavity length L_{CAV} via:

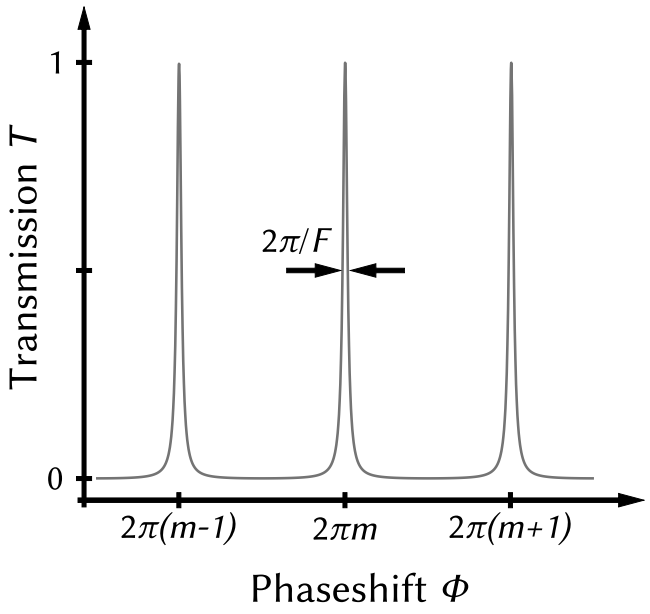

Figure 1.5 – Transmission through a Fabry-Perot resonator. The finesse F depends on the reflectivity of cavity mirrors.

$$\Delta\omega = \frac{\pi c}{nFL_{CAV}} \tag{1.17}$$

$\Delta\omega$ is a measure of how fast photons are lost from the cavity equal to the cavity decay rate κ[28]. An equivalent and common figure of merit for the optical quality of a cavity is the Q-factor (Eq. 1.1).

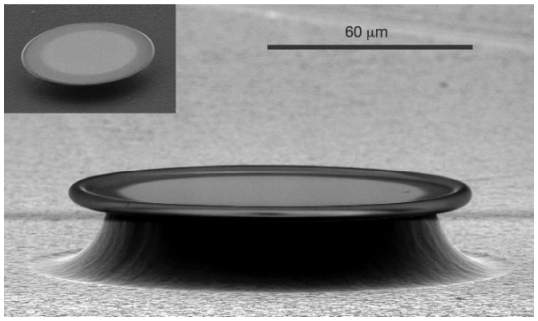

Figure 1.6 – Silica microtoriod resonators exhibit whispering gallery modes with ultra-high Q-factors ($Q \approx 10^8$). (Picture from [36])

Different implementations of optical cavities have been investigated experimentally. A Fabry Perot resonator is created by stacking layers of different semiconductors by molecular beam epitaxy (MBE). Distributed Bragg reflectors (DBR) are grown on either side of the cavity layer. DBRs work based on reflections at the

interface of materials with different refractive index (see next chapter). Light of wavelength inside the stop bands of the DBR is confined in the cavity for cQED experiments[37]. The use of microdiscs and microtoroids follows a different design. These disc-shaped resonators made of a dielectric material (e.g. SiO_2) with diameters one order of magnitude larger than the wavelength of the confined light circulate photons by means of total internal reflection (see Fig. 1.6). These photonic whispering gallery modes are excited by coupling the microdisk or microtoriod to the evanescent light of a tapered fiber placed next to the resonator[36].
A sophisticated approach to control the propagation of light in solids are the photonic crystals introduced in the next section.

1.3 Photonic crystals

Proposed in the late 1980's by Eli Yablonovic and Sajeev John ([1], [38]), photonic crystals are created by the periodic variation of the refractive index in one or more dimensions. Bragg-reflections at material interfaces and the resulting interference restrict the propagation of light to certain wavelengths and directions. Nature offers many examples where colorful appearance is created by constructive and destructive interference of light. These colors are not perceived because of absorbing dyes or pigments but stem from variations of the refractive index in stacked layers or complicated three dimensional periodic structures. Abalone shells, peacock feathers, beetles and butterflies[39] are prominent examples. Here, the refractive index varies on the order of the light's wavelength. The perceived colors are dependent on the angle of observation. Thin films of fluids show a beautiful display of colors when looking for example at oil spills or soap bubbles (Fig. 1.7(a)).

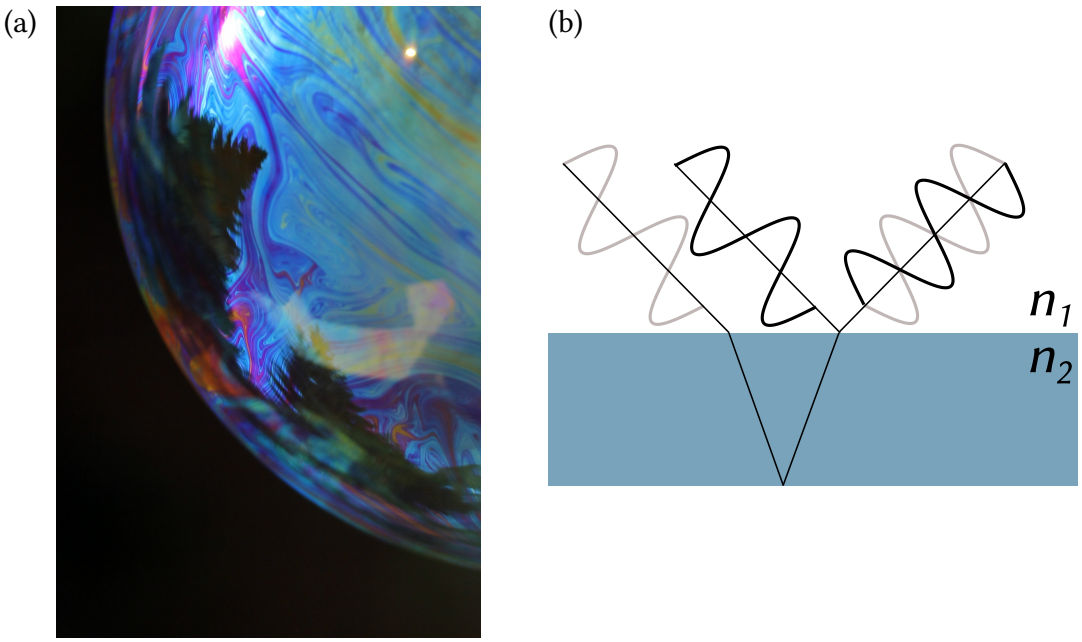

Figure 1.7 – (a) Vivid colors reflected by the thin film of a soap bubble. (b) Destructive interference of monochrome light reflected by a high index material ($n_1 < n_2$).

Fig. 1.7(b) illustrates how monochromatic light interferes destructively. When the light wave is reflected by the high index material it experiences a phase shift of

π. The light which enters the film and is reflected on the other side of the film has to travel a longer optical path d depending on the angle of incidence. If the wavelength of the light corresponds to the optical path difference $d = \lambda$ the light interferes destructively with light reflected directly at the surface. If the thin film is irradiated with white light the observer will perceive a red-orange color when blue light cancels itself out. Blue is perceived when observing the film under a different angle under which red light interferes destructively. Structural colors can be created by arranging nanoparticles or -structures in a periodic fashion. An elegant way has been demonstrated by [40] which allows for magnetic control of the distance between nanoparticles (see Fig. 1.8).

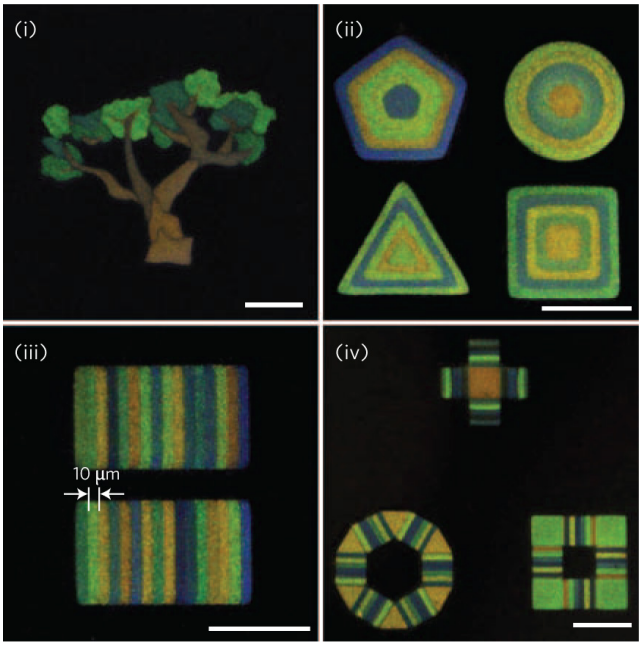

Figure 1.8 – Structural colors produced by magnetically arranged magnetite nanocrystals capped with silica shells ((ii), (iii) scale bars are 100 μm; (i) and (iv) 250 μm; from [40])

In a dielectric medium without free charges and zero current density the macroscopic Maxwell equations describe the propagation of light:

$$\begin{aligned} \nabla \cdot \mathbf{H}(\mathbf{r}, t) &= 0 \\ \nabla \cdot [\epsilon(\mathbf{r})\mathbf{E}(\mathbf{r}, t)] &= 0 \\ \nabla \times \mathbf{E}(\mathbf{r}, t) + \mu_0 \frac{\partial \mathbf{H}(\mathbf{r}, t)}{\partial t} &= 0 \end{aligned}$$

$$\nabla \times \mathbf{H}(\mathbf{r},t) - \epsilon_0 \epsilon(\mathbf{r}) \frac{\partial \mathbf{E}(\mathbf{r},t)}{\partial t} = 0 \tag{1.18}$$

$\mathbf{E}$ and $\mathbf{H}$ are the macroscopic electric and magnetic fields, ϵ_0 is the permittivity of vacuum. Considering linear materials the electric field $\mathbf{E}$ is related to the displacement field via $\mathbf{D}(\mathbf{r}) = \epsilon_0 \epsilon(\mathbf{r}) \mathbf{E}(\mathbf{r})$ omitting higher order terms. The dielectric constant $\epsilon(\mathbf{r}, \omega)$ is assumed to be constant over the range of frequencies to be considered. Another approximation is made by setting the relative magnetic permeability $\mu(\mathbf{r}) = 1$ so that the magnetic induction field $\mathbf{B} = \mu_0 \mathbf{H}$. When expanding $\mathbf{E}$ and $\mathbf{H}$ into a set of harmonic modes the spatial and time dependence can be separated:

$$\begin{aligned} \mathbf{H}(\mathbf{r},t) &= \mathbf{H}(\mathbf{r}) e^{i\omega t} \\ \mathbf{E}(\mathbf{r},t) &= \mathbf{E}(\mathbf{r}) e^{i\omega t} \end{aligned} \tag{1.19}$$

While the first two equations in Eq. 1.18 demand that the electromagnetic waves are transverse the remaining two can be combined to result in:

$$\begin{aligned} \nabla \times \left(\frac{1}{\epsilon(\mathbf{r})} \nabla \times \mathbf{H}(\mathbf{r}) \right) &= (\frac{\omega}{c})^2 \mathbf{H}(\mathbf{r}) \\ \Theta \mathbf{H}(\mathbf{r}) &= (\frac{\omega}{c})^2 \mathbf{H}(\mathbf{r}) \end{aligned} \tag{1.20}$$

The task of determining the electromagnetic fields in a dielectric material with a given dielectric constant $\epsilon(\mathbf{r}, \omega)$ is being reduced to this eigenvalue problem[41]. The solutions of this master equation are the electromagnetic harmonic modes for a dielectric medium. The dielectric structures investigated in this work will exhibit dielectric constants with values alternating in two dimensions. This periodicity causes the master equation to have no real solutions for a finite range of frequencies referred to as the photonic bandgap. In a solid state crystal the atoms are periodically arranged in a lattice constituting a periodic potential landscape $V(\mathbf{r})$. The periodicity is on the same order of magnitude as the *de Broglie* wavelength of the electron. At the boundaries of the Brillouin zone, i.e. $k = \pm \pi / a$ (a is the lattice constant of the crystal) the solution of the Schrödinger equation for an electron are standing waves, i.e. waves that do not propagate. The result of $V(\mathbf{r})$ are gaps in the electronic band structure $\omega(k)$. For certain wave vectors k exist no solution with angular frequency ω. Such gaps are also found in the photonic band structure

of light for dielectric materials with a periodic variation of the dielectric constant $\epsilon(\mathbf{r})$. The periodicity of $\epsilon(\mathbf{r})$ determines the center-frequency of the bandgap, as the lattice constant does in the case of a crystal. In analogy to solid state crystals these materials are referred to as photonic crystals. The center-frequency can be scaled with the dimensions of the photonic crystal. In one dimensional (1D) photonic crystals the dielectric constant varies in one dimension, e.g. a multi-layered film of alternating materials. Light within the photonic bandgap cannot propagate along this direction and will be reflected. Such structures have found applications as optical filters and high reflectivity mirrors for example in vertical cavity surface emitting lasers (VCSELs).

The photonic crystal's equivalents to the conduction and valence band of the solid state crystal are the air band and the dielectric band, respectively. The modes in the dielectric band below the photonic bandgap are more concentrated in the material with high refractive index lowering their frequency in respect to the air band modes. Detailed descriptions on the formation of the optical bandgap can be found in [29] and [41]. A 2D photonic crystal has alternating high and low refractive index in two dimensions and is homogeneous in the third. This is for example realized by growing columns of a non-absorbing material or by etching holes into a dielectric material, e.g. in a hexagonal lattice as shown in Fig. 1.9. The refractive index of the dielectric material relative to the refractive index of air determines the width of the photonic bandgap. The optical modes can be distinguished by their polarization. Transverse-magnetic (TM) modes have **E** normal to the plane of periodicity and **H** in the plane. For transverse-electric (TE) modes **H** is normal to the plane and **E** is parallel. A square array of dielectric columns will only exhibit a photonic bandgap for TM modes whereas a triangular air hole array has a photonic bandgap for both polarizations.

In order to control light propagating in arbitrary directions, the refractive index has to change in every dimension. 3D photonic crystals like the inverse opal structure (see Fig. 1.10) or the woodpile structure [43] have a complete bandgap in all directions. These 3D structures require advanced processing techniques[44] and cannot be easily realized with standard planar processing/lithography. For achiev-

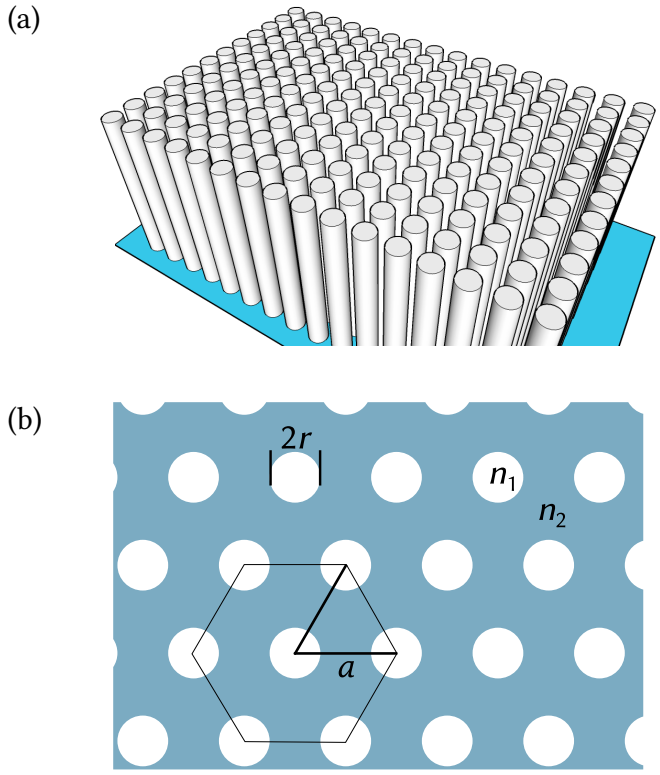

Figure 1.9 – (a) 2D array of dielectric columns in air. (b) Triangular lattice of air holes ($n_1 = 1$) with radius r and lattice constant a in a dielectric material with refractive index n_2.

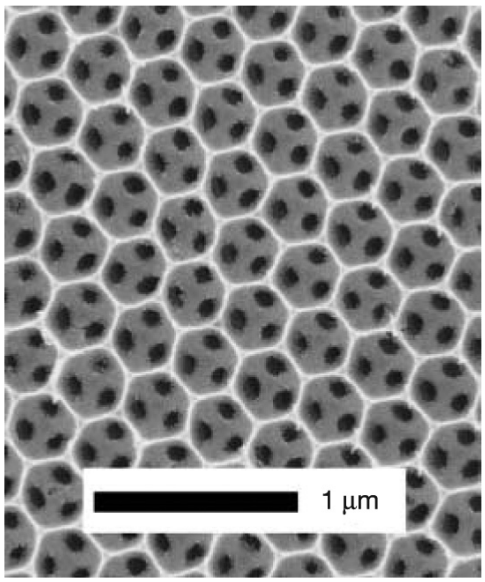

Figure 1.10 – SEM picture of a titania inverse opal from [42].

ing 3D confinement in a 2D photonic crystal total internal reflection (TIR) is used. A photonic crystal membrane (PCM) is a 2D air hole array fabricated on a thin membrane which serves as a planar waveguide (see Fig. 1.11). Light will be confined inside the membrane (refractive index n_2) if it hits the interface to the air cladding ($n_1 = 1$) at an angle below the critical angle $\theta_c = sin^{-1}(n_1/n_2)$ described by Snell's law. In other words, due to the conservation of the wavevector component parallel to the membrane $k_{||}$ light with an inplane-wavevector component $k_{||} > (2\pi/\lambda_{air})$ is confined to the membrane by TIR. Photonic crystal membranes

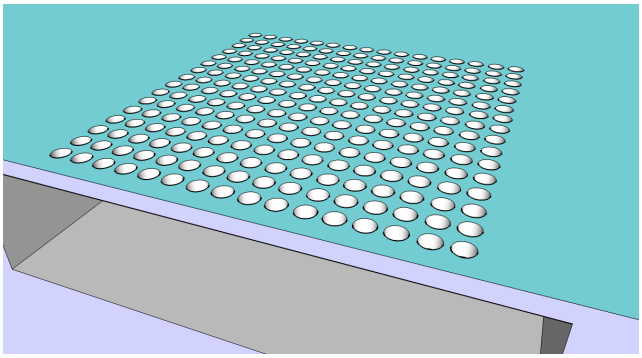

Figure 1.11 – Photonic crystal membrane: Cubic air hole lattice in a thin membrane for index guiding.

do not exhibit a complete photonic bandgap. Similar to light escaping from sharply bent optical fibers light impinging on the membrane-air interface at an abrupt angle couples to extended modes propagating in air. Consequently, the modes guided by TIR only exist outside the so called light cone ($\omega \geq ck_{||}$). In analogy to 2D photonic crystals the modes of the dielectric and air band are distinguished into two polarizations. For *TE-like* modes the electric field is mostly parallel to a symmetry plane while being mostly perpendicular for *TM-like* modes depending on the distance normal to the plane[41]. In the experiments and simulations presented in this thesis photonic crystal membranes with a hexagonal lattice of airholes are investigated. This kind of PCM exhibits a photonic bandgap for TE-like modes but not for TM-like modes. As the light of the solid state emitters (see Chap. 1.4 on InAs quantum dots) incorporated into the membrane is primarily TE-polarized it will be subject to the photonic bandgap. PCMs have been successfully used in order to realize photonic devices controlling spontaneous emission[20] for low-

threshold laser applications[33]. They have also been investigated in the context of cavity quantum electrodynamics[18] described in Chap. 1.5. The PCM devices investigated in this thesis are based on GaAs. The next chapter covers important aspects on an optical quantum emitter compatible with this material system, the InAs quantum dot.

1.4 InAs quantum dots

A Quantum Dot (QD) is a semiconductor nanostructure with three-dimensional confinement for charge carriers. The length scale to which the charge carriers are confined to is smaller than the *de Broglie* wavelength resulting in quantum effects. Most prominent is the complete discretization of the density of states also observed in single atoms. This property accounts for QDs being referred to as artificial atoms. QDs can be created electro-statically by applying a voltage across a two dimensional electron gas, by self-assembly using colloidal synthesis or epitaxial growth. For the samples used in this work the latter is employed to grow InAs islands by molecular beam epitaxy (MBE) embedded in a GaAs matrix creating chemically stable quantum emitters. Due to the lattice mismatch of 7% relative to GaAs the layers of InAs are strained when grown on a GaAs substrate. For a

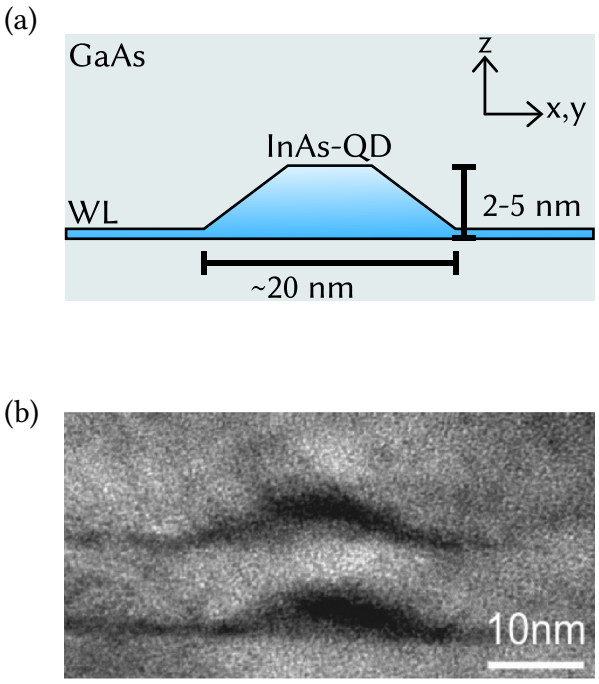

Figure 1.12 – (a) Schematic of a self-assembled InAs QD and wetting layer (WL) embedded in GaAs (z is the growth direction). (b) TEM image of two QDs stacked in growth direction (from [45]).

critical thickness of InAs (approx. 1-4 monolayers[46] depending on the composition) a relaxation of this strain is energetically favorable by forming small islands in comparison to the surface free energy of a full layer. This Stranski-Krastanov

growth mode creates small islands which have a lateral size of $20 - 25$ nm and are $2 - 5$ nm in the growth direction[46][47] (see Fig. 1.12). Due to the bandgap offset and bandgap difference between GaAs ($E_g(T = 300\ \mathrm{K}) = 1.43$ eV) and InAs ($E_g(T = 300\ \mathrm{K}) = 0.36$ eV) a three-dimensional attractive potential for charge carriers is created inside the GaAs matrix as depicted in Fig. 1.13.

The lateral dimensions and thickness of the QDs as well as the thickness of the wetting layer are controlled during growth (e.g. by temperature and material flow). The wetting layer is a thin InAs Quantum Well (QW) of few monolayers which adheres to the GaAs substrate after the formation of the InAs islands. To avoid coupling to optically active InAs surface states the QDs are capped with GaAs. The charge carriers are most effectively confined in the z-direction. The single particle energy states are equidistant as for an electron in a QW (i.e. a particle in a box). In the simple model used here this state can be treated as an energetic offset. The confinement in the plane is comparably weaker. For electrons and holes using

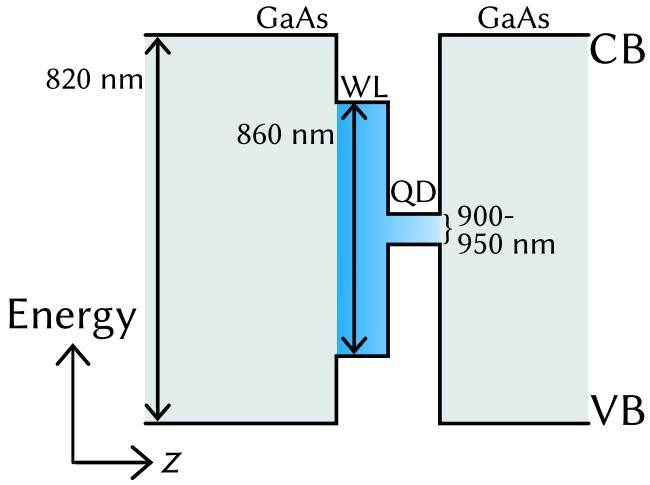

Figure 1.13 – Bandgap diagram of self-assembled InAs QDs in GaAs. The transition wavelengths are indicated. For the WL and the QD these depend on the actual thickness and size. In the experiments the QDs are non-resonantly excited via the wetting layer by a diode laser with $\lambda_{laser} = 855$ nm.

single band approximation the energy levels are that of a two dimensional radial symmetric harmonic oscillator with quantum numbers m and n ($m, n = 0, 1, 2, ...$). The electron eigenstates are $|mn\rangle$ and angular momenta are given by $L_{mn} = m - n$.

The energy levels are:

$$E_{m,n} = \hbar\omega(m + 1/2) + \hbar\omega(n + 1/2) \tag{1.21}$$

The energy levels are degenerate and labeled by adding the quantum numbers m and n. In analogy to atomic physics the energy levels are referred to as shells and labeled s,p,d,f(...). The Pauli exclusion principle allows two charged particles with opposite spin to occupy each level. The s-shell can therefore be populated by two electrons resulting in two dipole-allowed transitions. The energy spacing between s- and p-shell depends on size, strain, and In-content of the dots. For strained $In_{0.5}Ga_{0.5}As$ an energy difference of 41 meV has been reported[48]. In the photoluminescence experiments performed for this work the QDs are populated with charge carriers by non-resonant optical excitation with a laser creating free charge carriers in the wetting layer. The experiments are executed at cryogenic temperatures in order to avoid non-radiative decay. The charge carriers will dissipate

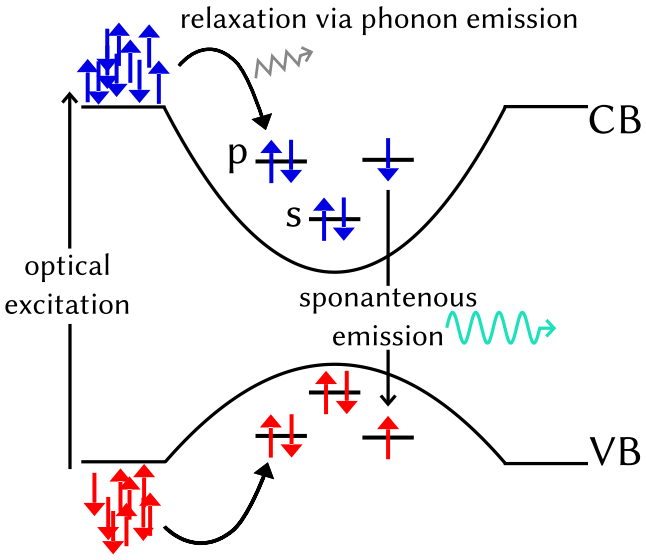

Figure 1.14 – Schematic depiction of the capture of charge carries into the parabolic potential of the QD. The charge carriers relax via phonon emission into the free quantum level with the lowest energy. After the spectral lifetime the charge carriers recombine emitting a photon.

excess energy by coupling to phonons in order to occupy the lowest free energy level in the QD within a few ps[49] as schematically illustrated in Fig. 1.14. With increasing excitation power density more charge carriers are generated populating

higher energy shells. After the spectral lifetime the charge carriers recombine by spontaneous emission of a photon with energy $\hbar\omega = E_i - E_f$, i.e. the energetic difference between the initial state E_i and the final state E_f. The lifetime depends on the number of photonic states available and adheres to Fermi's Golden rule[28]. In the experiments presented here, the spectral lifetime is measured to be $\tau = 1 - 2$ ns (see Chap. 4.2). As in bulk semiconductors electron and hole are bound by the Coulomb interaction. When one electron and one hole are present in the QD a so called neutral exciton ($X^0 = 1e + 1h$) is formed. The QD system will return to its ground state by emission of a photon with the energy of the single neutral exciton E_{X^0} which is the energy difference of electron and hole in the s-shell minus the exciton binding energy. Due to the confining potential of the QD these quasiparticles are bound more strongly compared to the bulk semiconductor. Thus, if the QD is excited once more within the exciton's lifetime, another exciton with orthogonal polarization is generated and the QD is in the biexcitonic state (XX). The consequence is that the photon emitted from this charge configuration has a different energy E_{XX}. Depending on a previous charge of the QD photons can be emitted at E_{X^+} or E_{X^-} for a positively or negatively charged exciton respectively.

Due to the three-dimensional confinement the QD's resonances are spectrally sharp justifying the term 'artificial atom'. Another feature common with single atoms is the QD's emission of single photons. In contrast to classical light sources emitting several photons instantaneously (bunched) single photon sources generate individual (anti-bunched) and indistinguishable photons[28]. The samples which are used in the experiments presented here contain a high density of QDs nucleated at random positions. A large number of QDs with randomly distributed properties, e.g. size and strain, emits photons in a homogeneously broadened emission band of ≈ 50 nm with a center wavelength of 935 nm.

On samples with a low density of InAs islands only a small number of QDs are found per μm^2 which can be individually addressed. A QD is a two-level quantum system with ground state $|0\rangle$ and the excitonic state $|1\rangle$ storing quantum information. Moreover, the biexciton state enables two qubit operation as a controlled-NOT gate. Unless the control bit (first exciton) is set the target bit (second ex-

citon) cannot be rotated[50]. Building a network of electronically coupled QDs (quantum dot molecules) quantum information processing can be performed on a scalable architecture[51]. QDs have a much larger dipole moment in comparison to single atoms due to their lateral size. This ensures efficient coupling to flying qubits (photons). Moreover, the biexcitonic state can be used to generate entangled photon pairs[52]. Photons are ideal for the transmission of quantum information, e.g. for quantum communication, traveling at the highest possible velocity. Compared to solid state qubits, they interact weakly with their environment and are consequently ideal for storing quantum information. For two-qubit operations and quantum information processing on the other hand, good coupling strength of qubits is imperative. Combining both types of qubits, i.e. photons and quantum emitters, will be the topic of the following chapter on cavity quantum electrodynamics facilitating strong light-matter interaction in photonic crystals employing InAs QDs.

1.5 PCM nanocavities and cQED

The nanocavities used in the experiments presented in this work are defect type cavities inside two-dimensional photonic crystal membranes. Such defects are created by omitting one or more holes and thus breaking the periodicity of the photonic crystal membrane. Examples are the H1-cavity[53] (see Fig. 1.17), a single hole defect in a hexagonal lattice, and the L3-cavity which is formed by three missing holes (see Fig. 1.15). H1 and L3 are both defects in a hexagonal lattice. An optimized L3 cavity design is used in the experiments presented in this thesis. Displacement and/or reduction of the diameter of the holes on either end of the cavity enhances the confinement due to TIR of the electromagnetic mode by avoiding an abrupt change of the spatial mode profile[54].

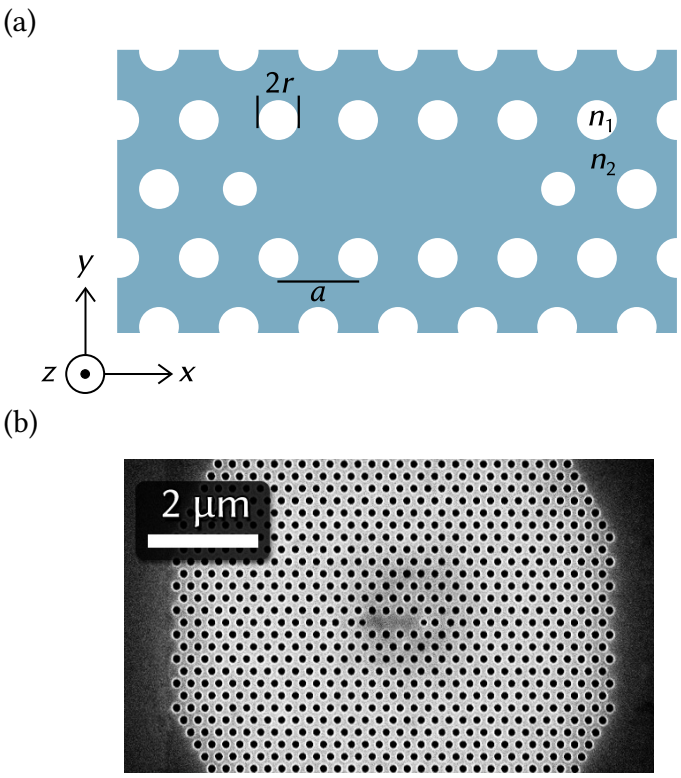

Figure 1.15 – (a) L3 nanocavity layout: The optical properties are set by the lattice constant a, air hole radius r, membrane thickness d (not shown), refractive index of the surrounding medium n_1 and the refractive index of the membrane n_2. (b) SEM picture of a L3 defect cavity used in the experiments.

To populate the cavity with photons, the photonic crystals were processed on GaAs wafer material with an embedded ensemble of InAs QDs. When optically excited by a laser, a broad spectrum is emitted due to the statistically distribution of the QD size. This photoluminescence (PL) background shown in Fig. 1.16 is decorated with the fundamental mode of the nanocavity if emitter position and wavelength coincide with the resonance wavelength of the cavity and an anti-node of the cavity mode profile.

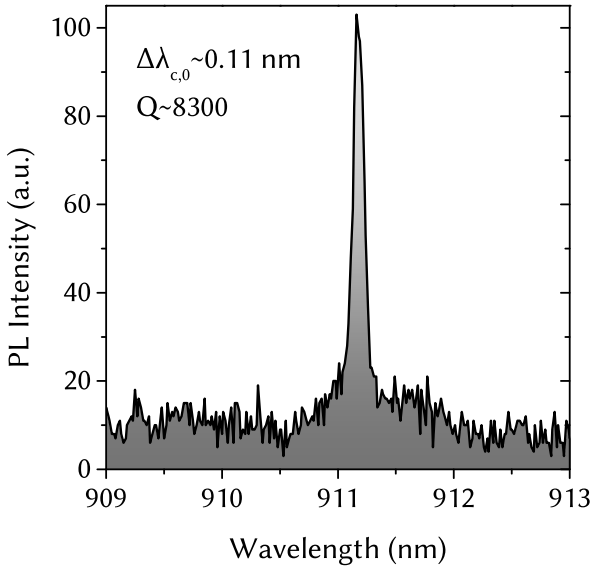

Figure 1.16 – Broad emission band of QDs and a L3 nanocavity resonance with a Q-factor of $Q \approx 8300$ at cryogenic temperatures $T = 7.5K$. Lattice constant $a = 260$ nm, hole radius $r = 80$ nm. The membrane thickness d is 134 nm with the refractive index of GaAs being $n_2 = n_{GaAs} \approx 3.4$. The surrounding medium is vacuum with $n_1 = 1$.

By choosing the lattice constant a and the hole radius r, i.e. the air-fill factor r/a, the mode resonance can be tuned to the desired wavelength as shown in Fig. 1.17 taken from [20].

In 2004, the vacuum Rabi splitting in a planar cavity-QD system was observed for the first time using a L3-defect nanocavity[34]. The observed splitting was $\Delta E_1 = 170\ \mu$eV. The energy was reversibly exchanged at a Rabi frequency $\Omega = \Delta E_1/2\hbar = 30$ GHz between the QD and the cavity with a Q-factor of 13300.

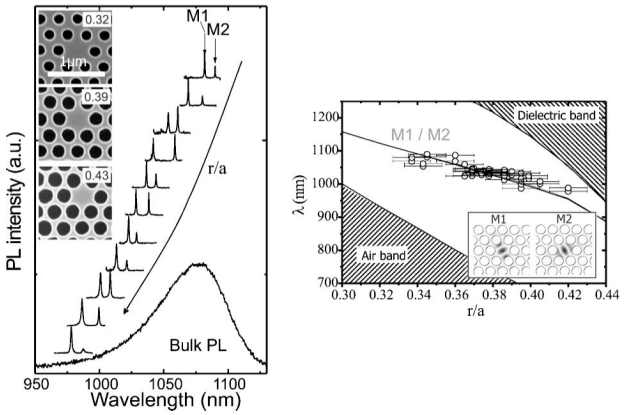

Figure 1.17 – Series of H1-cavities with different air-fill factors r/a shown in the SEM images in the inset (from [20]). The PL spectra recorded for the varying geometry show that the position of the two cavity modes can be tuned through QD emission band (Bulk PL). With the change of r/a the mode position within the photonic bandgap changes.

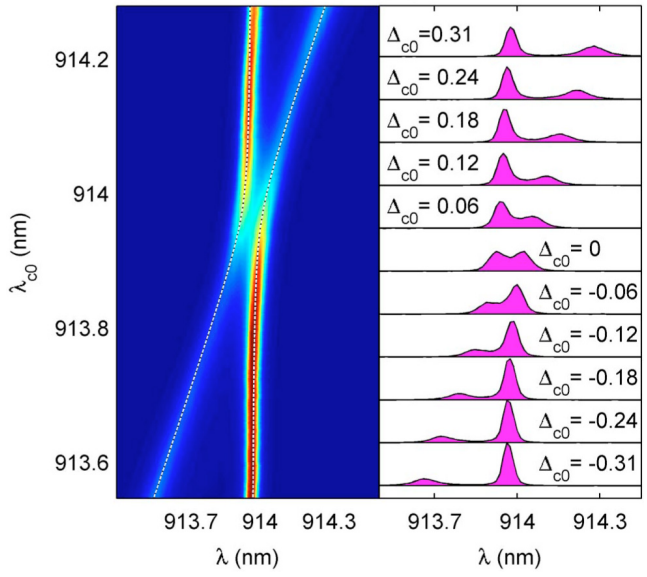

Figure 1.18 – Demonstration of the anti-crossing behavior of a single QD and the L3 cavity mode resonance taken from [55]. The mode resonance is spectrally shifted by adsorption of nitrogen to coincide with the QD emission. $\Delta\lambda_{c0}$ denotes the spectral shift in respect to the uncoupled mode wavelength in nm.

Fig. 1.18 shows a series of PL spectra of a single QD and a L3 cavity measured with a changing dielectric environment. By adsorption of nitrogen onto the cold membrane the refractive index of the photonic crystal changes. This causes the mode resonance to shift. This behavior is used to spectrally tune the mode into resonance with the QD emission. As this condition is fulfilled, the QD and the mode are strongly coupled. The spectral position of the empty cavity cannot be observed instead a clear anti-crossing of the QD and the mode is measured with a splitting of $\Delta E_1 = 132\ \mu$eV.

With a single photon in the cavity, the system is no longer transparent for another photon with $\hbar\omega_{photon} = E_1^{\pm}$ (Eq. 1.12). This 'photon blockade' behavior sensitive to single photons has been proposed to be used as a single-photon transistor [56]. Photons at the frequency of the bare cavity photons can tunnel through the cavity in a network of optical waveguides after the absorption of a 'gate' photon. This photon tunneling can be used for routing information in the form of photonic (flying) qubits for quantum information processing.

Furthermore, omission of a whole line of holes creates a waveguide allowing light inside the photonic bandgap to propagate along the line-defect. These have found applications in interconnecting defect cavities[14]. Strong confinement inside a line-defect within a 2D photonic crystal is achieved by locally changing its width (Fig. 1.19(a)). Here, the holes are shifted a few nanometers away from the waveguide center. A gap is introduced in the waveguide mode by this local width modulation efficiently confining light. Gaps in the modes of waveguides can also be introduced by locally changing the lattice constant and radius for a few columns of the photonic crystal (Fig. 1.19(b)), i.e. creating a double-heterostructure nanocavity[57]. Ultra-high-Q cavities with Q factors of more than $Q > 800000$ have been demonstrated in Si-photonic crystal waveguide cavities [58]. Vacuum Rabi splitting has been observed in photonic crystal waveguide cavities with $\Delta E_1 = 140\ \mu$eV[59].

The strong coupling regime requires a spectral and spatial overlap of the emitter and the mode wavelength as well as the position of the emitter at an anti-node of the mode profile. These conditions are in principle defined during the processing of the device. The passive nature of these optical devices has to be overcome

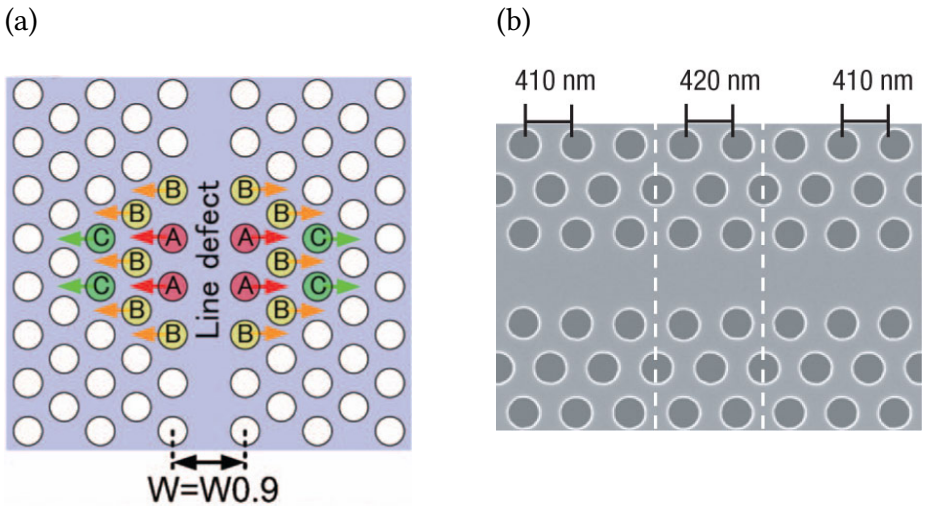

Figure 1.19 – (a) Line-defect with locally modulated width (from [58]) and (b) double-heterostructure (from [57]) effectively confine light ($Q > 5 \cdot 10^5$).

for fast and dynamic routing and filtering of photons and quantum information processing. Spectral manipulation is attained by changing the dielectric environment of the cavity. This is either done globally by changing the temperature, by adsorption of inert gases, or locally by means of irreversibly etching certain areas close to the cavity[60]. Another approach addresses the emitter. By incorporating the device into a lateral PIN-diode structure an electrical field can be applied. This field causes the emission wavelength of the QD to change due to the confined Stark effect. In recent experiments, a tuning rate of 150 MHz was thus achieved [19]. Compared to the spectral lifetime of the InAs QDs of less than 1 ns [20] when coupled to the continuum states of the vacuum most these techniques can be considered static. The surface acoustic waves enabling reversible tuning with GHz-rates are introduced in the next chapter.

1.6 Surface acoustic waves

The coupling of a quantum emitter to a photonic nanocavity is a promising building block for quantum gates in a scalable quantum information processing network. Multiplexing of streams of qubits requires a dynamic change or switching of the photonic building blocks of the network. The underlying time scale is determined by decay rates of the emitter and the rate of the cavity losses. Therefore, photonic crystal devices require a tuning mechanism with a high tuning rate and fine control of the coupling. This can be achieved with surface acoustic waves (SAW).

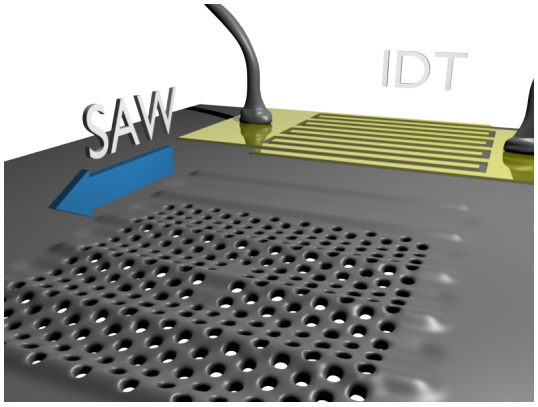

Figure 1.20 – Depiction of the SAW generated by an IDT deforming a photonic crystal membrane.

Surface acoustic waves are vibrational modes propagating over the surface of a solid. The mode used here is the Rayleigh surface acoustic wave. It is fairly popular for its application in cell- and smartphones as a bandpass filter for radio frequencies with wavelengths in the order of μm. It also causes destruction as seismic waves of an earthquake with wavelengths in the order of kilometers. These waves have been first mathematically described by Lord Rayleigh 1885[61]. Fig. 1.21 gives an overview which frequencies of surface acoustic waves overlap with the decay rates of InAs QDs inside a photonic crystal membrane nanocavity. Generation of SAW with frequency $f_{SAW} = 24$ GHz and more have been demonstrated [21]. These frequencies are sufficiently high to provide a tuning mechanism for manipulation of a strongly coupled cavity-QD system within its coherence time. The following chapter will present basic information on SAW. For more information on SAW and their application the reader is referred to [62],[63],[64] and [65].

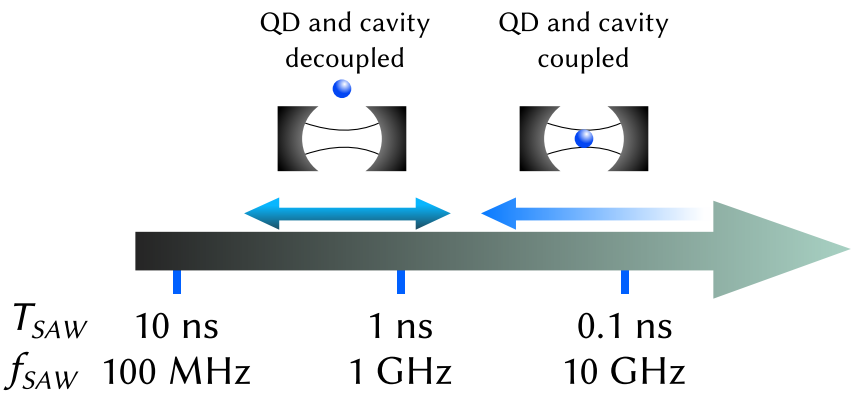

Figure 1.21 – Experimentally available SAW frequencies f_{SAW} and the respective SAW period T_{SAW} are compared to the coupling regime-dependent spectral lifetimes of an InAs QD.

1.6.1 Bulk elastic vibrations

In a homogeneous elastic medium the three elastic bulk eigenmodes (one longitudinal and two transverse) are described by the elastic wave equation with the stress tensor $\hat{T}$ and the displacement field $\mathbf{u}(\mathbf{r})$:

$$\nabla \cdot \hat{T} = \rho \frac{\partial^2 \mathbf{u}(\mathbf{r})}{\partial t^2} \tag{1.22}$$

The diagonal elements of $\hat{T}$ are non-zero for normal stress, i.e. tension or compression, whereas the off-diagonal elements describe shear stress. ρ is the density of the material. The wave equation is solved for a piezoelectric material like GaAs using the *constitutive relations*:

$$\begin{aligned} \hat{T} &= \hat{c}\hat{S} - \hat{p}\mathbf{E} \\ \mathbf{D} &= \hat{\epsilon}\mathbf{E} + \hat{p}\hat{S} \end{aligned} \tag{1.23}$$

The first equations is Hooke's law linking the stress tensor $\hat{T}$ to the strain tensor $\hat{S}$ via the 4th order elastic tensor $\hat{c}$. For a piezoelectric material Hooke's law is modified. $\hat{p}$ is denoting the piezoelectric tensor and $\mathbf{E}(\mathbf{r}) = -\nabla\Phi$ the resulting electric field. In a strained solid the atoms in the crystal and their dipole moments are displaced. Due to the asymmetry in a piezoelectric crystal this will cause a net polarization, i.e. an electric field. Likewise, exposed to an electric field the piezoelectric material will be polarized and generate strain. The displacement is linearly proportional to the electric field. The second constitutive relation describes the

electric displacement field $\mathbf{D}(\mathbf{r})$ due to the electric field and the deformation of the material with $\widehat{\epsilon}$ denoting the dielectric tensor. Compared to the speed of light the propagation velocities of acoustic phonons are much lower by a factor of 10^5. This justifies the use of quasi-electrostatic equations. Given a displacement field periodic in time, i.e. $\mathbf{u}(t) = \mathbf{u}_0\, e^{-i\omega t}$, and no free charges present ($\nabla \cdot \mathbf{D} = 0$) the following equations describe the wave propagation:

$$\begin{aligned} \rho\omega^2 u_i + c_{ijkl}\frac{\partial u_k}{\partial x_j \partial x_l} + p_{ijm}\frac{\partial \Phi}{\partial x_j \partial x_m} &= 0 \\ p_{jml}\frac{\partial u_m}{\partial x_j \partial x_l} - \epsilon_{jm}\frac{\partial \Phi}{\partial x_j \partial x_m} &= 0 \end{aligned} \tag{1.24}$$

Compared to bulk vibrations in non-piezoelectric materials the wave phase velocity v is increased by a small factor. This increase is also referred to as *piezoelectric stiffening*. For a longitudinal bulk wave the increase is given by:

$$\begin{aligned} v + \Delta v &= \sqrt{\frac{c(1+K^2)}{\rho}} \\ K^2 &= \frac{p^2}{c\epsilon} \end{aligned} \tag{1.25}$$

K is the electromechanical coupling constant. In general, $\widehat{K}$ is a 4th order tensor. It is depended on the components of the elastic, piezoelectric and dielectric constants in the direction of the wave propagation.

1.6.2 The Rayleigh surface mode

At the surface of a crystal ($z_{surface} = 0$) the components of the stress tensor $T_{xz} = T_{yz} = T_{zz}$ vanish. There is no stress at the surface in the $\mathbf{z}$ direction which is perpendicular to the surface plane spanned by $\mathbf{x}$ and $\mathbf{y}$. Another boundary condition imposed is the continuity of the z-component of the displacement field at the surface:

$$\begin{aligned} T_{xz} = T_{yz} = T_{zz} &= 0 \,|\, z = 0 \\ D_z(z = dz) &= D_z(z = -dz) \end{aligned} \tag{1.26}$$

If an elastic wave propagates along the surface the displaced volume of material is less strained since the halfspace with $z > z_{surface}$ is comprised of vacuum. Consequently the phase velocity is lower. This difference in velocity compared to the

bulk confines the SAW to the surface. The surface acoustic wave decays exponentially into the bulk. This is analogous to the index guiding of light in optical fibers. The solution of the wave equation using the boundary condition imposed by the surface yields different surface acoustic wave modes. In the following, only the Rayleigh mode which is a superposition of a longitudinal and a transverse displacement normal to the surface are of importance and referred to as SAW. Hence, a point of mass is moving on an elliptical path in the plane defined by the direction of SAW propagation and perpendicular to the surface of the solid (Sagittal plane). Fig. 1.22 depicts the mechanical displacement and the electric potential for a SAW

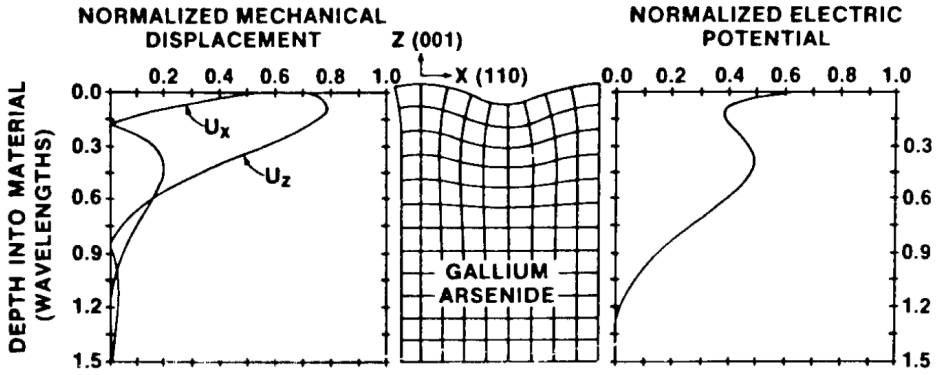

Figure 1.22 – Normalized potential and displacement in the direction of propagation u_x and normal to the surface u_z. The distance from the surface is given in multiple wavelengths (taken from [66]).

on (001) GaAs propagating in the piezoelectric $[110]$ direction. The amplitude of the mechanical displacement normal to the surface can be up to a few nanometers. The cross section in Fig. 1.22 is not to scale since the actual vertical displacement is much smaller than the SAW wavelength. For non-piezoelectric materials the displacement components derived from the wave equation (Eq. 1.22) at the surface using the boundary conditions for stress and displacement field are [67]:

$$\begin{aligned} u_x &= C\left(e^{-\Omega kz - i\phi} + c.c.\right) e^{i(kx-\omega t)} \\ iu_z &= C\left(\gamma e^{-\Omega kz - i\phi} + c.c.\right) e^{i(kx-\omega t)} \end{aligned} \tag{1.27}$$

Ω, γ and ϕ are explicit functions of the materials properties, i.e. elastic properties and phase velocity with complex values. C is the amplitude which has the dimension of length. k is the wavevector which is parallel to $\mathbf{x}$. A simplified real form of

the propagating wave is given by [62]:

$$u_x = A_x sin(kx - v_{SAW}t)$$
$$u_z = A_z cos(kx - v_{SAW}t) \tag{1.28}$$

A_x and A_z denote the amplitudes of u_x and u_z of the displacement as plotted in Fig. 1.22. The phase velocity v_{SAW} in a crystal with cubic symmetry like GaAs is determined by the elastic properties, i.e. the independent components of the elastic tensor c_{11}, c_{12} and c_{12}. For an isotropic material v_{SAW} is given by the lowest velocity given as solution of the following cubic equation in $X = \rho {v_{SAW}}^2 / c_{11}$ [67]:

$$\left(1 - \frac{c_{11}}{c_{44}} X\right) \left(\frac{c_{11}{c_{11}}' - {c_{12}}^2}{{c_{11}}^2} - X\right)^2 = X^2 \left(\frac{{c_{11}}'}{c_{11}} - X\right) \tag{1.29}$$

with ${c_{11}}' = \frac{1}{2}(c_{11} + c_{12} + 2c_{44})$. On the (001) surface of GaAs in the $[110]$ direction the SAW velocity is $v_{SAW} = 2864$ m/s [68] at room temperature. At cryogenic temperatures the velocity increases slightly to $v_{SAW} = 2960$ m/s. The phase velocity is frequency independent with a linear dispersion relation:

$$v_{SAW} = \lambda_{SAW} \cdot f_{SAW} \tag{1.30}$$

In case of deviations from the $[110]$ direction, the phase velocity differs and the SAW can couple to bulk waves. Moreover, the propagation in the $[110]$ direction provides the strongest piezoelectric coupling for GaAs. This direction is important for the efficient electric generation of the SAW.

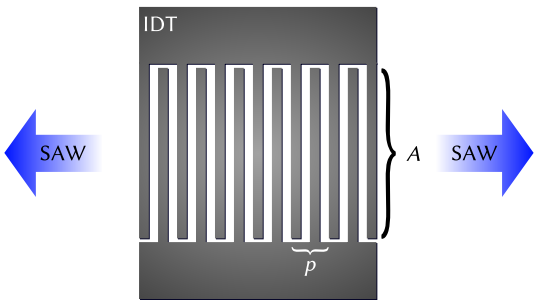

Figure 1.23 – Interdigital transducer (IDT) with finger period p and aperture A. The IDT generates SAW propagating perpendicular to its long finger axis.

This is achieved by applying an alternating voltage with frequency f to a pair of comb-shaped electrodes with intersecting fingers at spatial period $p = v_{SAW}/f$

shown in Fig. 1.23. These interdigital transducer (IDT) have been proposed by White and Voltmer 1965 [69]. The inverse piezoelectric effect causes the material beneath each finger pair to be either compressed or stretched depending on the sign of the voltage. Initially the displacement is a superposition of surface acoustic waves with many different wavevectors, i.e. a surface acoustic white noise. After the time f^{-1} the displacement with wavelength $\lambda_{SAW} = v_{SAW}/f = p$ is in phase with the surface acoustic wave generated at the next finger pair and amplified. Acoustic waves with wavelengths deviating from the finger period will interfere destructively. The frequency spectrum of the generated vibrations is determined by the finger shape, i.e. the Fourier transform of a rectangular function in the spatial domain with period p - the *sinc* function. Moreover, the finite size of the IDT has to be taken into account, i.e. the total number of finger pairs is convoluted with finger period p. Consequently, the number of fingers affects the width of the resonance.

Higher harmonics of the fundamental resonance will also interfere constructively. All other contributions to the initial wave packet will cancel out. A coherent beam of acoustic phonons is excited and emitted on either side of the IDT. The aperture

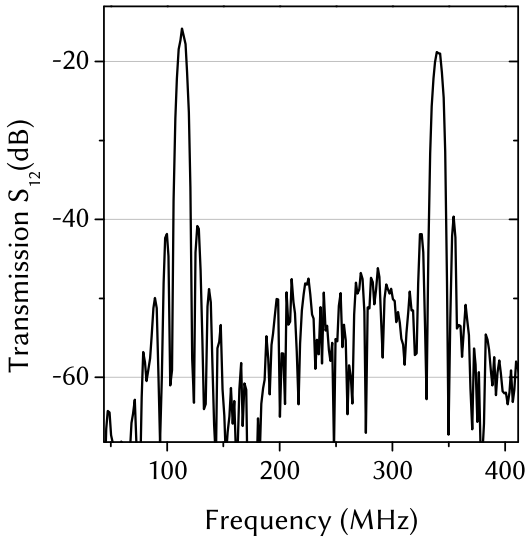

Figure 1.24 – SAW transmission of a split4-IDT delayline on $LiNbO_3$ measured with a network analyzer. The measurement shows the fundamental and third harmonic at $f_{SAW} = 115$ MHz and $f_{SAW} = 345$ MHz.

A of the IDT determines over which area the applied RF-power is distributed and

affects the impedance of the device. The IDTs used in the experiments presented here are single finger IDTs with an aperture $A = 200$ μm and 80 pairs of fingers. For a single finger IDT, successive fingers are on a different potential. This is the simplest type of IDT. For split-IDTs every finger is split into two. This second-order grating is advantageous for the generation of higher harmonics. Other IDT designs include tapered IDTs with a gradually changing finger period and focusing IDTs. A transmission measurement between two opposing split4-IDTs in Fig. 1.24 shows the resonance at the frequency of the surface acoustic wave f_{SAW} and $3f_{SAW}$. IDTs are commercially available in devices for filtering radio-frequencies, delaying signals, resonators and sensors. The SAW transmission on a delayline is very sensitive to any change of the elastic properties at the surface, e.g. the density. SAW devices with activated surfaces are employed to selectively sense the adsorption of gases. Lab-on-a-chip applications employ SAW devices for driving droplets and mixing small volumes of fluids.

SAW have proven relevance in fundamental research, e.g. the quantum Hall effect[70] or spin transport[71]. Two aspects of the SAW affect the electric properties of a QD, i.e. the strain field and electric field. The effects are referred to as deformation potential coupling and acousto-electric coupling. Both are modulated with the SAW period but exhibit a relative phase shift of π. At low power, SAW transmission is a sensitive probe of the sheet conductivity due to the latter effect ([72],[73]). Moreover, at high power the SAW can transport charge carriers by modulating the conduction and valence band of semiconductors. Electrons and holes are separated by $\lambda_{SAW}/2$ due to the electric field wave which accompanies the SAW ([74],[75]). This can be used to sequentially inject charge carriers into QD thereby creating a clocked single photon source [76]. The deformation potential coupling affects the wavefunctions and eigenstates of the charge carriers confined in the QD. This results in a spectral shift of the emission energy depending on the size and the composition of the InGaAs-QDs. Reportedly, under uniaxial stress the energy is assumed to shift to higher or lower energies depending on the Ga content. Measurements on adjacent QDs in the sample revealed different signs of the tuning slope[77]. Due to its arbitrary nature this shift is neglected in the following.

1.6.3 Photonic modulation with SAW

Materials exhibiting a strong variation of their refractive index due to strain are favorable for acousto-optical applications. A surface acoustic wave represents a propagating diffraction grating which will diffract light depending on the SAW wavelength, phase and amplitude. Light with wave vector $\mathbf{k}_0$ and angular frequency ω_0 will couple to the coherent acoustic phonons of the SAW in Stokes ($-$) and anti-Stokes ($+$) processes:

$$\begin{aligned} \mathbf{k}_{\pm 1} &= \mathbf{k}_0 \pm k_{SAW} \\ \omega_{\pm 1} &= \omega_0 \pm \omega_{SAW} \end{aligned} \tag{1.31}$$

The relative change of the refractive index is in the order of 10^{-4} [78] requiring a long interaction path of SAW and light. It has found applications in acousto-optical modulators or Bragg-cells facilitating indirect electrical control of the frequency and phase of the diffracted light using materials with a high piezoelectric coupling strength like $LiNbO_3$. If the SAW propagates over a one-dimensional lateral diffraction grating, umklapp scattering between the mini-Brillouin zones of the superlattice allows for more effective light diffraction[78]. This effect is further investigated for SAW propagating on vertically stacked layers, i.e. two Bragg reflectors creating a one dimensional photonic crystal nanocavity[80]. Here, the

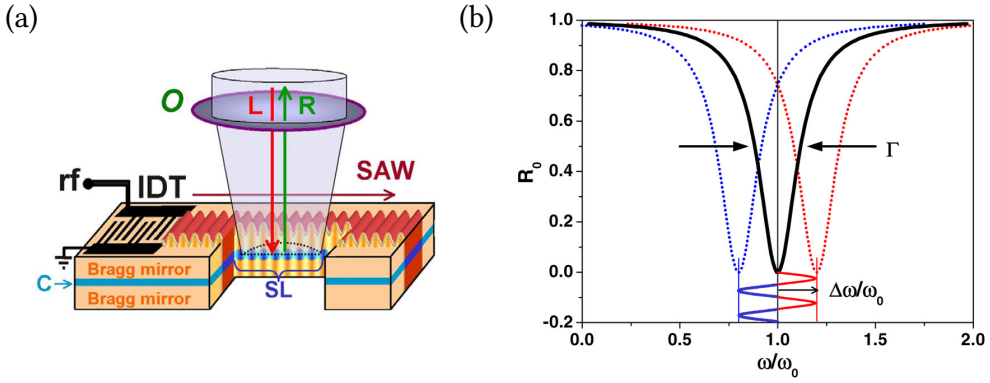

Figure 1.25 – (a) Schematic of a one dimensional photonic crystal cavity (C) created by two Bragg reflectors. Cavity length and refractive index are modulated by the SAW. (b) The cavity reflectivity R_0 is periodically shifted by $\Delta\omega$ by the SAW (from [79]).

modulation of the cavity resonance depends more on the variation of the vertical extent of the optical resonator than on the change of the refractive index. The dynamic superlattice (SL) created by the SAW folds the original photon dispersion. In Fig. 1.25 the optical resonance is shown to be shifted periodically by the SAW[79]. Since the acoustic amplitude decays exponentially within the order of λ_{SAW} from the surface this setup is not suited for high SAW frequencies, i.e. short wavelengths. This can be overcome by using bulk acoustic waves[81]. Here, a

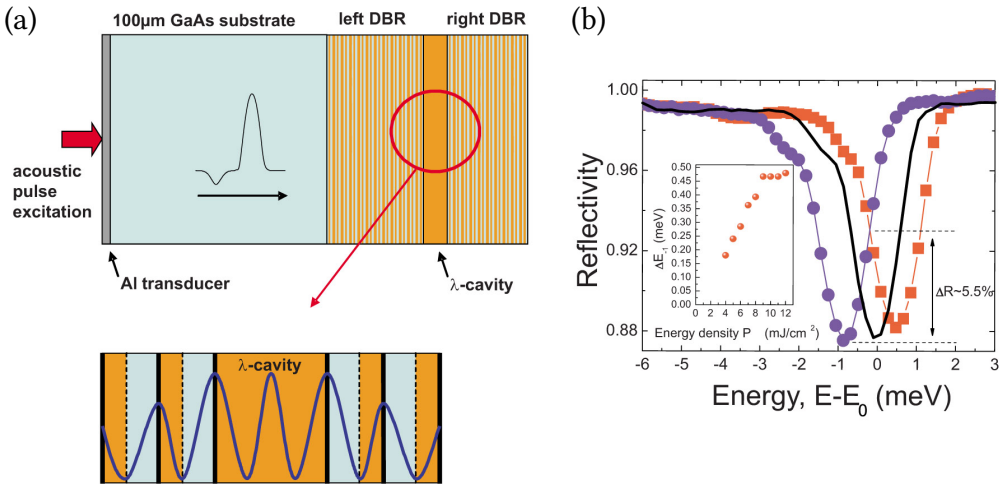

Figure 1.26 – (a) Schematic of the Fabry-Perot resonator deformed by a bulk acoustic wave generated by local heating with a laser pulse. (b) The deformation causes the cavity resonance and thus the reflectivity to be dynamically shifted (circles and squares) in respect to the undeformed cavity (solid line). The inset in (b) shows the dependence on the laser pulse power, i.e. the amplitude of the displacement (from [81]).

short pressure pulse propagates normal to the layers of a 1D photonic crystal cavity, i.e. a Fabry-Perot resonator shown in Fig. 1.26. The longitudinal component of the acoustic wave shifts the interfaces of the individual layers. The effect can be described by the simple model of a Fabry-Perot resonator with a dynamically changing length $L_{CAV}(t)$. It is discussed for photonic crystal membrane nanocavities in Chap. 3.2. Planar photonic crystal designs have proven to be successful in controlling spontaneous emission for laser applications with ultra-low threshold [33] which can be electrically driven[82]. Strongly coupled cavity-emitter systems and photonic crystal networks based on planar structures are widely regarded as

a promising approach for quantum information processing tasks ([83],[18]). For these planar photonic structures, we have demonstrated the feasibility of high-frequency tuning using surface acoustic waves.

In the experiments presented in the context of this thesis, the SAW is used to mechanically deform the photonic crystal membrane to tune the resonance of a nanocavity as illustrated in Fig. 1.20. In the following chapters experimental data and FDTD simulations will be presented.

2 Implementation and time-integrated experiments

The manipulation of the resonance condition of a photonic crystal membrane nanocavity at frequencies exceeding 1 GHz is demonstrated. In this chapter the general experimental implementation and the results of time-integrated experiments are described. These results motivate and instigate the need for stroboscopic and time-resolved experimental investigations as well as finite-difference time domain simulations presented in the chapters following hereafter.

2.1 Sample preparation and experimental setup

The targeted spectral tuning mechanism requires a sophisticated and elaborate sample production process. The functionality and performance hinges on the correct implementation, interaction and interoperability of the three building blocks by means of:

- MBE-growth of the heterostructure with embedded InAs QDs
- Photonic crystal membrane processing
- IDT processing

High quality optical properties of QDs and PCM nanocavity in respect to low non-radiative losses and good optical confinement in case of the latter are required. Moreover, interaction depends upon spectral overlap of the QD emission wavelength and the nanocavity resonance wavelength. Optical verification of the quality of this challenging manufacturing process is followed by IDT processing. Here,

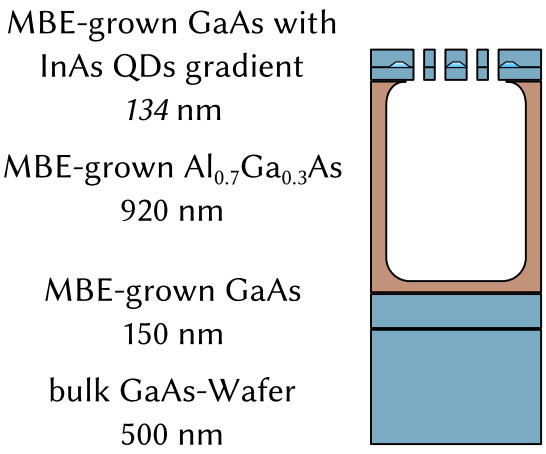

Figure 2.1 – Schematic cross-section of a PCM after electron beam lithography, reactive ion etching and hydrofluoric acid (HF) etching of the AlGaAs sacrificial layer.

particular attention has to be payed as not to degrade the optical quality of the PCM nanocavities. A more process parameter-specific and detailed documentation can be found in the Appendix. The following is intended to give a general overview of sample preparation and experimental implementation.

The semiconductor heterostructure shown in Fig. 2.1 includes the top-most GaAs layer with embedded InAs QDs grown on top a of $Al_{0.7}Ga_{0.3}As$ sacrificial layer. These layers are built upon a linking GaAs layer on a bulk GaAs wafer. The wafers used here were grown at the UCSB Materials Department MBE facilities of Pierre Petroff by either Hyochul Kim or Tuan Anh Truong. Following a verification of the QDs optical properties (emission wavelength and spontaneous emission rate), the PCMs were processed in three-step procedure. Using a Electron Beam Lithography System with an acceleration voltage of 100 kV the PCM air hole array is patterned into electron beam resist. The exposed resist is removed using the adequate developer. Subsequently, an inductively coupled plasma (ICP) reactive ion etch process transfers the hole array to the wafer. Care has to be taken that the top-most layer is etched through. The sacrificial layer needs to be etched to some extent. This is mandatory for the final production step in which the sacrificial layer is removed below the PCMs by hydrofluoric acid.

In the theoretical part of this thesis surface acoustic waves are described as deformations propagating on the surface of a solid. The time-scale of the investi-

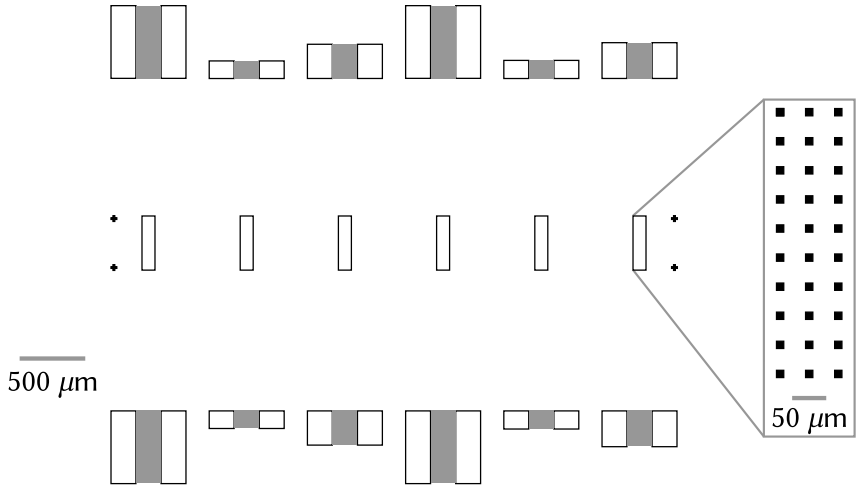

Figure 2.2 – Sample layout with six arrays of PCMs and pairs of single finger IDTs featuring different SAW wavelengths. Each PCM array comprises 30 PCMs.

gated SAW tuning mechanism is established by the SAW frequency f_{SAW}. The SAW wavelength λ_{SAW} and f_{SAW} are connected via the dispersion relation using speed of sound (see Eq. 1.30). Three different IDT geometries were processed and used in the experiments presented in this thesis: $\lambda_{SAW} = 7.28$ μm, 3.64 μm and 1.82 μm. These SAW wavelengths correspond to $28a$, $14a$ and $7a$ for a photonic crystal lattice constant of $a = 260$ nm. The sample layout featuring the PCM arrays enclosed by a pair of IDTs is shown in Fig. 6.4. The IDTs are processed using electron beam lithography and electron beam physical vapor deposition of 5 nm titanium and 50 nm aluminum. Measured at cryogenic temperatures, the IDT resonance frequencies f_{SAW} were found to be 414 MHz, 850 MHz, and 1703 MHz resulting in SAW periods of 2.4, 1.2, and 0.6 ns respectively. The experimental setup is presented in Fig. 2.3. The sample with PCMs and IDTs sits inside an evacuated continuous helium flow cooled cryostat. A RF signal generator is connected to the IDT providing the RF signal with the IDT resonance frequency f_{SAW} at RF power P_{RF}. The RF signal generator output is gated by a pulse generator signal. SAW-pulsing is needed to alleviate temperature tuning of the cavity resonance due thermal energy dissipation during SAW generation. The SAW pulse repetition rate has a typical value of $f_{Pulse} = 8$ kHz. The SAW duty cycle DC_{SAW} was chosen to be less than 1 %. The InAs QDs are excited by an IR laser emitting at $\lambda_{Laser} = 855$ nm. The QD photon emissions are dispersed by a spectrometer and either registered by a

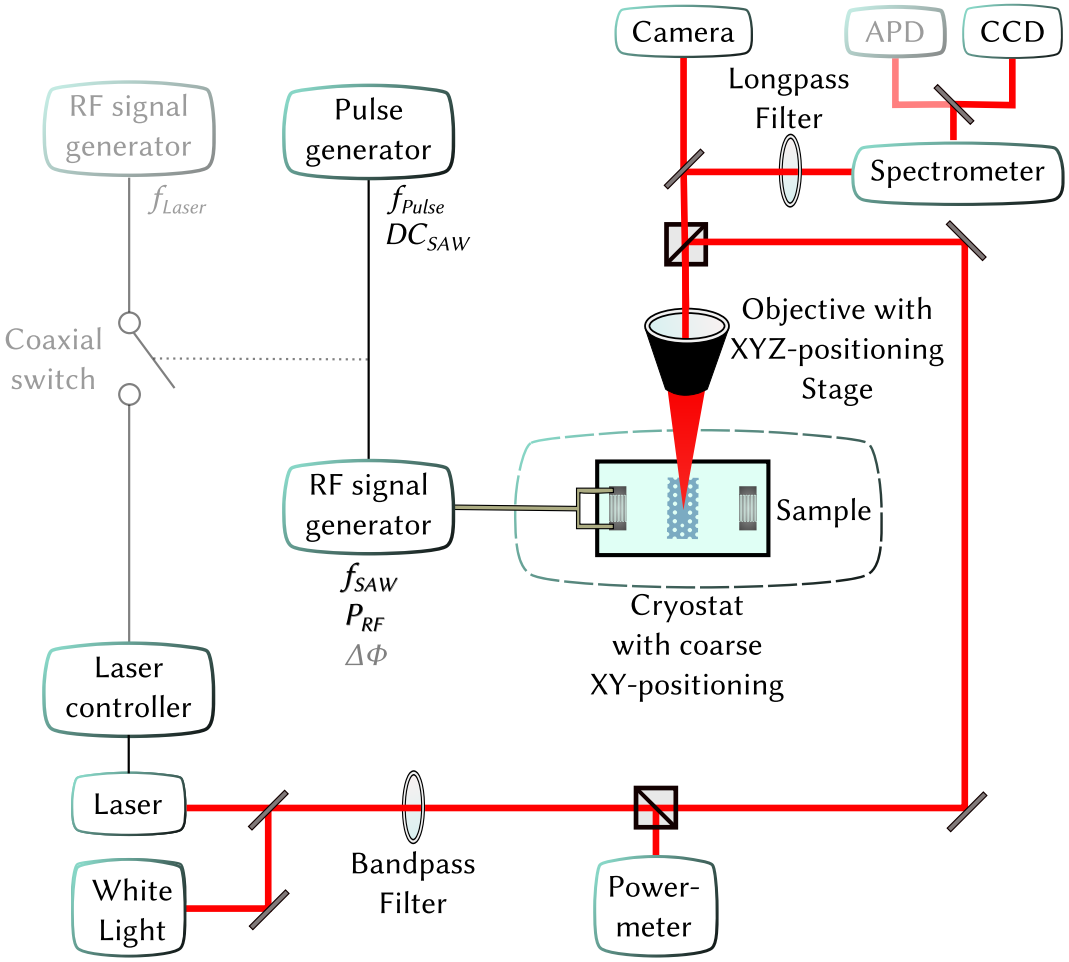

Figure 2.3 – Experimental setup used for μPL-experiments. The schematic features the cryostat, the exciting laser and the RF equipment for generation and timing of the SAW pulses. Equipment used for dispersion and detection of the collected photons emitted by the sample include a spectrometer, CCD and fast single photon detector. For differentiation, parts of the setup used for full time domain stroboscopic and time-resolved measurements are slightly greyed out.

CCD array detector or an avalanche photo diode (APD). Fig. 2.3 also includes the setup used for full time domain stroboscopic and time-resolved measurements described in Chap. 4.1 and 4.2. These measurements require a SAW phase-locking of the laser pulse to the SAW phase Φ_{SAW}. A detailed description of the experimental setup and methods is found in the Appendix.

2.2 Time-integrated experiments

The proposed tuning mechanism of the interaction between emitter and the cavity needs to proof its effectiveness. It should spectrally detune the cavity and the emitter by several linewidths of the cavity resonance. The spectral information in the measurements presented in this chapter is acquired using a monochromator and a CCD array detector. The acquisition over several seconds will average the spectral dynamics of the cavity mode actuated by the surface acoustic wave. The experiments discussed in this chapter are published in [84].

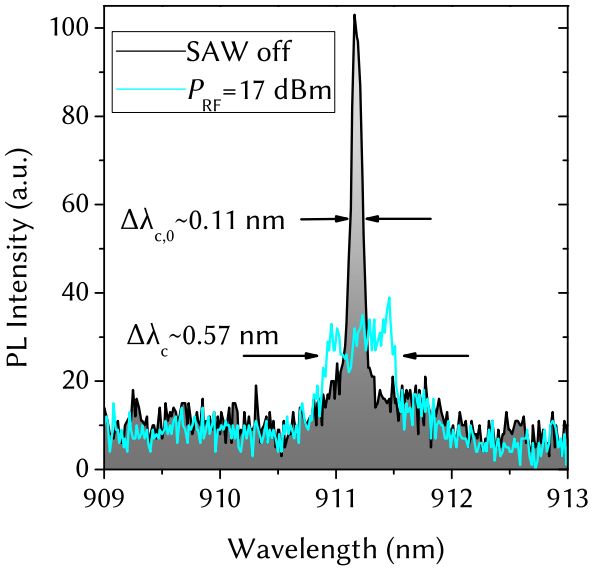

Figure 2.4 – Time-integrated measurement of the nanocavity mode with and without a surface acoustic wave. With moderate RF power the spectral feature exhibits a more than five-fold broadening. $P_{RF} = 17$ dBm, $f_{SAW} = 1703$ MHz.

The experimental data shown in Fig. 2.4 displays in black a PL spectrum with

the resonance of a L3 nanocavity fundamental mode at $\lambda_c = 911$ nm. The photonic crystal GaAs-membrane is populated by an ensemble of InAs QDs which are pumped by a diode laser via the wetting layer (see Chap. 1.4). The spectral width of the cavity mode $\Delta\lambda_{c,0} = 0.11$ nm corresponds to a quality factor of $Q = 8300$. This is regarded as a high value[26] for this cavity design and dielectric material. Due to absorption in the bulk material and the on the surface of GaAs Q-factors are limited to 10^4 [85]. The quality-factor depends on different fabrication aspects, e.g. side-wall roughness and circularity of the holes[86]. A seemingly pristine photonic crystal nanocavity when looked at in a scanning electron microscope (SEM) will exhibit a small Q-factor if light is Rayleigh-scatter on rough membrane-sidewalls. Upon applying the RF signal to the IDT at moderate power of $P_{RF} = 17$ dBm the surface acoustic wave is generated which deforms the photonic crystal membrane and the L3 cavity. As a consequence, the time-integrated spectrum of the mode changes as shown in Fig. 2.4. The observed spectral feature has a width of $\Delta\lambda_c = 0.57 \pm 0.1$ nm centered around the peak position of the undisturbed mode. During the acquisition time of the time-integrated measurement the PCM is deformed the SAW in a periodic manner. This causes the nanocavity resonance wavelength to be tuned over a certain spectral tuning range. As the time-integrated measurement does not provide the mode dynamics the spectral shift is obscured. Fig. 2.5 shows the normalized result of the numerical integration of a Lorentzian with oscillating mean $x_0(t) = A\,sin(\frac{2\pi}{T}t)$ for different amplitudes A (0 FWHM$\leq A \leq$ 10 FWHM of the Lorentzian).

$$F(x) = \int_0^{2\pi} d\Phi \frac{1}{\pi\left[\left(x - sin(\Phi)\right)^2 + 1\right]} \tag{2.1}$$

With increasing amplitude the spectral bandwidth which is covered by the integrated Lorentzians increases. In the time-integrated measurements presented here, the width of the spectral feature is a measure for the spectral tuning range dependent on the SAW amplitude. The spectral tuning range $\Delta\lambda_c$ extends from the furthest blue-shifted mode position to the red-shifted position when the cavity is largest as depicted in Fig. 2.6.

Hence, in Fig. 2.4 the SAW tuning facilitates a spectral tuning range of 5 times the full-width-half-maximum of the mode. For the resulting lineshape a fit using a

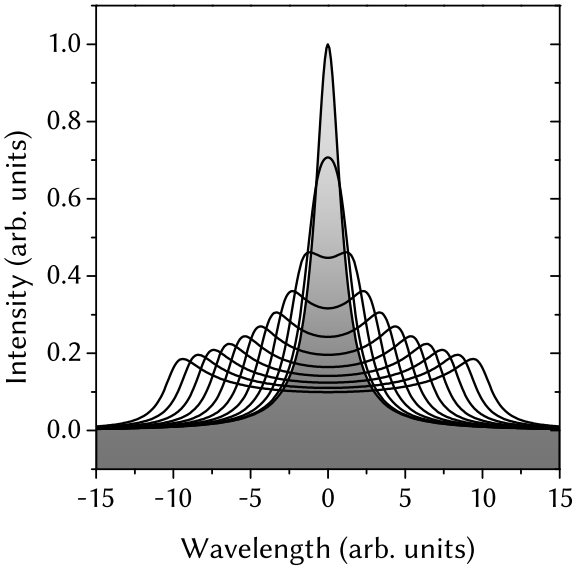

Figure 2.5 – Result of a numerical integration of a Lorentzian with oscillating mean x_0 with increasing amplitude up to 10 FWHM of the original function. In a time-integrated measurement the spectrum will be a superposition of all mode positions during the period T_{SAW}.

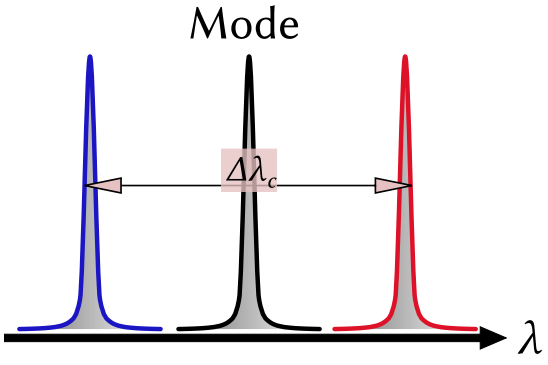

Figure 2.6 – The spectral tuning range $\Delta\lambda_c$ is established by the spectral shift of the mode wavelength during the SAW period T_{SAW}.

single Lorentzian is not possible. Consequently, for the uncertainty of the spectral tuning range value $\Delta\lambda_c$ the spectral linewidth of unperturbed cavity is used.

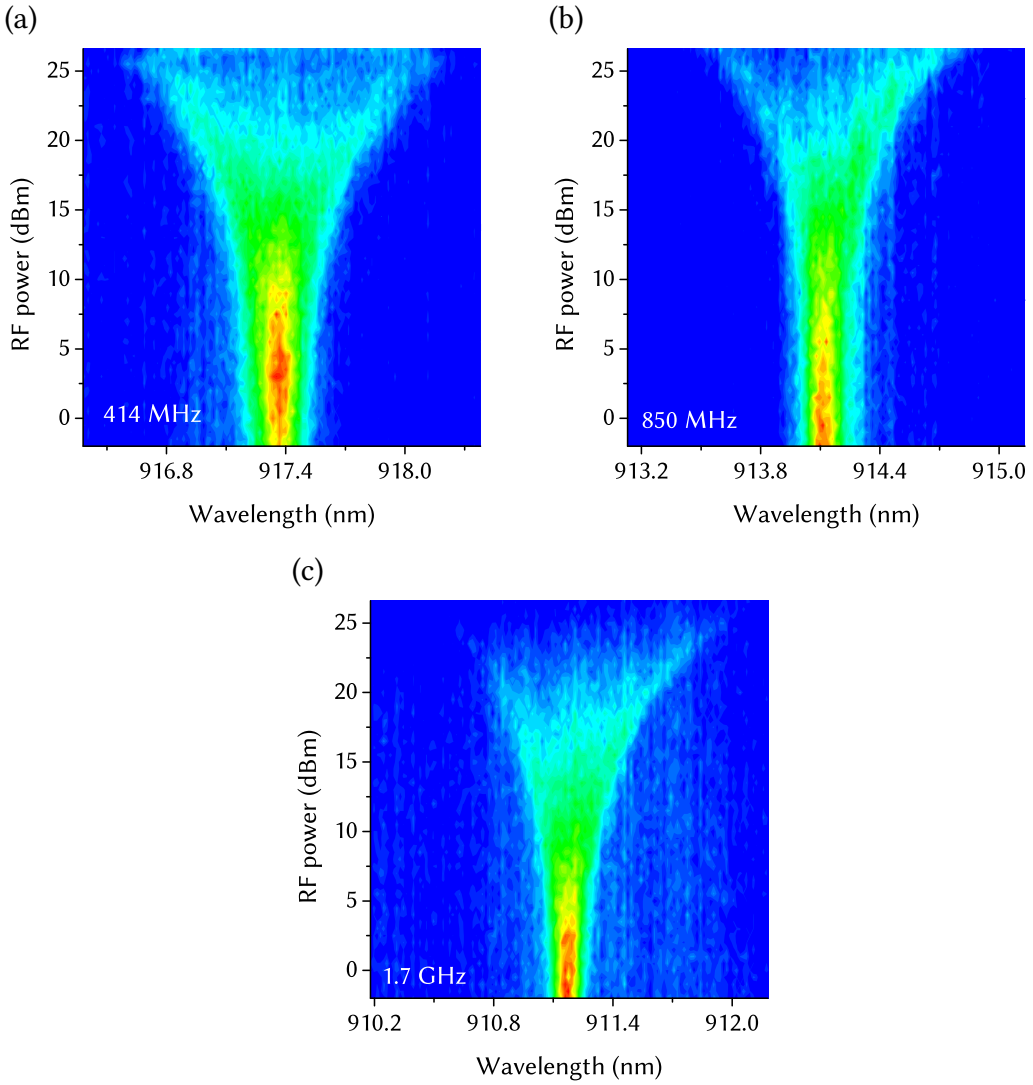

Figure 2.7 – Contour plots of RF power sweep measurements for SAW frequencies: (a) 414 MHz, (b) 850 MHz and (c) 1703 MHz.

For higher RF power, the spectral tuning range increases. As shown for the three investigated SAW frequencies in Fig. 2.7, the effect of the SAW is significant. For $f_{SAW} = 1703$ MHz, the mode traverses a spectral distance of $\Delta\lambda_c > 1.5 \pm 0.1$ nm. This spectral tuning range corresponds to more than 13.5 times the spectral linewidth of the unperturbed mode. The integrated spectrum of the oscillating Lorentzians in Fig. 2.5 exhibits a higher intensity at the maxima at $(\lambda_{c,0} \pm A)$ where the tuning rate $\frac{d\lambda_c(t)}{dt}$ is minimum. This intensity increase is also visible in the experimental data.

Considering a Fabry-Perot resonator with oscillating cavity length (see Chap. 1.2.2) the spectral shift of the nanocavity mode wavelength can be related to:

$$\lambda_{FP}(t) = \frac{2n}{m} L_{CAV}(t) \tag{2.2}$$

with m: mode index and n: effective refractive index of the membrane. Adopting this relationship allows for an estimation of the SAW amplitude via:

$$L_{CAV}(t) \propto A_{SAW} sin(\omega_{SAW} t) \tag{2.3}$$

with mode index $m = 5$ and $n = 2.75$ according to the L3 cavity design (described in the following chapter). This assumption infers that the cavity length is deformed proportional to the SAW amplitude. Accordingly, the spectral tuning range of $\Delta\lambda_c = 1.5$ nm from Fig. 2.7(c) results from a SAW amplitude of $A_{SAW} = \frac{m}{2n}\Delta\lambda_c = 1.4$ nm. This SAW amplitude is consistent with realistic values[79]. The achieved spectral tuning range is more than sufficient for cQED experiments with single QDs. Other methods used for this kind of experiments as for example gas adsorption[55] or heating[16] suffice to a spectral tuning range of < 1 nm.

Moreover, the Fabry-Perot resonator model implies a linear dependency of the spectral tuning range on the SAW amplitude. The spectral tuning range extracted from the measurements in Fig. 2.7 should therefore increase linearly with the amplitude of the surface acoustic wave A_{SAW}.

In Fig. 2.8 the spectral tuning range $\Delta\lambda_c$ is plotted against the square-root of the applied RF power P_{RF} which is proportional to A_{SAW}. The spectral tuning range is given in multiples of the undisturbed spectral width of the cavity mode $\Delta\lambda_{c,0}$. For all three SAW frequencies the experimental data shows a linear increase of the spectral tuning range proportional to A_{SAW}. Besides a confirmation of the linear increase of $\Delta\lambda_c$ as a function of the SAW amplitude the data also exhibits a difference regarding the magnitude of $\Delta\lambda_c$ in respect to the surface acoustic wave frequency f_{SAW}. The SAW tuning mechanism is most efficient for $f_{SAW} = 1703$ MHz achieving a $\Delta\lambda_c$ which is more than $8\times$ the spectral width of the undisturbed mode. At this frequency the SAW wavelength $\lambda_{SAW} = 7a$ is approximately twice the cavity length and therefore yielding the highest distortion of the L3-cavity. This is in accordance with FDTD simulation results presented in Chap. 3.2.

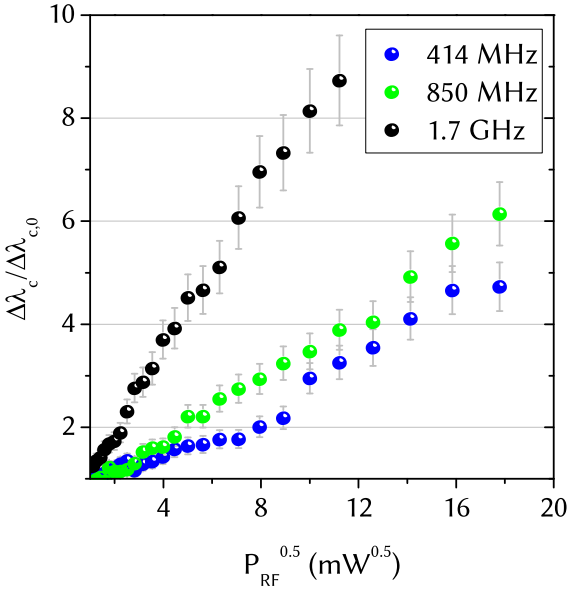

Figure 2.8 – Linear increase of the spectral tuning range with SAW amplitude as implied by the Fabry-Perot resonator model is confirmed. $\Delta\lambda_c$ is plotted against $\sqrt{P_{SAW}} \propto A_{SAW}$.

The differences in the spectral tuning range $\Delta\lambda_c$ for different SAW wavelengths indicates that the effect on the mode wavelength is caused by a mechanical deformation by the SAW. If the mode was broadened by a deformed or stressed membrane due to the heat generated by SAW transduction this would not be visible. Furthermore, $\Delta\lambda_c$ depends on the radio frequency applied to the IDT. As described in the theoretical section on interdigital transducers these devices exhibit a very narrow frequency response, i.e. a bandpass filter. Here, this frequency response is measured using a *Network Analyzer* by comparing the amount of power which is reflected at each RF frequency (red line in Fig. 2.9). By sweeping the IDT driving frequency over the center frequency of the IDT resonance the resulting SAW intensity is varied. Consequently, the spectral tuning range $\Delta\lambda_c$ reveals the same profile as the frequency response of the IDT measured with the *Network Analyzer*. Fig. 2.9 compares this measurement for the three investigated SAW frequencies. Indeed, the resonance wavelength of the nanocavity mode is altered only if a SAW is generated. This confirms that the mode wavelength is tuned by a mechanical deformation of the photonic crystal membrane due to SAW.

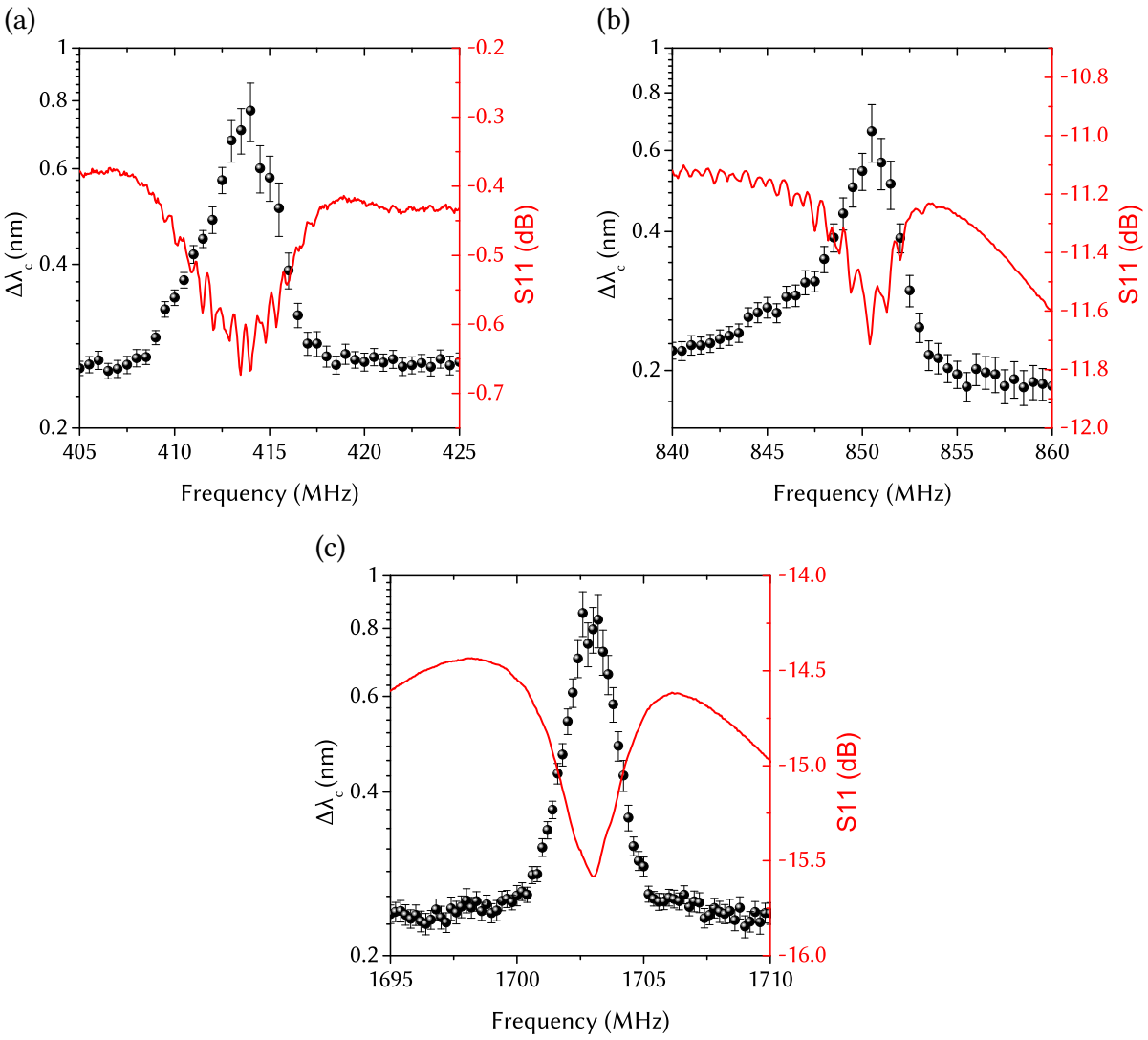

Figure 2.9 – Broadening of the nanocavity emission as a function of the applied RF frequency (symbols). The red line is the measurement of the power reflected by the IDT using a *Network Analyzer*: (a) 415 MHz, (b) 850 MHz and (c) 1703 MHz.

The presented time-integrated experiments demonstrate the effectiveness of the spectral tuning mechanism using SAW. The experimental results are related to a simple Fabry-Perot resonator model with variable cavity length. This comparison implies that for a higher SAW amplitude the mode resonance shift is increased due to an increased cavity size. Clearly, the spectral tuning range varies with the SAW wavelength used. To further investigate the ramifications a more elaborate modeling taking the geometry into account is required. To gather a deeper insight into the SAW tuning mechanism finite-difference time domain simulations are presented in the following chapter.

3 Simulating nanocavity modes manipulated by SAW using the Finite Difference Time Domain method

3.1 Introduction: FDTD simulation of PCM nanocavities

The aim of this thesis is to demonstrate the feasibility and effectiveness of high frequency tuning of a photonic crystal nanocavity with surface acoustic waves. The experiments are complemented by simulating the effect of the SAW. These simulations are not only intended to reproduce the experimental data, but also to provide new information which is not accessible in the experiments, e.g. the in-plane E-field distribution. This is also referred to as the spatial mode profile of the photonic mode. Moreover, since the electric generation of SAW requires a special IDT for each SAW wavelength (disregarding higher SAW harmonics and tapered IDTs) a SAW wavelength dependent characterization was done prior to the fabrication of samples.

Electromagnetic radiation is described by the well-known Maxwell equations (see Eq. 1.18 in Chap. 1.3). These equations describe the propagation and field intensities in time and space. In 1966, K. Yee published a paper demonstrating the numerical solution to a scattering problem of an electromagnetic pulse by a perfectly conducting cylinder[87]. The time-dependent partial differential Maxwell equa-

tions are solved numerically for discrete points in space and time by introducing a set of finite difference equations. Following Yee's publication, A. Taflove et al. published their work on the numerical stability of the method in 1975[88]. The name "finite-difference time domain" (FDTD) for this method was also coined by Taflove[89]. The former two publications are regarded as the seminal papers seeding widespread research and use of the finite-difference time domain method for computation of electromagnetic problems. A multitude of commercial and open-source applications are available today. Using the finite-difference time domain method, the steady-state and transient solution of an electromagnetic problem is attained in a leap-frog manner, i.e. alternately for the electric and magnetic field components. The simulation volume containing the photonic crystal and electromagnetic fields is discretized in a mesh of small sub-volumes named Yee cells. In each discrete time step the finite-difference equations approximating Maxwell's equations are solved based on the solutions obtained in previous time step. The time step is defined by the mesh size and the speed of light. FDTD calculations, as opposed to pure frequency-domain calculations, provide information on time-dependent properties in particular the Q-factor. Consequently, FDTD simulations are the ideal tool for fast prototyping of photonic crystals and optimization by parametric search since sample processing is expensive and time consuming. This section describes the setup of a FDTD simulation of a photonic crystal membrane nanocavity and the results obtained for an unperturbed cavity. It is followed by the effects of a deformation by surface acoustic waves on the principal and higher order modes of the nanocavity. For more information on the FDTD method the reader is referred to [90].

The work flow of setting up a simulation is described for a L3 cavity design. For the simulations presented here a commercial software product (*Lumerical FDTD Solutions*) has been used[91]. It allows setting up the device geometry similar to the workflow of CAD software. The program supports the import of GDSII files used by electron beam lithography applications. The geometry of the L3 cavity is depicted in Fig. 3.1. The photonic crystal consists of a hexagonal air hole lattice with a lattice constant of $a = 260$ nm and radius $r = 80$ nm ($r/a \approx 0.31$).

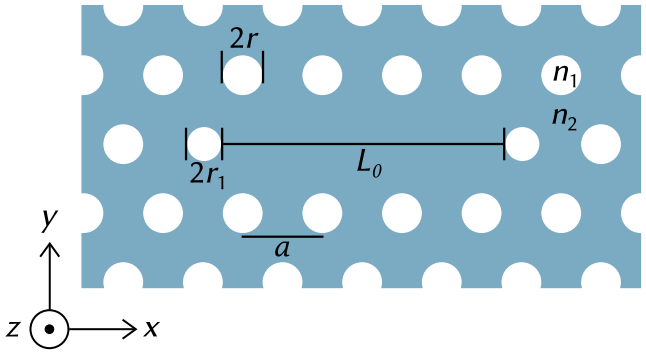

Figure 3.1 – Design parameters of the L3 cavity layout: Lattice constant $a = 260$ nm, air hole radius $r = 80$ nm, air hole radius at the cavity edges $r_1 = 0.85r$, membrane thickness $d = 130$ nm, refractive index of air $n_1 = 1.00$, refractive index of GaAs $n_2 = 3.54$. L_0 denotes the length of the cavity.

Light is confined in the z-direction by TIR in a membrane of thickness $d = 130$ nm. To improve this confinement, the air holes at the cavity edges have a smaller radius of $r_1 = 0.85r$ [54]. First, the modes which can be excited for this cavity design are determined. Dipole sources are placed in a random fashion regarding their polarization and lateral position within the cavity at the center of membrane at $z = 0$ nm. As described in Eq. 1.9, efficient excitation of the mode requires that the source is at the position of an antinode of the spatial electromagnetic field distribution. The source properties are set up in time-domain. The dipole source emits a pulse with a Gaussian envelope set to a center frequency of 330 THz and 6 ps pulse length resulting in a FWHM of 80 THz. This broadband pulse is necessary in order to excite any mode confine in the cavity. So called 'time monitors' record the electromagnetic field components in the time domain for the duration of the simulation at a user defined single point, plane or volume element. For the simulations presented here, the sampling rate is set to 3800 THz. The time monitors are set up to record after the source pulse. The total time of the simulation is 600 fs. A tradeoff between accuracy and computation time is necessary determining the size of the simulation mesh and the simulation volume, i.e. the size of the photonic crystal around the cavity. Here, the simulation volume spans over 15x15 rows/columns of holes to achieve good accuracy. The simulation mesh should be of small enough to accurately resolve the airholes but be as coarse as possible to

reduce the computation time. The relation between computation time and mesh step dx is $\propto (1/dt)^4$. Here, the minimum mesh step was set to 0.25 nm. Additionally, the software accounts variations occurring within a single Yee cell. The "Conformal Mesh Technology" of the software resolves subcell features by solving the integral Maxwell equations at the materials' interface. Light that is propagating out of the simulation volume is absorbed by so-called 'Perfectly Matched Layers' (PML). These PMLs are calculated to be impedance matched to the surrounding material avoiding reflections. The first run of the simulation provides the frequency spectrum of the excited cavity resonances by Fast Fourier transformation of the signal of the time monitor.

To identify the modes, the next simulation contains monitors which collect the spatial information of the light field at the resonance frequencies of the cavity identified in the previous step. The spatial mode profiles are shown in Fig. 3.2 and Fig. 3.3. The fundamental mode $M1$ of the L3 nanocavity has an antinode at the center of the cavity. This allows the emitter to be placed at good distance from GaAs surfaces avoiding non-radiative emission[92]. Clearly, this is a reason why the L3 cavity design is popular for cQED applications. The calculated mode

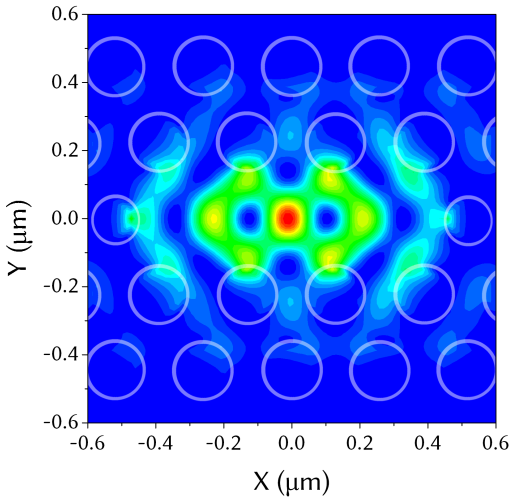

Figure 3.2 – Spatial profile $\mathbf{E}(\mathbf{r})^2$ at $z = 0$ nm of the fundamental L3 mode M1.

profiles and the resonance frequency of the fundamental mode $M1$ and higher order modes $M2$ and $M3$ are in good agreement with the literature [93].

From the spatial mode profiles resulting from this simulation the modes and their

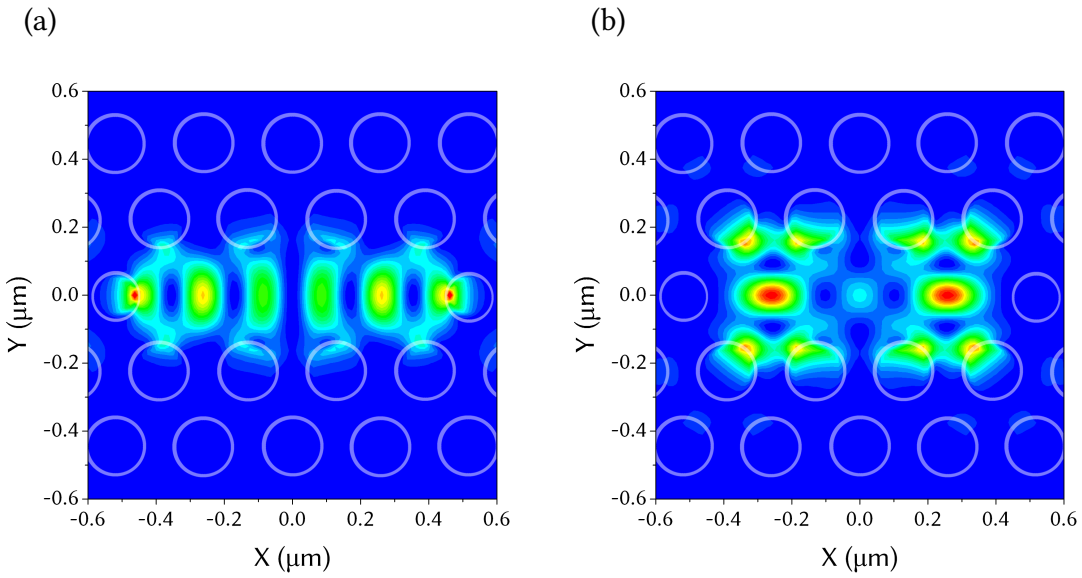

Figure 3.3 – Spatial mode profiles $\mathbf{E}(\mathbf{r})^2$ of higher order modes: (a) *M*2, and (b) *M*3

symmetries are identified. Any symmetry the desired modes exhibit can be used to reduce the computation time by introducing symmetry boundary conditions. A symmetry plane parallel to the membrane at $z = 0$ nm and another plane normal to the membrane along the x direction are used to reduce the computation time by a factor of 4. The mode profile itself allow for another symmetry plane parallel to the *y*-axis. However, this symmetry is broken by the SAW propagation along the *x* direction and therefore cannot be considered. The next task is to determine the *Q*-factor for a particular mode. Consequently, a single dipole source emitting at the mode's frequency with a narrow bandwidth (9 THz) is positioned at an antinode to excite the mode resonantly. The simulation time is increased to 1500 fs since a narrow band pulse has a longer duration (50 fs). Moreover, the simulation needs to be long enough to gather information on the cavity losses for *Q*-factor calculations. The simulation time should therefore be at least as long as half a cycle of the light field inside the cavity in addition to the emitter's pulse length.

There are different ways to determine the *Q*-factor. In order to establish *Q* from the mode's resonance linewidth the simulation time has to be as long as it takes for the field in the cavity to decay. This is impractical even for low-*Q* designs. Another way would be to monitor the energy loss from the cavity in the halfspace over the cavity as this defines *Q*-factor[94]. Here, the reduction of the field amplitude

measured at the resonant frequency of the mode f_{res} inside the cavity is calculated (ring-down simulation). The Q-factor is determined by the slope of the temporal decay of the electromagnetic field's envelope. The Q factor is calculated from the mean value of the slope calculated for each pair of data points of the envelope. The standard deviation determines the error of Q. The results obtained for $M1$, $M2$, and $M3$ are given in Table3.1.

Mode	λ_c	Q-factor Q_0	Polarization
$M1$	954.963 ± 0.005 nm	7958 ± 7	y
$M2$	899.539 ± 0.005 nm	713 ± 1	y
$M3$	880.977 ± 0.005 nm	488 ± 3	x

Table 3.1 – Calculated wavelength, Q-factor and polarization of the first three modes of the L3 cavity.

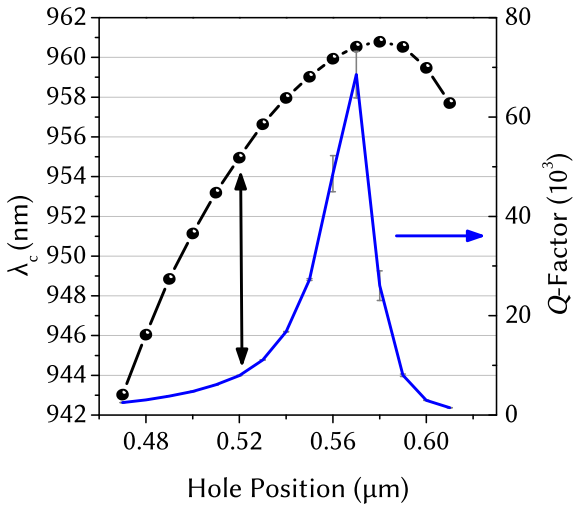

Figure 3.4 – Variation of the mode wavelength λ_c (circles) and Q-factor (line) with the position of the airholes at the cavity edges. The black double-arrow indicates the investigated design.

The Q-factor of the fundamental mode $M1$ can be optimized by changing the position of the airholes at the cavity edges. This locally changes the Bragg reflection condition which in turn confines the mode more gently and improves the confinement in the z-direction by TIR[54]. The FDTD simulations show that the Q-factor

increases up to $68 \cdot 10^3$ as shown in Fig. 3.4. The chosen cavity geometry for the simulations improves the confinement of higher order modes[93] is marked by a double-arrow. Moreover, it facilitates a clear analysis of the cavity distortion by the SAW since the cavity mode wavelength exhibits a linear dependency on the hole position change. Additionally, this geometry is less susceptible to fabrication imperfections in respect to the *Q*-factor.

The accuracy of the simulation results depends on the sampling rate of the monitors and the simulation time. Clearly, a simulation time long enough for the electromagnetic fields to decay improves the accuracy of the frequency domain information calculated by Fast Fourier transformation of the time domain signal. Other factors include the simulation volume, i.e. the size of the photonic crystal which is simulated, and the modeling of material's optical parameters. The focus of the following calculations is on relative changes of the resonance wavelength and the *Q*-factor. Accordingly, the accuracy of the absolute values is not crucial for the sake of argument. The minimum error for the simulated resonance wavelengths is given by the resolution of spectral data of 0.01 nm calculated by Fast Fourier transformation. This value is chosen as the uncertainty for the resonance wavelengths.

In the next chapter the influence on *M*1 for a photonic crystal membrane deformed by SAWs is discussed.

3.2 Tuning of the fundamental mode of a L3 nanocavity

The SAW mode consists of a longitudinal and a transversal component normal to the surface (see Chap. 1.6.2). Propagating on a photonic crystal membrane, the longitudinal component changes the periodicity of hexagonal air-hole lattice as well as the shape of the air-holes which become elliptical. This affects the Bragg condition for light propagating in the plane. The transversal displacement SAW component varies the TIR waveguiding properties of the membrane. This effect is neglected in the simulations since the effect on the waveguided mode is weak. Additionally, the variation of the refractive index of the GaAs due to strain is not considered since its relative change is in the order of 10^{-4}. This is a negligible variation compared to the index contrast of GaAs to air. A SAW propagates at the speed of sound of the solid which is 5 orders of magnitude lower than the speed of light. As described in the previous section, the simulation time sufficient to collect information on the dynamic properties of the cavity is half a cycle of the mode light field ($\approx$ 1500 fs). Thus, disregarding the propagation of the SAW during the simulation time, i.e. assuming a static deformation of the membrane, is a valid approximation. Consequently, the deformation of the photonic crystal membrane was superimposed prior to the FDTD simulation. The deformation of the membrane for SAW propagating in the x-direction is calculated using:

$$u_x(x,t) = A_{SAW}\, sin\left(2\pi\left(\frac{x}{\lambda_{SAW}} + \frac{t}{T_{SAW}}\right)\right) \tag{3.1}$$

Input parameters are the wavelength of the SAW λ_{SAW} and the SAW amplitude A_{SAW}. The period of the SAW $T_{SAW} = {f_{SAW}}^{-1}$ relates to the SAW wavelength via the dispersion relation using a phase velocity in GaAs of $v_{SAW} = 3100$ m/s. As a result, Eq. 3.1 describes the dynamic deformation of a nanocavity stretched at $t = 0.25\, T_{SAW}$ and compressed half a SAW period later. In the following, the effects of the deformation on the mode resonance wavelength and Q-factor are investigated for different SAW wavelengths propagating in the x- and y-direction (see schematic in Fig. 3.1). Fig. 3.5 shows the deformation of the cavity design introduced in Chap. 3.1 with $a = 260$ nm, $\lambda_{SAW} = 7a = 1.82$ μm with $\mathbf{k}_{SAW} \parallel$

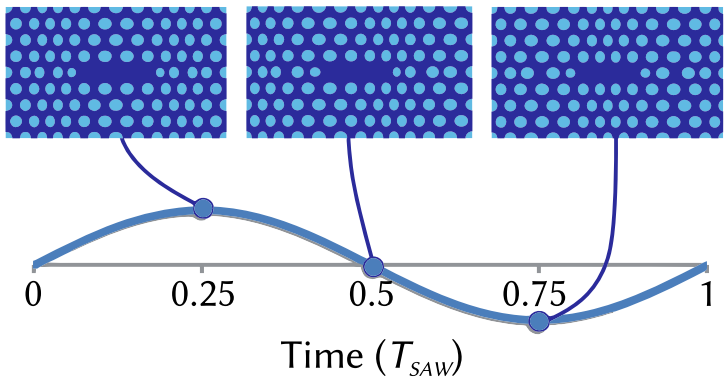

Figure 3.5 – Cavity deformation at different times t during the SAW period T_{SAW} for $\lambda_{SAW} = 7a$ and $A_{SAW} = 50$ nm.

x. For the deformation to be perceivable an unrealistically high SAW amplitude $A_{SAW} = 50$ nm is used.

The effects of a realistic amplitude of $A_{SAW} = 1$ nm on the mode wavelength and its Q-factor are presented in Fig. 3.6 and Fig. 3.7 for ($\mathbf{k}_{SAW} \parallel \mathbf{x}$) and ($\mathbf{k}_{SAW} \parallel \mathbf{y}$) respectively. The resulting change of the mode resonance is given relative to the value of the undeformed cavity $\lambda_{c,0}$. In Fig. 3.6 the SAW wavelengths investigated are $\lambda_{SAW} = 7a = 1.82$ μm, $\lambda_{SAW} = 14a = 3.64$ μm, and $\lambda_{SAW} = 28a = 7.28$ μm. The shortest of the above wavelengths causes the greatest shift of the resonance wavelength. In fact, $\lambda_{SAW} = 7a$ is distinguished due to the geometry of the L3 cavity, i.e. the length of the cavity, $L_0 \approx 3.5a$, in the x-direction (see Fig. 3.1). For this SAW wavelength the cavity is deformed to its fullest extent, since the SAW half-wavelength fits into the cavity. The other two SAW wavelengths are chosen for comparison. All three are used in the experiments discussed in the previous chapter and Chap. 4. Fig. 3.7 displays the results of these SAW wavelengths and additionally $\lambda_{SAW} = 3.2a = 832$ nm which is twice the cavity length in the y-direction assessed from the data shown in Fig. 3.10(b). Clearly, the modulation of the mode follows the sinusoidal deformation of the photonic crystal. This is a common feature found for all SAW wavelengths simulated. For the SAW wavelengths given in Fig. 3.6(a) and Fig. 3.7(a) the mode exhibits the maximum red-shift at time $t = 0.25T_{SAW}$ when the cavity is stretched to its highest extend. Half a SAW period later, at $t = 0.75T_{SAW}$ the mode is blue-shifted. A comparison

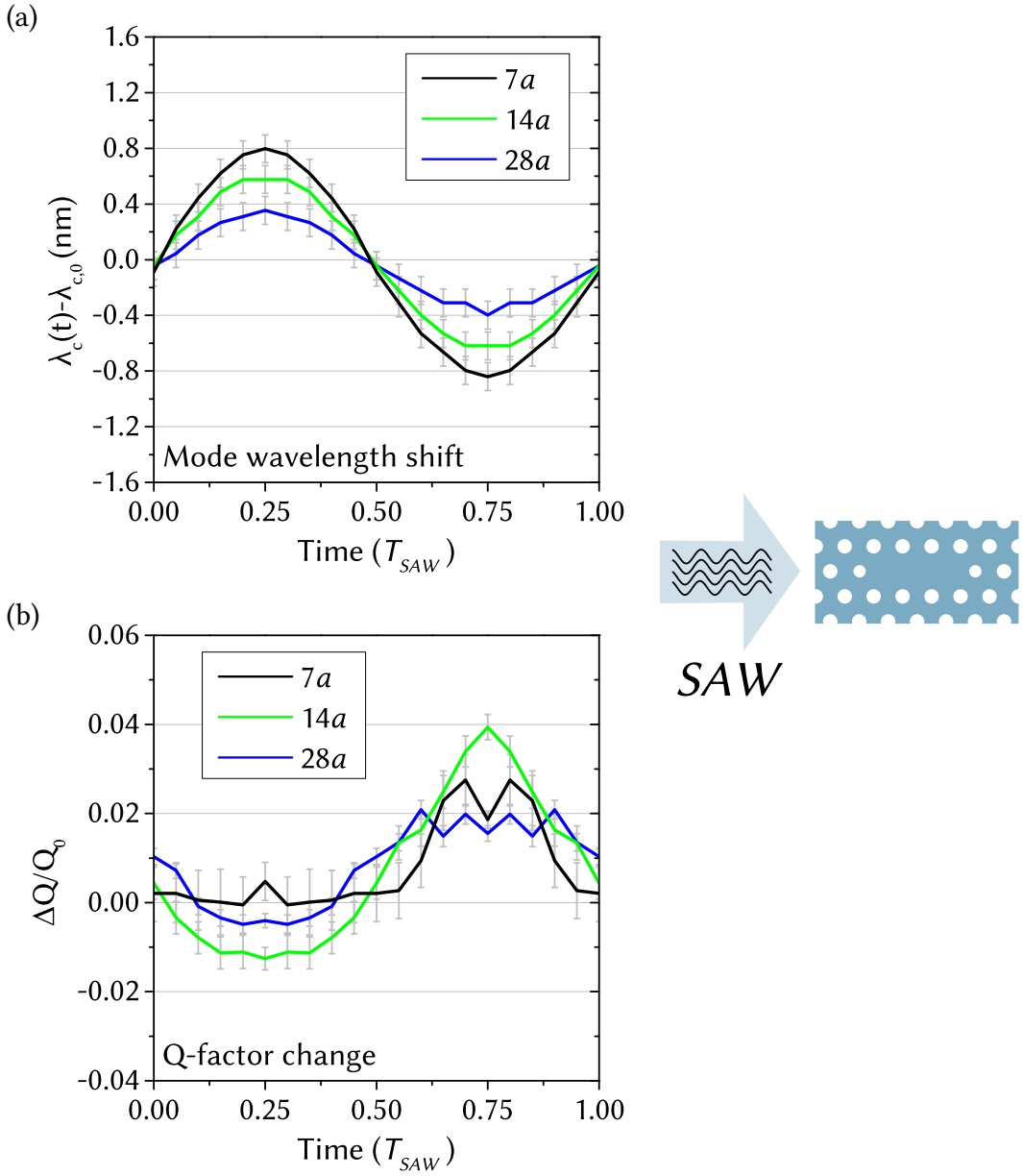

Figure 3.6 – FDTD simulation results for $\lambda_{SAW} = 7a$, $\lambda_{SAW} = 14a$ and $\lambda_{SAW} = 28a$ with $A_{SAW} = 1$ nm for SAW propagating in the x-direction: (a) Shift of the mode wavelength $\lambda_c(t) - \lambda_{c,0}$. (b) Relative Q-factor change $\Delta Q(t)/Q_0 = (Q(t) - Q_0)/Q_0$.

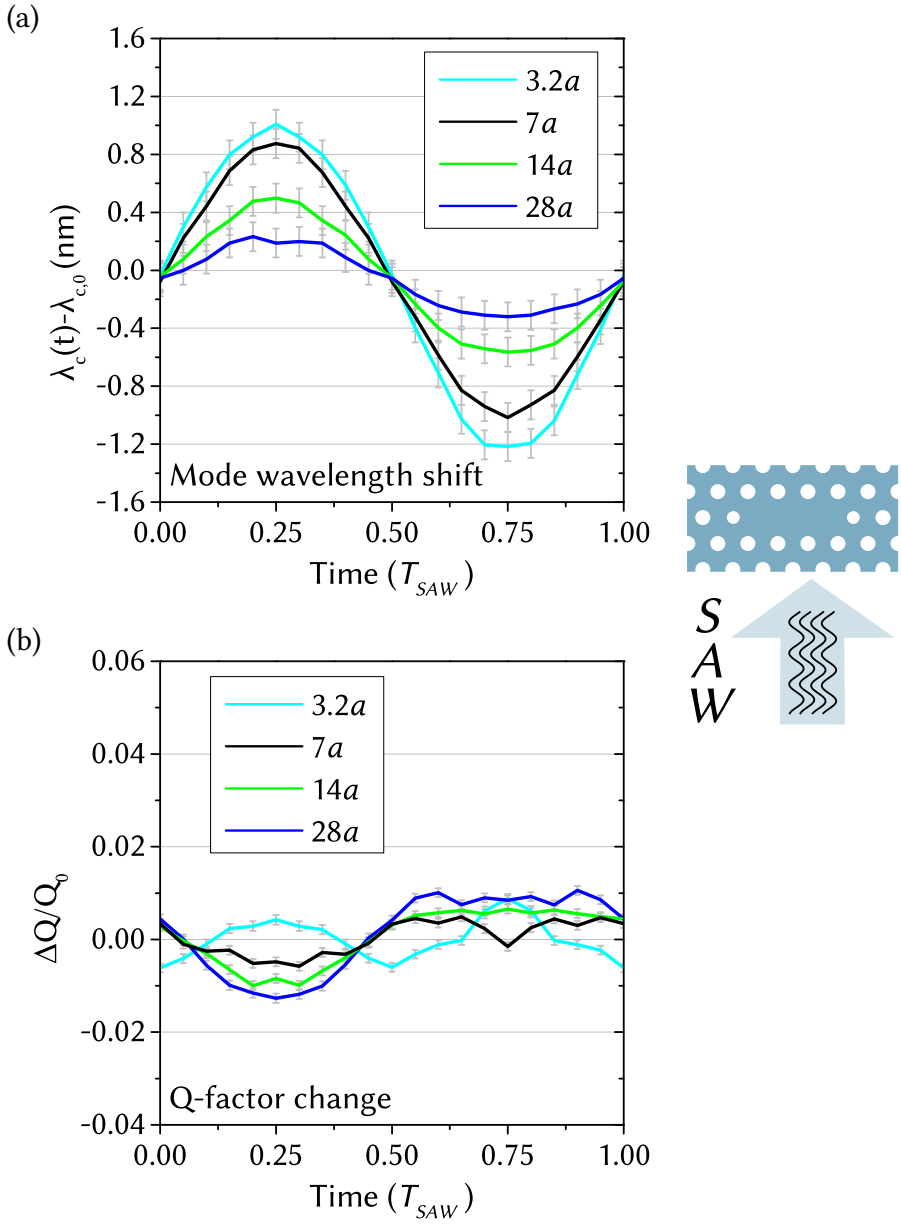

Figure 3.7 – FDTD simulation results for $\lambda_{SAW} = 3.2a$, $\lambda_{SAW} = 7a$, $\lambda_{SAW} = 14a$ and $\lambda_{SAW} = 28a$ with $A_{SAW} = 1$ nm for SAW propagating in the y-direction: (a) Shift of the mode wavelength $\lambda_c(t) - \lambda_{c,0}$. (b) Relative Q-factor change $\Delta Q(t)/Q_0 = (Q(t) - Q_0)/Q_0$.

to the Fabry-Perot (FP) resonator model (see Chap. 1.2.2) with variable resonator length $\Delta L_{CAV}(t) \propto u_x(x,t)$ is apparent and results in the same phase dependence of the mode wavelength change:

$$\lambda_{FP}(t) = \frac{2n}{m} L_{CAV}(t) \propto u_x(x,t) \propto sin\left(2\pi\left(\frac{x}{\lambda_{SAW}} + \frac{t}{T_{SAW}}\right)\right) \tag{3.2}$$

Here, n is the refractive index and m is the index of the resonant mode. For $\lambda_{SAW} = 7a$ in Fig. 3.6(a) the mode exhibits a spectral tuning range $\Delta\lambda_c > 1.6$ nm for a SAW amplitude of 1 nm. The spectral tuning range is a measure of the combine blue- and redshift of the mode calculated by:

$$\Delta\lambda_c = \lambda_c(t = 0.25\,T_{SAW}) - \lambda_c(t = 0.75\,T_{SAW}) \tag{3.3}$$

For $\lambda_{SAW} = 7a$ the spectral tuning range exceeds more than $13\times$ the calculated spectral width of the resonance. Accordingly, the simulation shows in accordance with the experimental results that the SAW-tuning mechanism is efficient and well suited for the manipulation of the cavity-QD coupling. For longer SAW wavelengths the cavity deformation is smaller resulting in a smaller spectral shift of the mode. For the cavity being deformed along its short side ($\mathbf{k}_{SAW} \parallel \mathbf{y}$) the spectral tuning range for $\lambda_{SAW} = 3.2a$ has a value of $\Delta\lambda_c > 2.2$ nm. Comparing the results of $\lambda_{SAW} = 7a$, $14a$ and $28a$ for both propagation directions, $\mathbf{k}_{SAW} \parallel \mathbf{y}$ yields a slightly pronounced shift for $7a$ and a slightly smaller effect for the longer two SAW wavelengths.

Fig. 3.6(b) and Fig. 3.7(b) show the change of the Q-factor $\Delta Q(t) = Q(t) - Q_0$ relative to the original Q-factor Q_0, i.e. $\Delta Q(t)\,/\,Q_0$. A high Q-factor is a prerequisite for attaining strong coupling conditions in cQED experiments. The FDTD simulations show that the deformation of the photonic crystal by SAW decreases the Q-factor by less than 4% for both directions of SAW propagation. Notably, the change of the Q-factor over the SAW period is not consistent for all SAW wavelengths. Additionally, the Q-factor change differs for different modes of the L3-cavity as will be presented for $M2$ and $M3$ in the next chapter. For $\lambda_{SAW} = 3.2a$ ($\mathbf{k}_{SAW} \parallel \mathbf{y}$) the Q-factor of $M1$ increases slightly at $t = 0.25\,T_{SAW}$ and $t = 0.75\,T_{SAW}$. Whereas for all other SAW wavelengths the compressed cavity has an increased Q while decreasing for cavity expansion.

This contrasts the calculation shown in Fig. 3.4 where the Q-factor increases when the cavity length is extended in the x-direction by shifting the position of the two outer air-holes. As the SAW not only changes the position of two air-holes the principle of locally changing the condition of Bragg reflection for improved confinement[54] does not apply here. A comparison with the Fabry Perot model is not useful here since for this model the Q-factor is independent of the cavity length but depends on the reflectivity of the mirrors, i.e. the finesse (see Eq. 1.14). For a photonic crystal membrane the lateral mode profile, the confinement and thus the Q-factor are strongly affected by the overlap of the mode profile with GaAs/air-interfaces. This has been used to improve the coupling to a single mode fiber (SMF) by changing the position of 18 holes and thereby matching the mode profile to that of the SMF[95]. Similarly, the SAW shifts the position of every hole which results in an improved confinement for a decreased cavity length at $t = 0.75\,T_{SAW}$. Moreover, the SAW not only changes the dimension of the L3 cavity but alters the hole shape and the lattice constant for the entire photonic crystal. The air-fill factor r/a effects the width of the photonic bandgap and the spectral distance of the mode to the photonic bandgap edges [41][20] (see Fig. 1.17). An oscillation of the air-fill factor as a function of time and space could thus improve the confinement for a smaller cavity.

The spatial mode profile of the deformed cavity is shown in Fig. 3.8. For both SAW propagation directions the lateral distribution of the electric field for the stretched (left/lower half of the plot) and the compressed cavity (right/upper half of the plot) are compared for $\lambda_{SAW} = 7a\,(\mathbf{k}_{SAW} \parallel \mathbf{x})$ and $\lambda_{SAW} = 3.2a\,(\mathbf{k}_{SAW} \parallel \mathbf{y})$ at $A_{SAW} = 1$ nm. Apparently, the change of the cavity geometry changes the spatial mode profile just slightly. Moreover, the positions of the anti-nodes of the mode profile do not shift. Since, the coupling of emitter and cavity relies on good spatial alignment of emitter and anti-node of the field this is an important property of the SAW tuning mechanism.

With increasing SAW amplitude A_{SAW}, the deformation of the photonic crystal and consequently the spectral tuning range increase. The simulation results shown in Fig. 3.9 confirm a linear increase for all investigated SAW wavelengths and both

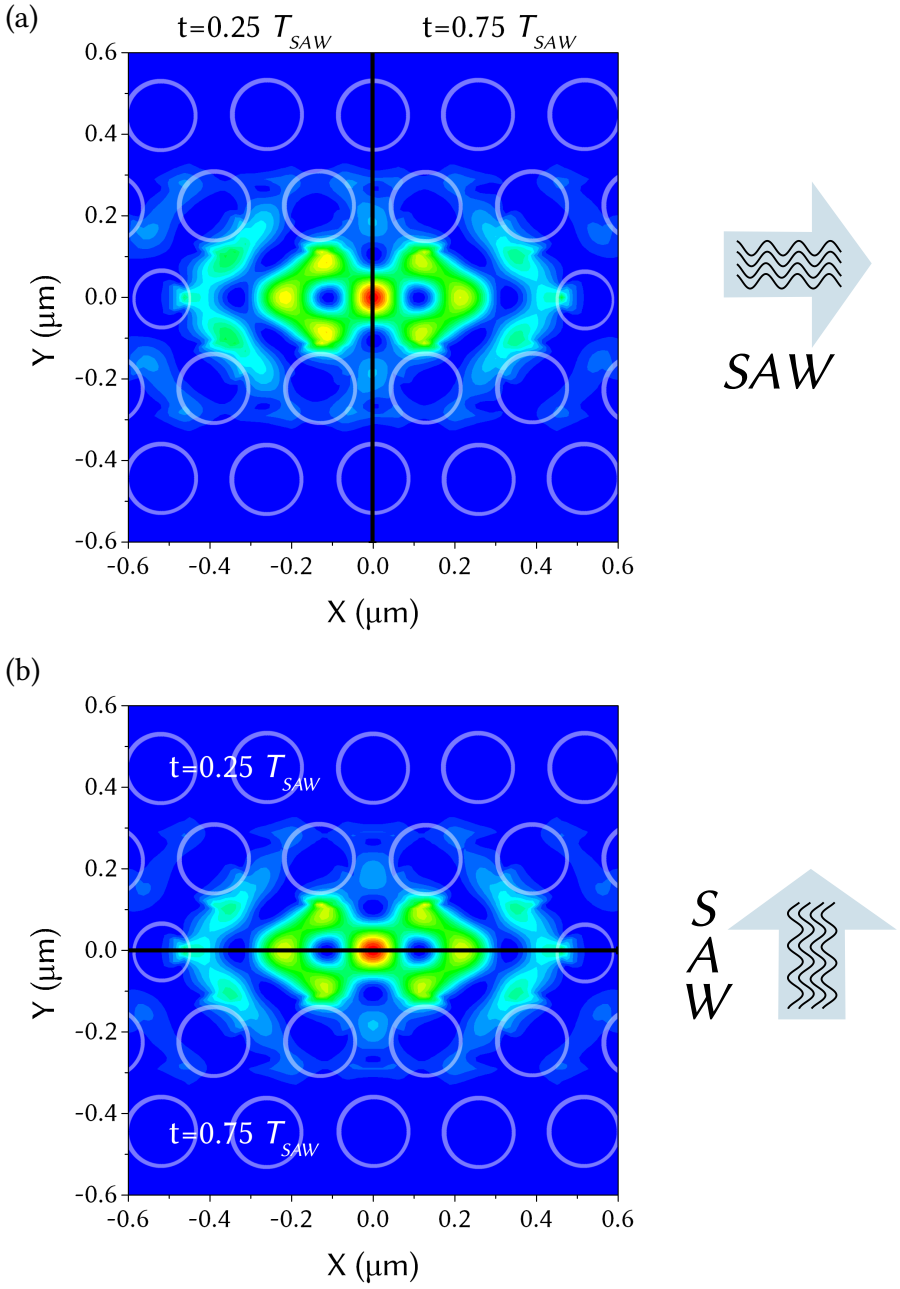

Figure 3.8 – Spatial mode profile is practically unaffected by the deformation: $\mathbf{E}(\mathbf{r})^2$ of mode $M1$ at $t = 0.25\,T_{SAW}$ (left/upper half of the plot) and $t = 0.75\,T_{SAW}$ (right/lower half of the plot) for $A_{SAW} = 1$ nm: (a) SAW propagating in x-direction, $\lambda_{SAW} = 7a$. (b) SAW propagating in y-direction, $\lambda_{SAW} = 3.2a$.

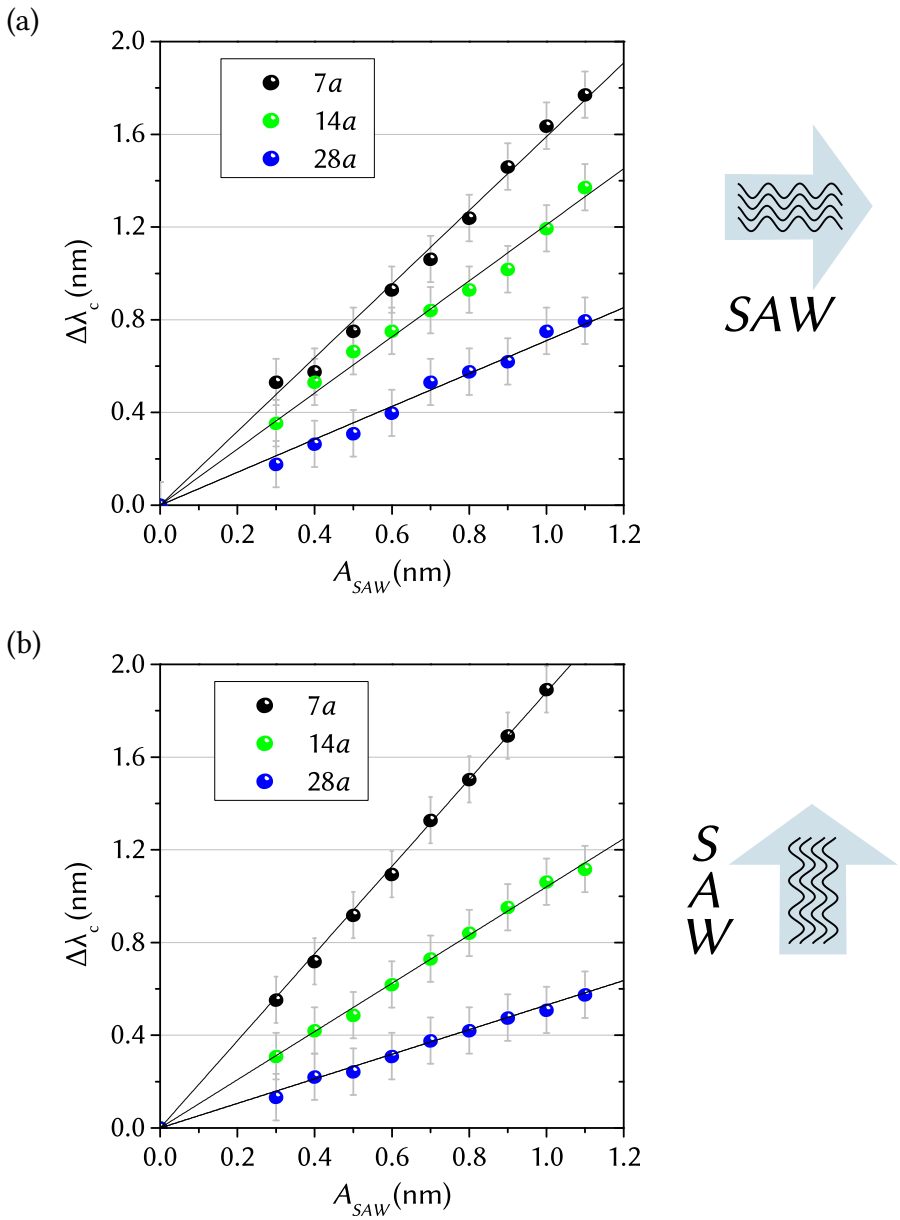

Figure 3.9 – FDTD simulation results: Linear increase of the spectral tuning range $\Delta\lambda_c$ with increasing SAW amplitude. Black lines are linear fits: (a) SAW propagating in *x*-direction, (b) SAW propagating in *y*-direction

directions of SAW propagation. A linear fit was used to quantify the change of the spectral tuning range depending of the SAW amplitude and SAW wavelength (see Tab. 3.2). This linear behavior is in concordance with the effect on the FP resonator mode for a linearly increased cavity length. Longer SAW wavelengths exhibit a smaller slope of $\Delta\lambda_c(A_{SAW})$. This accounts for a smaller change of the cavity length.

λ_{SAW}	b for $\mathbf{k}_{SAW} \parallel \mathbf{x}$	b for $\mathbf{k}_{SAW} \parallel \mathbf{y}$
$7a$	1.59 ± 0.02	1.88 ± 0.01
$14a$	1.21 ± 0.02	1.04 ± 0.01
$28a$	0.71 ± 0.01	0.53 ± 0.01

Table 3.2 – FDTD simulation results: Linear fit with $\Delta\lambda_c = b \cdot A_{SAW}$ to the simulation results of $\Delta\lambda_c(A_{SAW})$ for SAW propagating in the x and y-direction.

The SAW wavelength dependence of the spectral tuning range $\Delta\lambda_c(\lambda_{SAW})$ is shown in Fig. 3.10(a) and (b) for $A_{SAW} = 1$ nm. With $\mathbf{k}_{SAW} \parallel \mathbf{x}$, the spectral tuning range $\Delta\lambda_c$ increases exponentially with decreasing SAW wavelength down to $\lambda_{SAW} \approx 7a$. Here, $\Delta\lambda_c$ exhibits a local maximum where the SAW half-wavelength equals the cavity length $L_0 = 904$ nm$\approx 3.5a$. L_0 measures the distance between the opposing air/GaAs-interfaces at either cavity edge as depicted in Fig. 3.1. Fig. 3.10(a) also depicts the relative variation of the cavity length $\Delta L(\lambda_{SAW})/L_0$ at $t = 0.25T_{SAW}$. The cavity length changes for different λ_{SAW} according to $u_x(x,t)$ (Eq. 3.1). The relative change of the cavity length shown in Fig. 3.10(a) is calculated with the following equation for $A_{SAW} = 1$ nm:

$$f_L(\lambda_{SAW}) = \frac{\Delta L}{L_0} = \frac{1}{L_0}\left(\left|u_x\left(\frac{-L_0}{2}, \frac{T_{SAW}}{4}\right)\right| + u_x\left(\frac{L_0}{2}, \frac{T_{SAW}}{4}\right)\right) \tag{3.4}$$

This constitutes are direct comparison of the simulated results with the enhanced Fabry-Perot model (see. Eq. 3.2) where the change of the cavity length $f_L(\lambda_{SAW})$ is directly proportional to the change of the resonance wavelength. The calculated change of the cavity length is in excellent agreement with the change of the spectral tuning range for $\lambda_{SAW} \geq L_0$. Furthermore, the variation of the cavity length

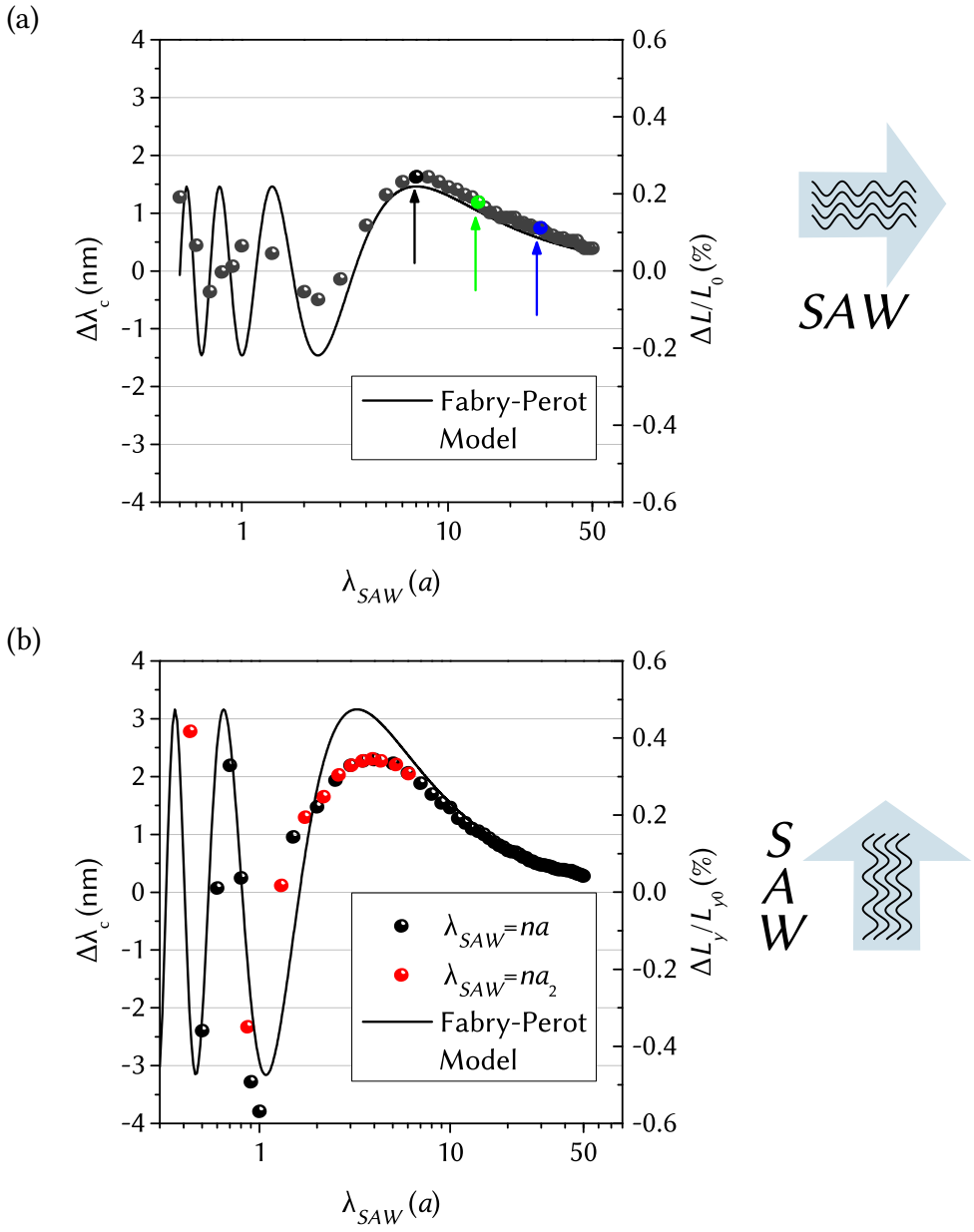

Figure 3.10 – FDTD simulation results: Variation of the spectral tuning range $\Delta\lambda_c$ as function of the SAW wavelength for $A_{SAW} = 1$ nm: (a) SAW propagating in x-direction; $\lambda_{SAW} = 7a$, $14a$ and $28a$ are marked by arrows. The black line is the relative change of the cavity length $\Delta L(\lambda_{SAW})/L_0$ calculated for $t = 0.25T_{SAW}$ and $A_{SAW} = 1$ nm using Eq. 3.4. (b) Variation of $\Delta\lambda_c$ as in (a) for SAW propagating along the y-axis of the cavity. Data points in black are calculated with λ_{SAW} being a multiple of a, whereas for the data in red the SAW wavelength is a multiple of a_2, i.e. the lattice constant in the y-direction. The black line shows the relative change of the cavity length with $L_{Fit} = 1.6a\,(1.9a_2)$ obtained by a fit to Eq. 3.4.

exhibits a phase shift of π at $\lambda_{SAW} = 3.5a$, i.e. for $L_0/2 < \lambda_{SAW} < L_0$ the cavity length is compressed at $t = 0.25T_{SAW}$. This phase shift is reproduced by the simulation. At $t = 0.25T_{SAW}$ the mode is now blue-shifted resulting in a negative spectral tuning range. With shorter SAW wavelengths ΔL and f_L change signs and are predominantly in phase. The extrema of $f_L(\lambda_{SAW})$ at $\lambda_{SAW} = \frac{4}{3}L_0 \approx 2.3a$ and $\lambda_{SAW} = 4L_0/5 \approx 1.4a$ are either not reproduced by the FDTD simulation or less pronounced for the latter. For $\lambda_{SAW} \gg L_0$ the change of the cavity length accounts well for the change of the mode wavelength.

The results for SAW propagating in the *y*-direction plotted in Fig. 3.10(b) exhibits the same qualitative change of the spectral tuning range with the SAW wavelength. The data plotted in red in Fig. 3.10(b) is intended to check for effects of a SAW wavelength commensurable with the lattice constant of the photonic crystal, e.g. the formation of a photonic superlattice. Clearly, for λ_{SAW} being a multiple of the lattice constant in the *y*-direction $a_2 = \frac{\sqrt{3}}{2}a$ the values of spectral tuning range fit to the results attained for λ_{SAW} being a multiple of a. Starting from long SAW wavelengths $\Delta\lambda_c$ increases strongly until reaching a local maximum for $\lambda_{SAW} \approx 3.5a$. Notably, this maximum does not correspond to $\lambda_{SAW} = 2 \times L_{y0} = 2.2a$, i.e. twice the short length of the L3 cavity. As shown in Fig. 3.11, the lateral distribution of the electric field in the *y*-direction expands into the area between the air-holes. It also overlaps with adjacent holes at a relative field strength of up to 63% relative to the central maximum. This may account for an effective cavity length larger than L_{y0}. In the *x*-direction the maximum relative field strength of the mode within the adjacent air-hole is only 14%. Fitting Eq. 3.4 with L_{y0} as variable parameter to the data establishes a cavity length of $L_{Fit} = 1.6a$. The cavity length resulting from the fit is in good agreement with the extent of the mode profile as shown in Fig. 3.11. The change of the spectral tuning range for long and short λ_{SAW} corresponds well with the variation of the relative cavity length $f_L(\lambda_{SAW})$ with $L_{Fit} = 1.6a$.

For long SAW wavelengths ($\lambda_{SAW} > 7a$), the spectral tuning of the cavity is equally efficient for both propagation directions. For shorter SAW wavelengths the short length of the L3 cavity exhibits a greater relative change compared to the effect of

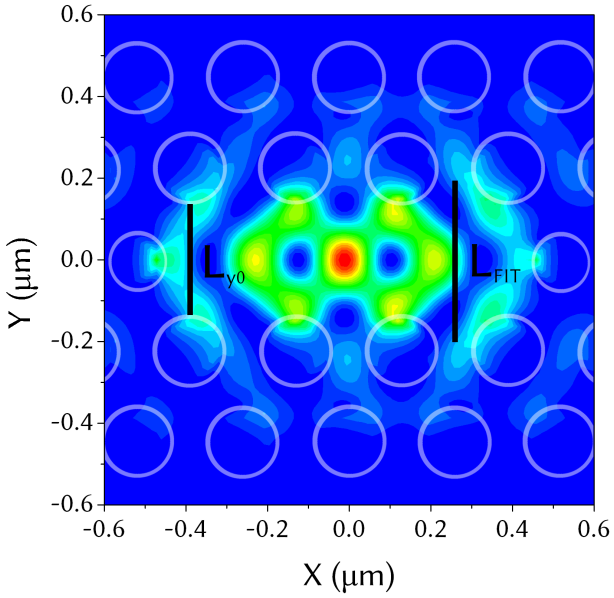

Figure 3.11 – Spatial mode profiles $\mathbf{E}(\mathbf{r})^2$ of mode $M1$ with measures for the length of the L3 cavity in the y-direction $L_{y0} = 1.1a$ and $L_{Fit} = 1.6a$ derived from a fit of $f_L(\lambda_{SAW})$ to the simulation results $\Delta\lambda_c(\lambda_{SAW})$ shown in Fig. 3.10(b).

SAW propagation in x-direction. This results in a larger spectral shift of the mode wavelength. For $\lambda_{SAW} = 2 \times L_{Fit}$ and ($\mathbf{k}_{SAW} \parallel \mathbf{y}$) the spectral tuning range $\Delta\lambda_c$ is 2.2 nm whereas for $\lambda_{SAW} = 2 \times L_0$ and ($\mathbf{k}_{SAW} \parallel \mathbf{x}$) the mode wavelength shifts by 1.6 nm.

Fig. 3.12(a) and (b) shows the relative variation of the Q-factor for different SAW wavelengths at $t = 0.25T_{SAW}$ and $t = 0.75T_{SAW}$. For long SAW wavelengths $\lambda_{SAW} > 6a$ propagating in the x-direction the Q-factor varies slightly by less than 5%. Clearly, the Q-factor changes more dramatically for $\lambda_{SAW} < L_0$. At $\lambda_{SAW} = 2a$, Q increases by more than 20% at $t = 0.75T_{SAW}$ and decreases by more than 14% at $t = 0.25T_{SAW}$. For this SAW wavelength the highest change of lattice constant a occurs. For $\lambda_{SAW} = 1a$ the position of the air-holes remain fixed and only the hole radii change. The Q-factor increases slightly by 5.4% at $t = 0.75T_{SAW}$ and decreases by 2.7% at $t = 0.25T_{SAW}$. This change supports the notion that the cavity confinement is not only controlled by the position of every hole adjacent to the cavity[95] but also the air-fill factor r/a[20]. In Fig. 3.12(b) the Q-factor

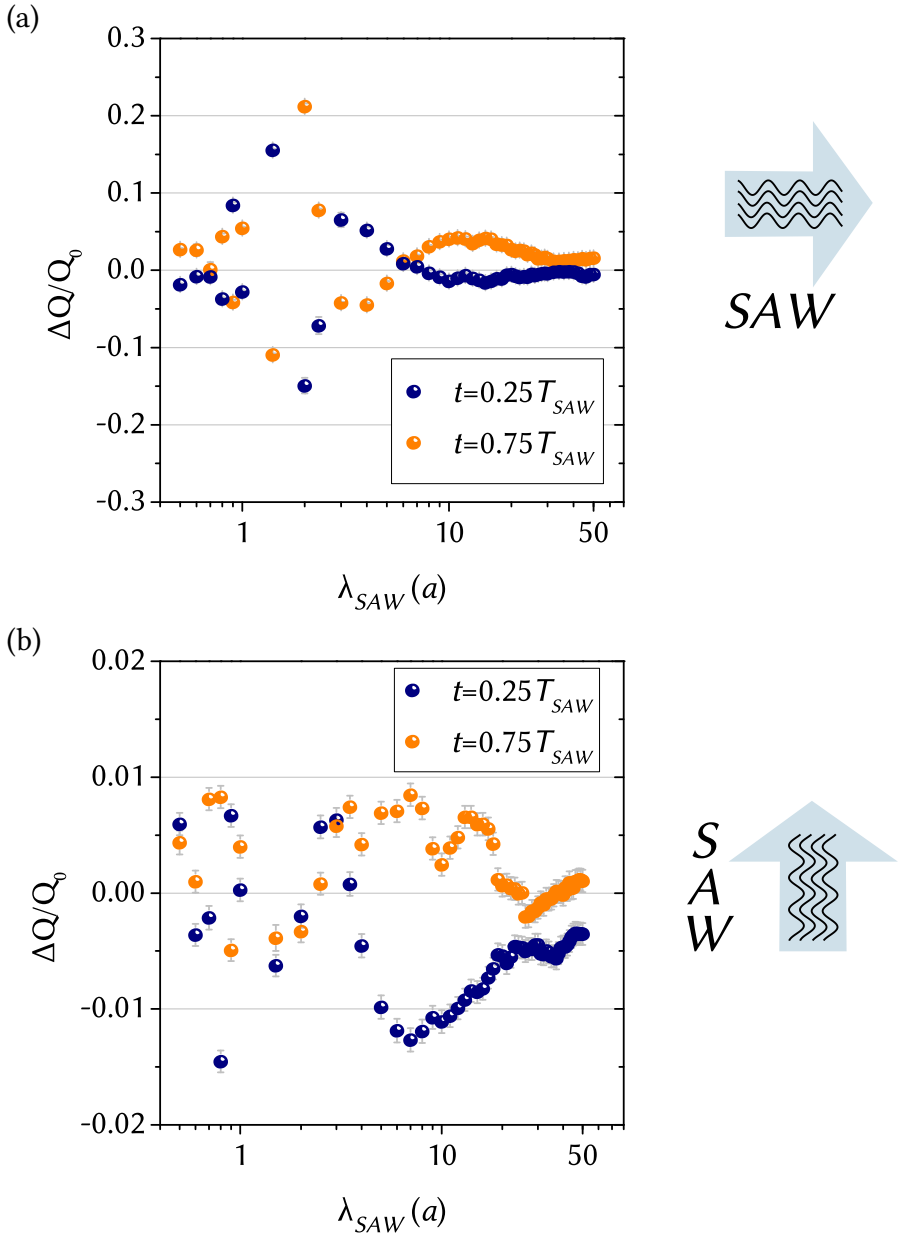

Figure 3.12 – FDTD simulation results: Relative variation of the Q-factor $\Delta Q(\lambda_{SAW})/Q_0$ at $t = 0.25T_{SAW}$ and $t = 0.75T_{SAW}$ for $A_{SAW} = 1$ nm. Plotted with error bars: (a) SAW propagating in x-direction. (b) SAW propagating in y-direction.

change for SAW propagating in the y-direction is plotted which does not exceed 1.5%. The changes are smaller compared to the values resulting from the SAW propagation along x. For $\lambda_{SAW} > 5a$ the variation of Q is less by a factor of ≈ 2. Moreover, the drastic change for smaller SAW wavelength is not reproduced. This result implies that the Q-factor is less affected by variations of the hole position and size along the y-axis. The origin of this discrepancy between the two propagation directions is not accounted for and contrasts the strong spectral shift attained with $(\mathbf{k}_{SAW} \parallel \mathbf{y})$.

3.3 Tuning of higher order cavity modes

The fundamental mode M1 of the L3 cavity is widely recognized as the best choice for cQED experiments for its high Q-factor. Non-resonant excitation of the fundamental mode via an ensemble of QDs pumped through the wetting-layer will result in a strong PL-background signal. This can be significantly reduced by resonant-pumping through a higher-order mode[96] as depicted in Fig. 3.13. This is achieved by resonantly pumping the higher order mode with a narrow-band laser. If anti-nodes of this pump mode and the fundamental mode overlap the fundamental mode is excited[97].

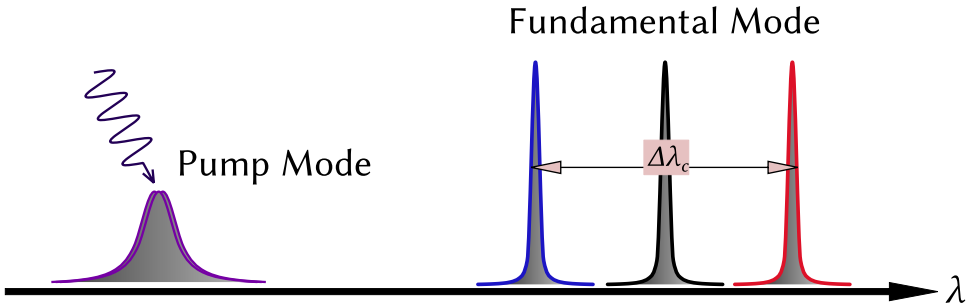

Figure 3.13 – Fundamental Mode is excited via a higher order pump mode.

Fig. 3.14 compares the mode profile of the fundamental mode $M1$ of the L3 cavity with those of its higher harmonics $M2$ and $M3$. Convoluting the respective mode profiles with that of $M1$ displays a spatial overlap with both which is more pronounced for $M3$. As shown in Tab. 3.3 $M1$ is spectrally well separated by more

Mode	λ_c	Q-factor Q_0
$M1$	954.963 ± 0.005 nm	7958 ± 7
$M2$	899.539 ± 0.005 nm	713 ± 1
$M3$	880.977 ± 0.005 nm	488 ± 3

Table 3.3 – FDTD simulation results: Wavelength and Q-factor of the first three modes of the L3 cavity.

than 50 nm from $M2$ and $M3$. This allows the fundamental mode to be pumped through $M2$ or $M3$ with a good spectral separation between the pump laser and

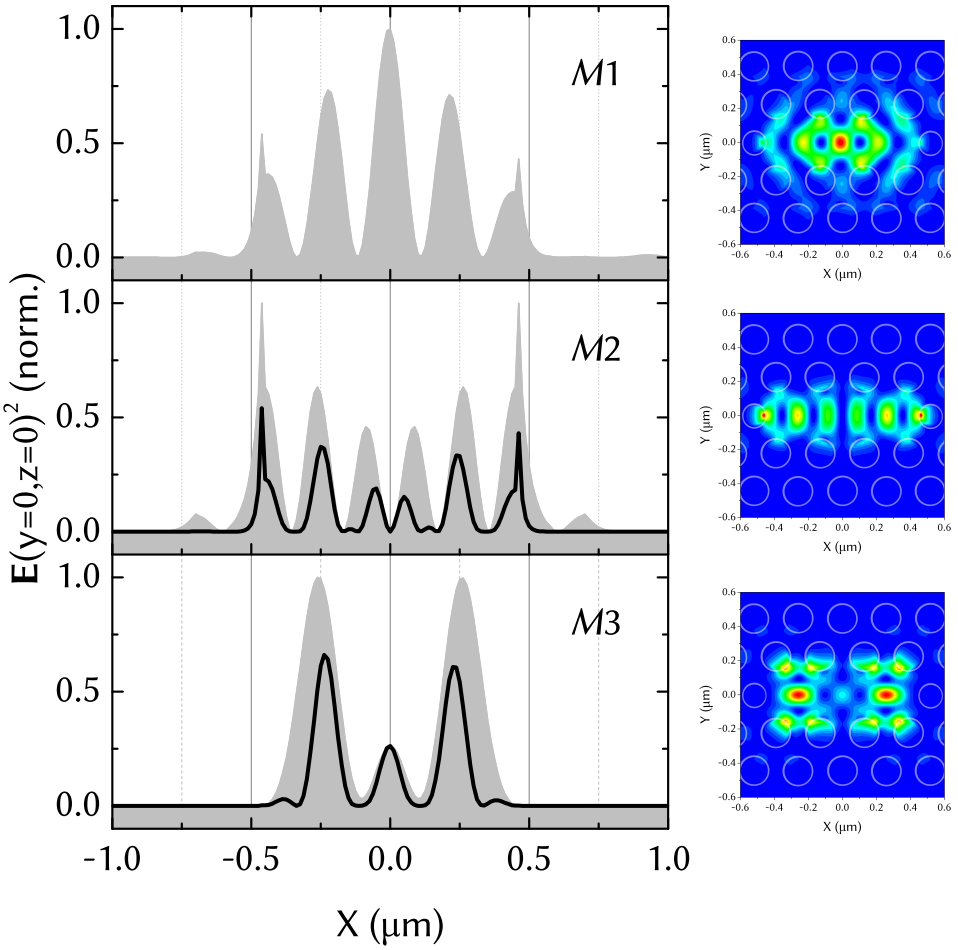

Figure 3.14 – Normalized cross sections through the spatial mode profiles $\mathbf{E}(\mathbf{r})^2$ at $y = z = 0$ of $M1$, $M2$ and $M3$. The panels of $M2$ and $M3$ also show the respective cross section convoluted with that of $M1$ (black line).

the mode. To successfully combine this resonant excitation scheme with the SAW tuning mechanism it is important to investigate how the higher order modes are shifted spectrally by the SAW in respect to a pump laser's fixed wavelength. The higher order modes are spectrally broad providing sufficient spectral overlap with the exciting laser. Consequently, a small spectral shift of the pump mode induced by the SAW does not affect the pumping efficency significantly. For the undeformed cavity the linewidths at half maximum are $\Delta\lambda_{c0} = 1.3$ nm and 1.8 nm for $M2$ and $M3$ respectively.

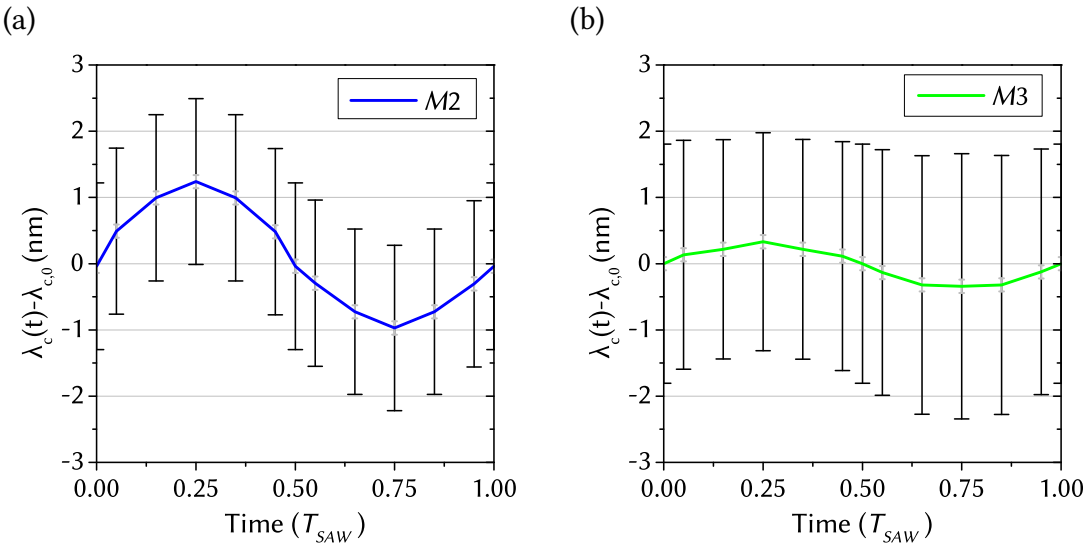

Figure 3.15 – FDTD simulation results for $\lambda_{SAW} = 7$a and $A_{SAW} = 1$ nm: Relative change of the mode wavelength $\lambda_{SAW}(t) - \lambda_{c0}$ of (a) $M2$ and (b) $M3$ with error bars in grey. The error bars in black display the spectral full width at half maximum $\Delta\lambda_{SAW}(t)$ of each mode.

The calculated spectral shift of the modes $M2$ and $M3$ with $\lambda_{SAW} = 7$a and $A_{SAW} = 1$ nm is shown in Fig. 3.15 ($\mathbf{k}_{SAW} \parallel \mathbf{x}$). For both modes the shift follows the sinusoidal deformation of the membrane in the same fashion as already seen for the fundamental mode. For $M2$ the tuning is very effective. The mode wavelength is red-shifted by more than 1.2 nm in the case of the expanded cavity while $M3$ only shifts by 0.3 nm. Fig. 3.15 also displays the spectral linewidth during the SAW period. It shows that for $M2$ the overlap of a narrow pump laser tuned to λ_{c0} is expected to vary substantially. $M3$ is much less affected by the SAW providing a perpetual laser overlap ideal for pumping the fundamental mode via this mode.

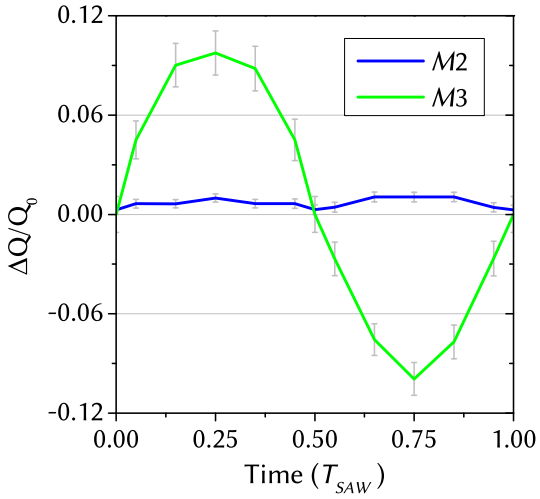

Figure 3.16 – FDTD simulation results for $\lambda_{SAW} = 7a$ and $A_{SAW} = 1$ nm: Relative change of the Q-factor for the modes $M2$ and $M3$.

The Q-factor change of $M2$ during the SAW period presented in Fig. 3.16 shows only a negligible change of less than 1.5%. Whereas the Q of $M3$ changes sinusoidally with an amplitude of $> 10\%$. The Q-factor change of $M3$ is shifted by half a SAW period in respect to that of the fundamental mode, i.e. the Q of $M3$ has its maximum at $t = 0.25\,T_{SAW}$ and its minimum at $t = 0.75\,T_{SAW}$. This could account for the different spectral position of each mode within the photonic bandgap and the ramifications of an oscillating air-fill factor r/a.

Fig. 3.17 displays the spatial mode profile of $M2$ and $M3$ of the deformed cavity at same SAW wavelength and amplitude. For both modes the position of the anti-nodes of the expanded cavity does not differ from the position of the compressed cavity. This consistency ensures constant spatial overlap with the anti-nodes of the fundamental mode which is a key requirement for resonant pumping.

For the fundamental mode $M1$ an increase of the SAW amplitude resulted in a linear increase of the spectral tuning range. The higher order modes exhibit a consistent behavior (Fig. 3.18). A linear fit to the simulation results shows that the slope of spectral tuning range of $M2$ exceeds that of $M1$ and $M3$ for $\lambda_{SAW} = 7a$, $14a$ and $28a$ (see Tab. 3.4).

Investigating a broader range of SAW wavelengths shows that $M2$ exhibits the strongest spectral shift of all three mode for $\lambda_{SAW} > 6a$ (see Fig. 3.19). $M3$ is

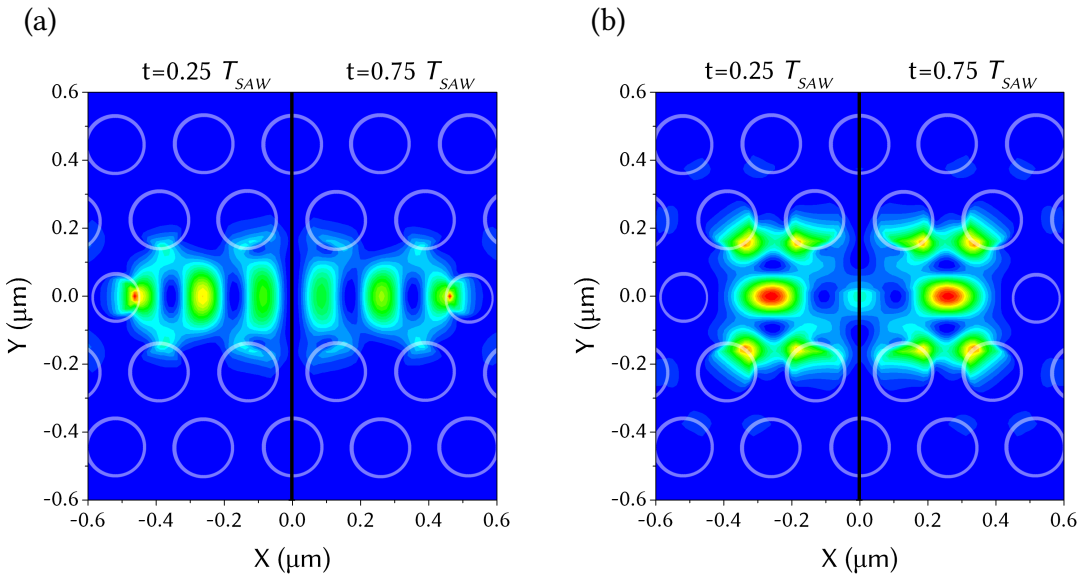

Figure 3.17 – Spatial mode profiles $|\mathbf{E}^2(\mathbf{r})|$ at $t = 0.25T_{SAW}$ (left half of each plot) and $t = 0.75T_{SAW}$ (right half of each plot) with $\lambda_{SAW} = 7a$ and $A_{SAW} = 1$ nm: (a) $M2$ and (b) $M3$.

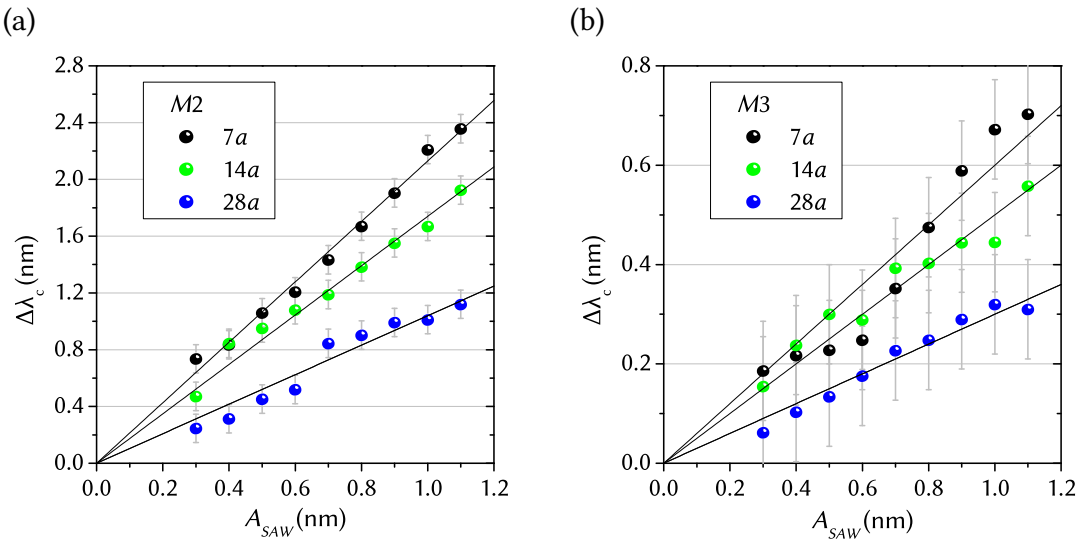

Figure 3.18 – FDTD simulation results: Dependence of the spectral tuning range $\Delta\lambda_c$ on the SAW amplitude for $\lambda_{SAW} = 7a$, $14a$ and $28a$: (a) $M2$ and (b) $M3$. The black lines are linear fit curves.

Mode	$\lambda_{SAW} = 7a$	$14a$	$28a$
$M1$	1.59 ± 0.02	1.21 ± 0.02	0.71 ± 0.01
$M2$	2.13 ± 0.03	1.74 ± 0.03	1.04 ± 0.04
$M3$	0.60 ± 0.03	0.50 ± 0.02	0.30 ± 0.01

Table 3.4 – Fit parameter b of the linear fit $\Delta\lambda_c = b \cdot A_{SAW}$ to the simulation results of $\Delta\lambda_c(A_{SAW})$ in Fig. 3.18.

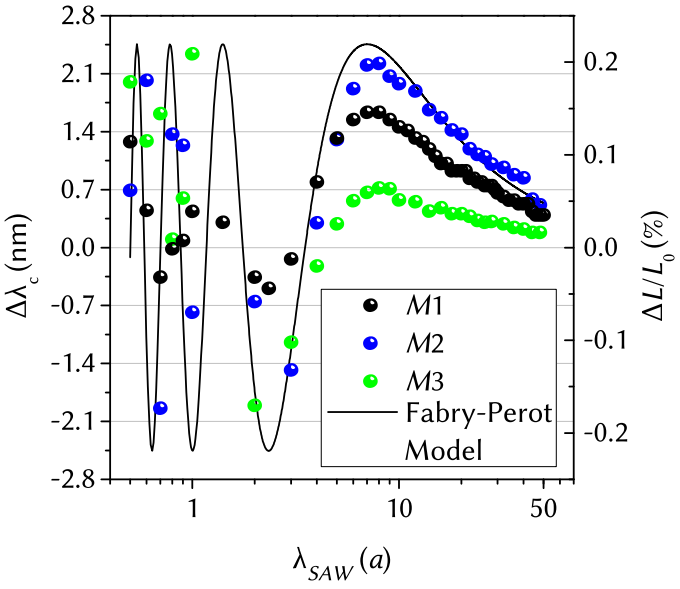

Figure 3.19 – FDTD simulation results: Variation of the spectral tuning range $\Delta\lambda_c$ as function of the SAW wavelength at $A_{SAW} = 1$ nm. The black line is the relative change of the cavity length $\Delta L(\lambda_{SAW})/L_0$ calculated for $t = 0.25\,T_{SAW}$ and $A_{SAW} = 1$ nm as described in Eq. 3.4.

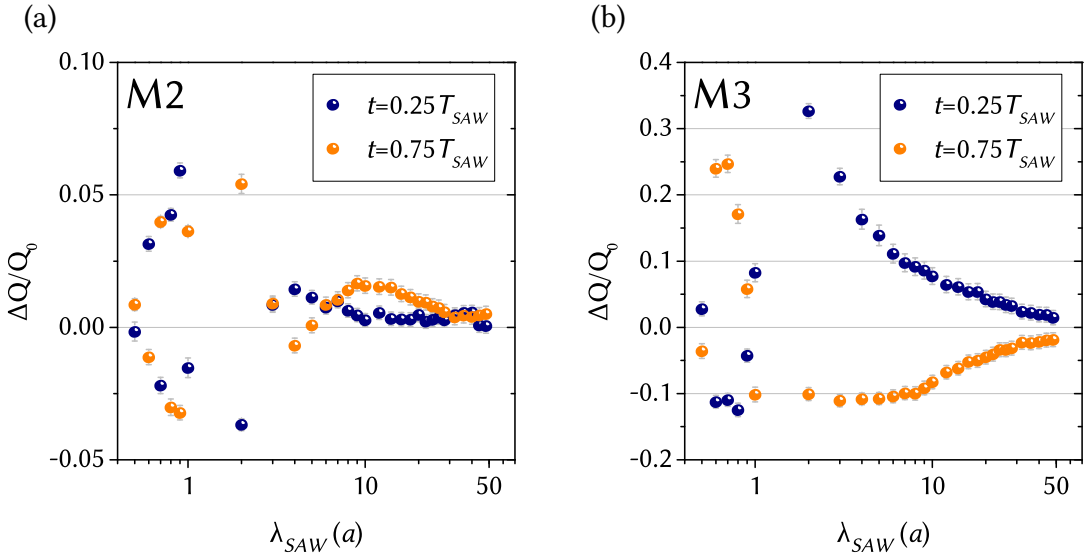

Figure 3.20 – FDTD simulation results: Relative variation of the Q-factor change ($\Delta Q = Q_c(t) - Q_{c,0}$) at $t = 0.25\,T_{SAW}$ and $t = 0.75\,T_{SAW}$ for $A_{SAW} = 1$ nm. Plotted with error bars: (a) $M2$ and (b) $M3$.

significantly less susceptible to deformations than $M2$ and $M1$. Moreover, the slope of $\Delta\lambda_c(\lambda_{SAW})$ for $M3$ deviates from $M1$ and $M2$. This difference in the spectral tuning range is proportional to the extent of the spatial mode profile in the x-direction. For $M3$ the anti-nodes are at a distance of more than 200 nm from the air-holes at the cavity edges (see Fig. 3.14). Consequently, a shift of these holes by up to A_{SAW} has a smaller effect on $M3$ than $M2$ where the mode profile spreads over the entire cavity length. All modes exhibit an increased spectral shift at smaller SAW wavelengths. In respect to the proposed remote pumping of the fundamental mode via $M3$ it is evident that the spectral tuning range does not exceed the linewidth of $M3$ for $\lambda_{SAW} > 3a$.

The change of the linewidth, i.e. the change of the Q-factor, is plotted in Fig. 3.20. For $M2$ the relative difference of the Q-factor is small for long SAW wavelengths ($\lambda_{SAW} > 5a$) for the compressed and the cavity. ΔQ increases proportional to the spectral tuning range. At shorter wavelength the variation is slightly pronounced with a maximum of less than 6% at $\lambda_{SAW} = 0.9a$. $M3$ on the other hand shows a different behavior in this respect depicted in Fig. 3.20(b). Here, a strong increase of the Q-factor at $t = 0.25\,T_{SAW}$ is calculated inversely proportional to the SAW wave-

length which peaks at $\Delta Q > 30\%$ for $\lambda_{SAW} = 2a$. For shorter SAW wavelengths this relation breaks abruptly. The Q-factor decrease at $t = 0.75 T_{SAW}$ shows the same dependence on long SAW wavelengths but saturates for $1a < \lambda_{SAW} < 8a$. On the whole, resonant pumping the fundamental mode via a higher order mode of the L3 cavity while manipulating $M1$ with SAW is feasible. $M3$ shows excellent qualities in this aspect. The spectral tuning range exceeding the mode linewidth occurs only for short SAW wavelengths $\lambda_{SAW} < 3a$ and high SAW amplitudes.

4 Stroboscopic and time-resolved experiments

4.1 Full time domain stroboscopic experiments

To resolve the full dynamics of the spectral mode shift, a SAW phase-locked full time domain stroboscopic measurement technique is used[75]. Here, the laser pulse repetition rate is adjusted for the SAW frequency to be an integer multiple. The laser pulses are triggered to be generated at a fixed time within the SAW period for each time-integrated measurement (see Fig. 6.3 in the appendix). This delay time is subsequently swept over the entire SAW period phase-resolving the change of the mode position. The following experimental results are published in [84]. The result of this measurement technique at $f_{SAW} = 414$ MHz and $P_{RF} = 32$ dBm plotted in Fig. 4.1 shows the full dynamics of the mode shift. The sinusoidal shift of the mode resulting from the FDTD simulations is excellent accordance with the experiment (see. Fig. 4.2). Moreover, the extracted mode wavelengths confirm the sinusoidal oscillation around the wavelength of the unperturbed cavity $\lambda_c = 917.45$ nm. A total spectral shift of $\Delta\lambda_c = 1.2$ nm is achieved. The mode dynamics are in excellent agreement with FDTD calculations using a SAW amplitude $A_{SAW} = 1.9$ nm.

According to the FDTD simulation, the Q-factor is expected to vary by 6%. This is in good agreement for $t = 0.25\,T_{SAW}$ and $t = 0.75\,T_{SAW}$ shown in Fig. 4.3 where the Q-factor change is within a few percent. Nevertheless, the experiment exhibits a strong decrease of Q for $t = 0\,T_{SAW}$ and $t = 0.5\,T_{SAW}$. The Q-factor extracted from the measurements shows a periodic degradation of up to 60% from the value

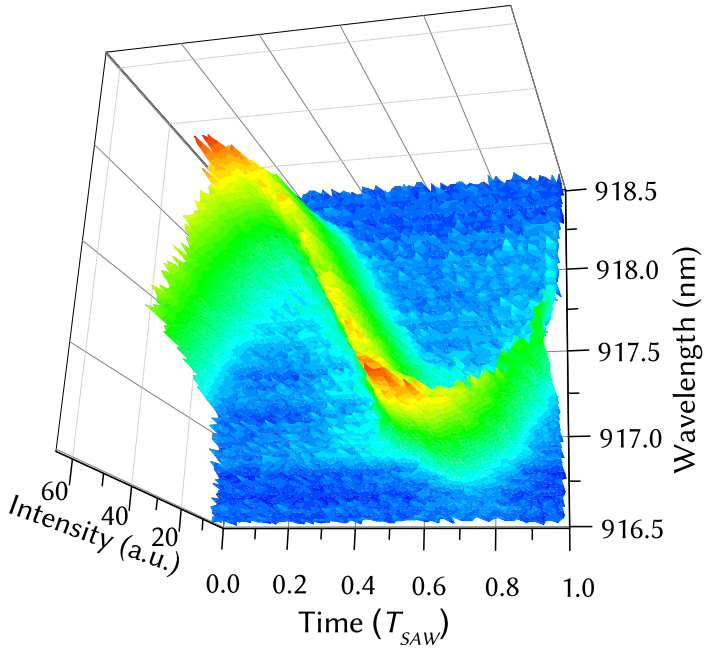

Figure 4.1 – Stroboscopic measurement of the sinusoidal variation of the mode wavelength at $f_{SAW} = 414$ MHz and $P_{RF} = 32$ dBm.

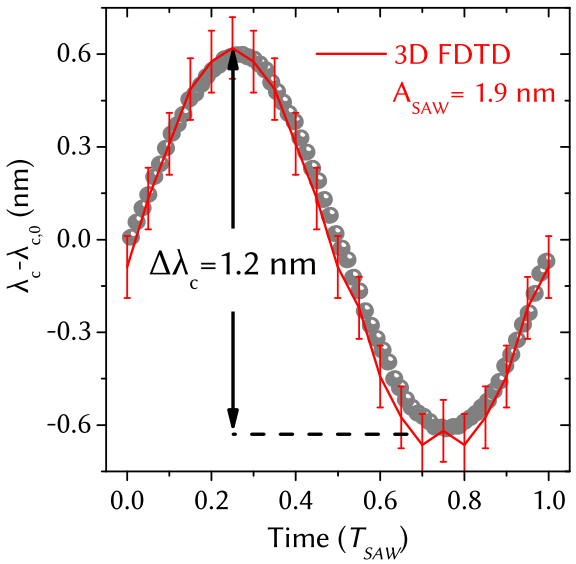

Figure 4.2 – Extracted mode position and FDTD simulation of the spectral shift for $\lambda_{SAW} = 28a$ and $A_{SAW} = 1.9$ nm.

of the unperturbed cavity of $Q_0 \approx 5000$. At these times, the deformation of the

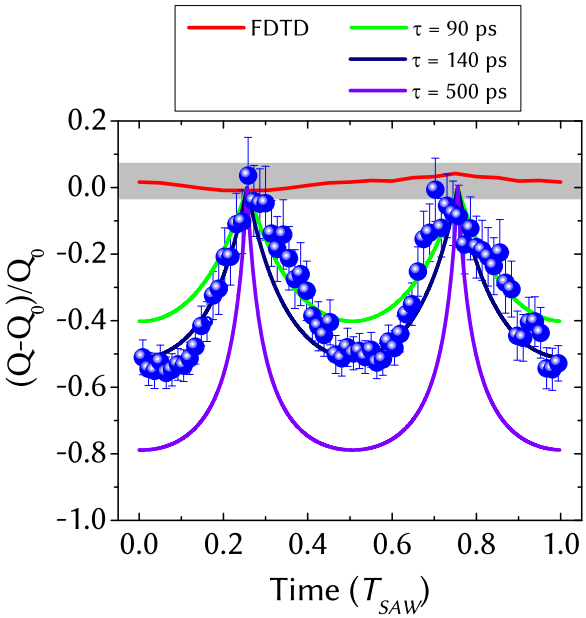

Figure 4.3 – Q-factor change extracted from the measurement in Fig. 4.2. The nominal Q-factor variation depends on the temporal resolution of the stroboscopic measurement denoted by τ. FDTD-calculations exhibit a small Q-factor variation $< 6\%$ (red line).

cavity and the Q-factor variation should be minimum according to the simulation. The additional broadening of the mode is an artifact of the time-integrated stroboscopic measurement. The timescale of the experimental setup and radiative decay processes define the maximum temporal resolution τ of the measurement. These resolution limitations stem from the laser pulse duration and the Purcell-enhanced radiative decay of the QDs. The time dependent spectral shift-rate of the mode is given by:

$$\left|\frac{d\lambda_c}{dt}\right| = 2\pi f_{SAW} A_0 \left|cos(2\pi f_{SAW} t)\right| \tag{4.1}$$

A_0 is 50% of the spectral tuning range. The spectral shift of the mode within the temporal resolution τ will additionally broaden the measured lineshape. Consequently, for a high spectral shift rate the mode will appear spectrally broadened compared to times of a low rate within the SAW period. On small timescales $< T_{SAW}/4$ a linear interpolation is valid and gives the resulting broadening $\delta\lambda_c$:

$$\delta\lambda_c \approx \left|\frac{d\lambda_c}{dt}\right| \tau \tag{4.2}$$

With the Q-factor of the unperturbed cavity $Q_0 = \lambda_{c,0}/\delta\lambda_{c,0}$ the nominal Q-factor modulation is:

$$\frac{Q - Q_0}{Q_0} = \frac{-\delta\lambda_c}{\delta\lambda_{c,0} + \delta\lambda_c} \tag{4.3}$$

The full expression plotted in Fig. 4.3 is:

$$\frac{Q - Q_0}{Q_0} = \frac{-2\pi f_{SAW} A_0 |cos(2\pi f_{SAW} t)|\tau}{\delta\lambda_{c,0} + 2\pi f_{SAW} A_0 |cos(2\pi f_{SAW} t)|\tau} \tag{4.4}$$

The maximum time resolution of the setup determined by the laser pulse duration $\tau = 90$ ps results in the nominal Q-factor modulation plotted in green (Fig. 4.3. The experimentally acquired variation of the Q-factor is well described by $\tau = 140$ ps which includes the Purcell enhanced radiative decay of QDs coupled to the mode of $\approx$ 50ps. As a results, the broadening of the mode in Fig. 4.2 can be justified by the temporal resolution of the experimental setup. The Q-factor of the mode is maintained.

At higher SAW frequencies and higher tuning rates $|d\lambda_c/dt|$ the effect of this artifact becomes more pronounced. Consequently, using this stroboscopic measure-

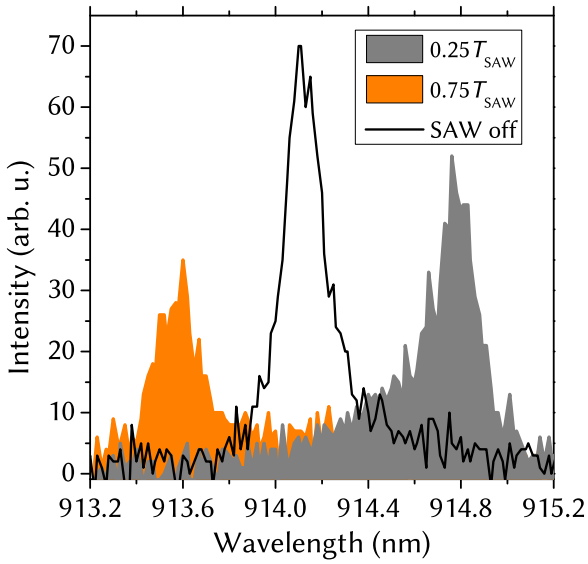

Figure 4.4 – Stroboscopic measurement of the mode at $t = 0.25T_{SAW}$ and $t = 0.75T_{SAW}$ at $f_{SAW} = 850$ MHz and $P_{RF} = 28$ dBm. An artifact of the tuning causes the asymmetric lineshape. The cavity mode without the SAW is plotted in black.

ment at $f_{SAW} = 850$ MHz results in asymmetric lineshapes. In Fig. 4.4 measurements of the mode at $t = 0.25\,T_{SAW}$ and $t = 0.75\,T_{SAW}$ are plotted. Here, the slow QD decays contribute to the PL signal which broadens the mode along the tuning direction of the mode.

The sinusoidal shift of the mode is equally well resolved for low and high RF powers. Fig. 4.5 depicts the mode shift with increasing RF power 5 dBm $\leq P_{RF} \leq$ 29

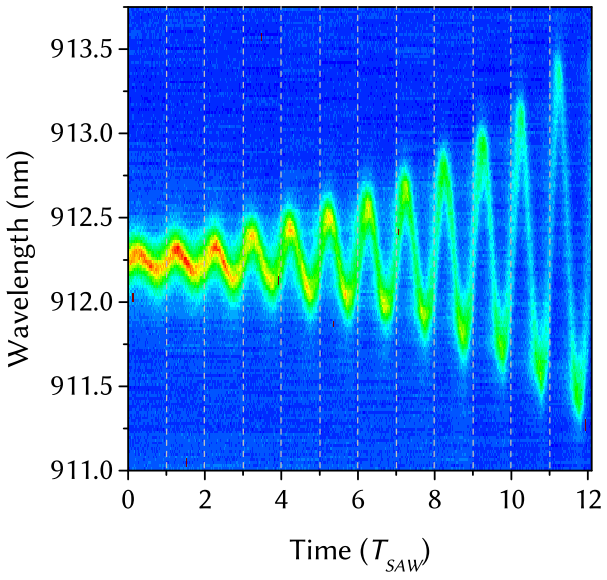

Figure 4.5 – Stroboscopic measurement of the mode shift at $f_{SAW} = 415$ MHz ($P_0 = 5$ dBm) with incremental increase of the RF power by $\Delta P_{RF} = 2$ dBm after each SAW period (white line).

dBm. The RF power is increased after each SAW period by $\Delta P_{RF} = 2$ dBm. The spectral tuning rate $\Delta\lambda_c$ exhibits the same increase observed in the power-dependent time-integrated measurements confirming the linear increase $\propto \sqrt{P_{RF}}$ (see. Fig. 2.8).

The stroboscopic measurements reveal an important property of the QDs inside the photonic crystal nanocavity. As described in Chap. 1.2, the spectral lifetime of the QDs decreases substantially due to the Purcell effect when spatially and spectrally coupled to an optical mode. On the other hand, when the QDs inside the cavity are being decoupled from a mode the absence of photonic states inside the photonic bandgap causes the lifetime to increase (see Fig. 4.6. The mode ob-

served in the spectra of the time-integrated PL measurements originates from the enhanced extraction efficiency from the QDs coupled to the mode. The decay of QDs not coupled to the mode is inhibited and returns a weak PL-signal. The rise of the extraction efficiency by coupling the emitter to a microcavity can be more than an order of magnitude[98]. The mode resonance wavelength will oscillate due to the mechanical deformation of the membrane by the SAW. As a result, the QDs spectrally within $\lambda_{c,0} \pm \Delta\lambda_c/2$ will eventually couple to the mode during the SAW period. After an initial slow decay with a spectral lifetime of several ns[20] the decay rate will increase (see next chapter for time-resolved measurements). Hence, every QD spatially coupled to the mode within the spectral tuning range is expected to cause a strong signal due to the Purcell-enhanced extraction efficiency with in the first SAW period after excitation. Instead of a well-resolved mode at $\lambda_c(t)$ in the time-integrated spectrum of the stroboscopic measurements a band of high PL intensity with the width of $\Delta\lambda_c$ would be observed. Clearly, this is not the case as the spectral oscillation of the mode is well resolved. The presented stroboscopic measurements support the conclusion that the QDs spectrally not overlapping with the mode at the time of excitation emit into the mode via non-resonant QD-cavity coupling. Non-resonant coupling and its mechanisms have been under controversial discussion in the recent years. The fast dephasing of the QDs is thought to be mediated by the emission or absorption of acoustic phonons[99]. Other contributions discussed are Coulomb scattering[100] and transitions between excited multiexciton states[101].

Overall, the presented time-integrated experiments established excellent qualities of the surface acoustic tuning mechanism for solid-state cQED experiments. With a demonstrated spectral tuning range of 1.5 nm, the SAW can dynamically couple and decouple the nanocavity mode to a single QD. Moreover, by changing the sample temperature the initial mode wavelength in respect to the QD is set. Thus, full control of the spectral overlap, the coupling strength and the tuning rate is gained. The mode tuning rate $|d\lambda_c/dt|$ determines how long the mode strongly couples to the QD. This rate is also controlled by the RF power applied to IDT which determines the spectral tuning range as confirmed by RF power-dependent

measurements. Additionally, the SAW acoustic wave does not degrade the Q-factor significantly. Only minor variations within a few percent occur. This property is very important since a high-Q of the cavity is a prerequisite for the strong coupling regime.

4.2 Time-resolved experiments

In Chapt. 2.2, the properties and effectiveness of the photonic SAW-based tuning scheme are demonstrated and investigated in time-integrated experiments. In the previous chapter, phase-resolved stroboscopic measurements [75] confirmed the FDTD-simulated dynamics of the mode. The time-resolved dynamic change of the emitter-cavity-coupling will be the subject of this chapter. Time-correlated single photon counting (TCSPC) measurements using a fast photon detector disclose the nature of the QD decay, i.e. slow decay and fast Purcell-enhanced decay. Its manipulation is demonstrated by spectrally changing the mode wavelength with the SAW. This tuning mechanism could be used to create a deterministic single-photon source emitting with an arbitrary pulse period, i.e. at the period of the surface acoustic wave. Moreover, by shifting the event of the exciting laser pulse within the SAW period the time resolution of the TCSPC measurement can be improved.

The presence of a photonic crystal material and a cavity has a great impact on the local density of optical states. The spectral decay characteristics of InAs QDs at different positions on the PCM are presented in Fig. 4.6. The spectral lifetimes established from these measurements are given in Tab. 4.1. Fig. 4.6(a) shows the monoexponential decay of a QD inside the unpatterned GaAs resulting in a spectral lifetime of $\tau = 0.63 \pm 0.01$ ns. This plot also shows the *Instrument Response Function* (IRF) of the experimental setup (see appendix). Main contributions to the IRF are the laser pulse duration of 90 ps and the time resolution of the avalanche photo diode (< 50 ps) and the photon counting system (32 ps). For the fit curves shown

InAS QD environment	τ/τ_1 [ns]	τ_2 [ns]
bulk GaAs	0.63 ± 0.01	N/A
L3 cavity	2.94 ± 0.19	0.19 ± 0.01
photonic crystal	3.78 ± 0.06	N/A

Table 4.1 – Spectral lifetimes of InAs QDs extracted from the decays shown in Fig. 4.6 (a),(c) and (d).

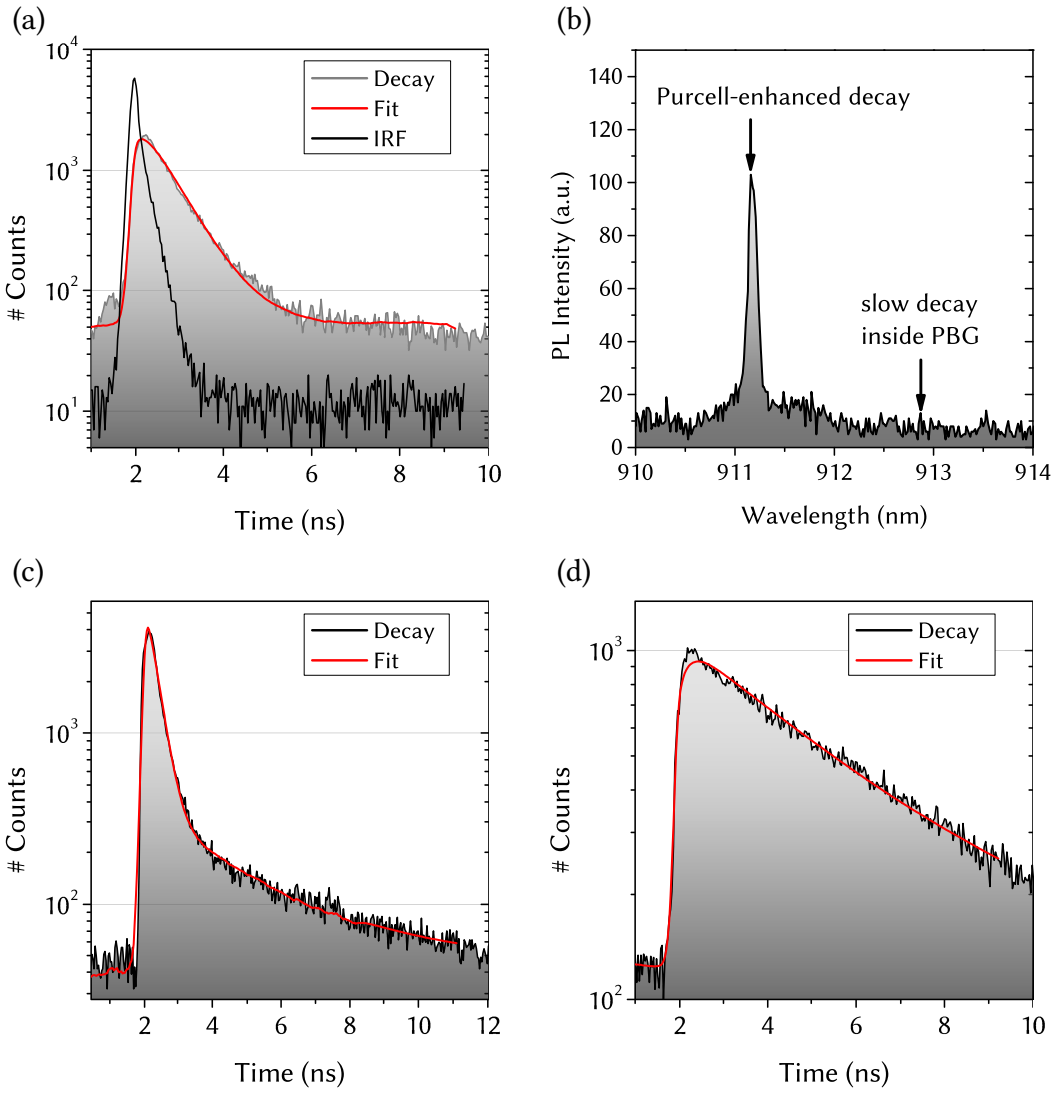

Figure 4.6 – Time-resolved decay transients and fits deconvoluted from the instrument response function (IRF): (a) QD on the unpatterned GaAs also showing the IRF, (b) PL spectrum indicating the spectral position of the measurements shown below, (c) Purcell-enhanced decay of QD coupled to cavity mode, (d) slow decay of QD spectrally inside the photonic bandgap (PBG).

in this figure the IRF is deconvoluted from the decay curves. Fig. 4.6(b) indicates the spectral position of the detector for the measurements below. For Fig. 4.6(c) a decay transient is recorded spatially at the center of the cavity and spectrally at the mode wavelength. Here, the decay characteristics are described by a biexponential decay. The fast decay with a spectral lifetime of $\tau_2 = 0.19 \pm 0.01$ ns is the Purcell-enhanced decay. When weakly coupled to a cavity an increased number of optical states becomes available to the quantum emitter increasing the emission rate by the Purcell-factor $F_p = \frac{3Q}{4\pi^2 V_{Mode}}$ (Q: quality factor; V_{Mode}: mode volume; see Eq. 1.10 in Chap. 1.2). A comparison with the spectral lifetime of the QD in the unpatterned GaAs yields an increase of the recombination rate by a factor of $F_p > 3$. The long time constant $\tau_1 = 2.94 \pm 0.19$ ns of the biexponential decay originates from QD decays which are not spatially coupled to the cavity [20]. The lifetime increases drastically if the QD is inside the photonic bandgap. As described in Chap. 1.3, no optical states are available to the emitter since the photonic density of states is zero inside the bandgap [31]. This reduces the spontaneous emission rate significantly resulting in a long spectral lifetime of $\tau = 3.78 \pm 0.06$ ns (Fig. 4.6(d)).

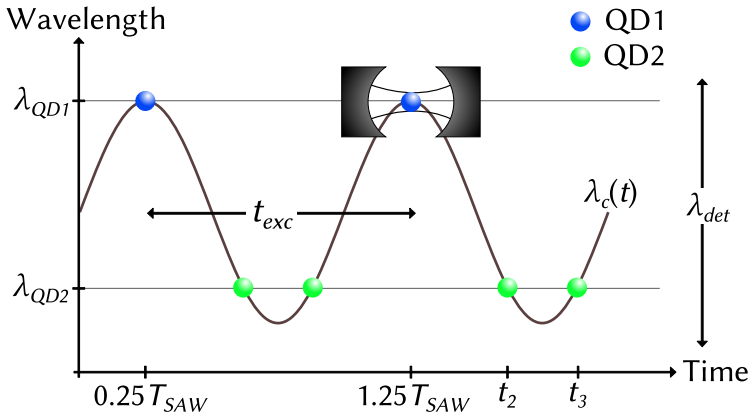

Figure 4.7 – The diagram shows the range of the two important parameters of the time-resolved experiments. The excitation time of the InAs QDs within the SAW period t_{exc} and the detector wavelength λ_{det}. As the SAW tunes the mode wavelength $\lambda_c(t)$ a QD couples to it if $\lambda_c(t_{couple}) = \lambda_{QD}$.

In the following time-resolved measurements, two parameters are controlled to investigate the dynamic coupling of the mode and a QD: the observed wavelength

of the fast detector λ_{det} and the occurrence of the laser pulse in respect to the beginning of the SAW period, i.e. the excitation time t_{exc}. The diagram in Fig. 4.7 shows the sinusoidal course of the mode $\lambda_c(t)$, i.e. how the surface acoustic wave tunes the mode wavelength λ_c. The spectral position of quantum dot QD1 is at the most red-shifted wavelength of the mode at $\lambda_c(t = 0.25T_{SAW}) = \lambda_{QD1}$. A QD will have a long spectral life time due to the photonic bandgap effect unless $\lambda_c(t_{couple}) = \lambda_{QD}$. Thus, if the detector wavelength λ_{det} is set to λ_{QD1} an increased photon count will be registered at time $t = 0.25T_{SAW}$. In that instance the spontaneous emission rate will be Purcell-enhanced as QD1 and the cavity mode couple. A quantum dot at a maximum of $\lambda_c(t)$ will couple once to the mode every SAW period. Quantum dot QD2 does not coincide with the most blue-shifted position of the mode at $\lambda_c(t = 0.75T_{SAW})$. Consequently, QD2 couples to the mode twice during the SAW period at times t_2 and t_3.

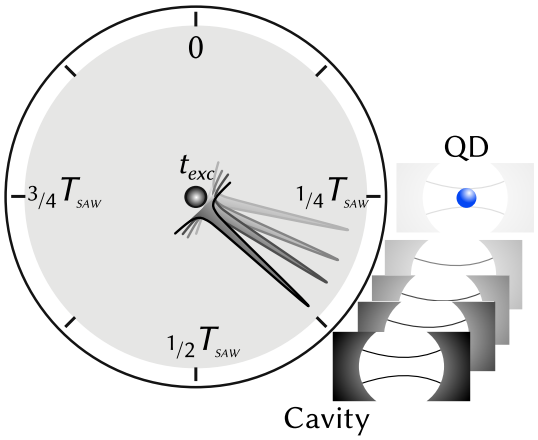

Figure 4.8 – The Purcell-enhanced decay will take place during the SAW period whenever the coupling condition $\lambda_c(t_{couple}) = \lambda_{QD}$ is fulfilled. This decay is delayed by Δt after the excitation at t_{exc} within the SAW period unless $t_{couple} = t_{exc}$: $\Delta t = \left[\left(\frac{t_{couple}-t_{exc}}{T_{SAW}}\right) \mathit{modulo}\, 1\right] T_{SAW}$. For a laser pulse at $t_{exc} = 0.35T_{SAW}$ and a QD coupling to the mode at $t = 0.25T_{SAW}$ the time interval between excitation and coupling condition is $\Delta t = 0.9T_{SAW}$.

In the following measurements, the wavelength λ_{det} of the fast detector is set to a wavelength within the spectral tuning range of the mode, e.g. $\lambda_{det} = \lambda_c(t = 0.25T_{SAW})$. The decay rate measured by the detector will be Purcell-enhanced and fast when the mode overlaps with the emitter observed at λ_{det}. The decay will

be slow due to the photonic bandgap effect for the mode being spectrally detuned from λ_{det}. As illustrated in Fig. 4.8 the sample can be excited at an arbitrary excitation time t_{exc} during the SAW period. For $t_{couple} = 0 \times T_{SAW}$ the mode is spectrally overlapping with the emitter at the beginning of the SAW period. For $t_{exc} = t_{couple}$ the Purcell-enhanced decay will occur right at the moment of excitation. At other times it will take

$$\Delta t = \left[\left(\frac{t_{couple} - t_{exc}}{T_{SAW}} \right) \textit{modulo}\, 1 \right] T_{SAW} \tag{4.5}$$

for the mode to be tuned to the emitter and the spontaneous emission rate increases.

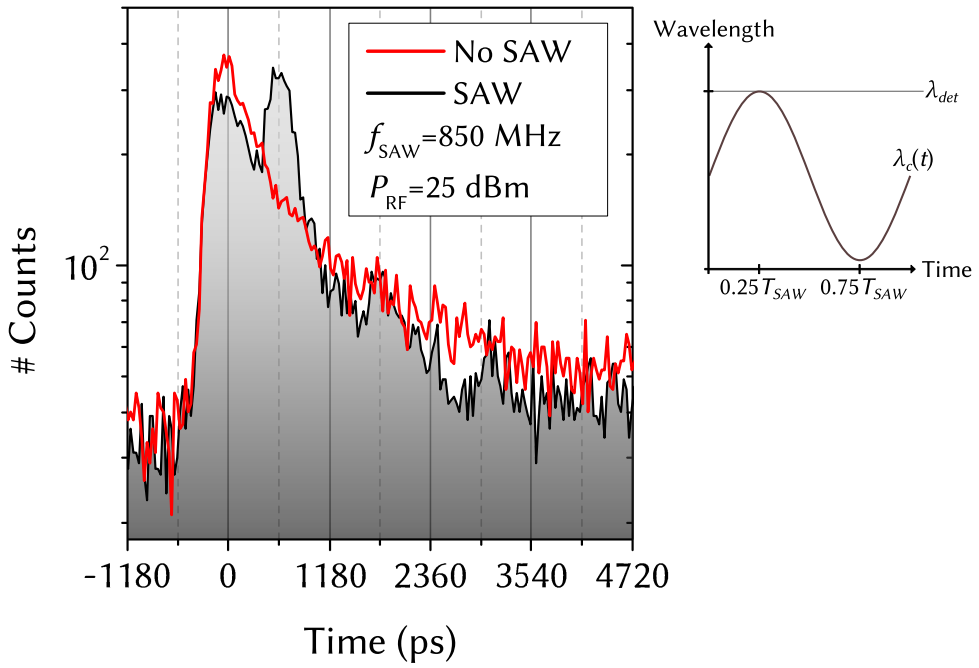

Figure 4.9 – Decay transients recorded at $\lambda_{det} = \lambda_c(t = 0.25T_{SAW}) = \lambda_{c,0} + 0.6$ nm. The decay transient in black is recorded under the influence of a surface acoustic wave ($f_{SAW} = 850$ MHz, $P_{RF} = 25$ dBm) with $t_{exc} = 0.75T_{SAW}$. The transient in red is a reference measurement recorded without SAW.

Fig. 4.9 shows the dynamic coupling between QD and cavity at a rate of $f_{SAW} = 850$ MHz at $P_{RF} = 25$ dBm and a reference measurement without SAW. As in the stroboscopic measurements in the previous chapter, the SAW frequency is an integer multiple of the arbitrary laser repetition rate, i.e. the time of the laser pulse is fixed

in respect to the SAW period. Here, the excitation time is set to $t_{exc} = 0.75\,T_{SAW}$. The unperturbed cavity mode wavelength is at $\lambda_{c,0} = 913.8$ nm and has a Q-factor $Q = 3700$. The detector is spectrally set to record at $\lambda_{det} = \lambda_{c,0} + 0.6$ nm which is the most red-shifted spectral position of the mode, i.e. $\lambda_c(t = 0.25\,T_{SAW})$. After the laser excites the sample the decay of the reference measurement without SAW (red transient) shows a monoexponential slow decay of QDs in the photonic bandgap since the mode is at $\lambda_{c,0}$ and stationary without the SAW. The QDs have a spectral decay time of $\tau = 0.90 \pm 0.03$ ns. When the SAW is generated the mode spectral position is oscillating with a period of $T_{SAW} = 1180$ ps. Initially after the laser excitation, the decay rate is equal to the reference measurement without SAW, i.e. the spontaneous emission is being suppressed. After $\Delta t = 0.5\,T_{SAW}$ the spontaneous emission rate increases drastically exceeding the intensity at excitation time due to the much higher extraction efficiency. For a time interval of ≈ 300 ps, the emission rate is high as a large number of optical states is available since the mode is spectrally overlapping with the emitters. This time interval is in good agreement with the fast decay of the biexponential decay but also depends on the spectral width of the mode and its tuning rate $|d\lambda_c(t)/dt|$. The measurement demonstrates that a spectral oscillation of the optical mode using the proposed SAW tuning mechanism offers a way to clock the fast recombination of a QD, i.e. the efficiency of the emitter as a single photon light source [32] at a defined frequency. By electrically driving the QD single photon emission ([102],[82]) on-wafer fabrication and full integration for quantum encrypted communication applications products are achievable.

After the mode becomes spectrally detuned from the observed QDs, the rate of spontaneous emission decreases and returns to a value comparable to the reference measurement without SAW. The photon count is lower though due to the reduced number of excited QDs after the fast Purcell-enhanced decay. At $\Delta t = T_{SAW}$ and $\Delta t = 2T_{SAW}$ after the first coupling of the mode additional peaks of the photon count are registered. Assuming that all QDs which were spectrally coupled to the mode have emitted into the mode at the first coupling this increase results from a decrease of the optical confinement of the cavity. This accounts for the

small variation of the Q-factor of the mechanically deformed membrane in the FDTD simulations and time-integrated measurements. Additionally, a lower vertical confinement of light in the cavity could increase the collection of photons.

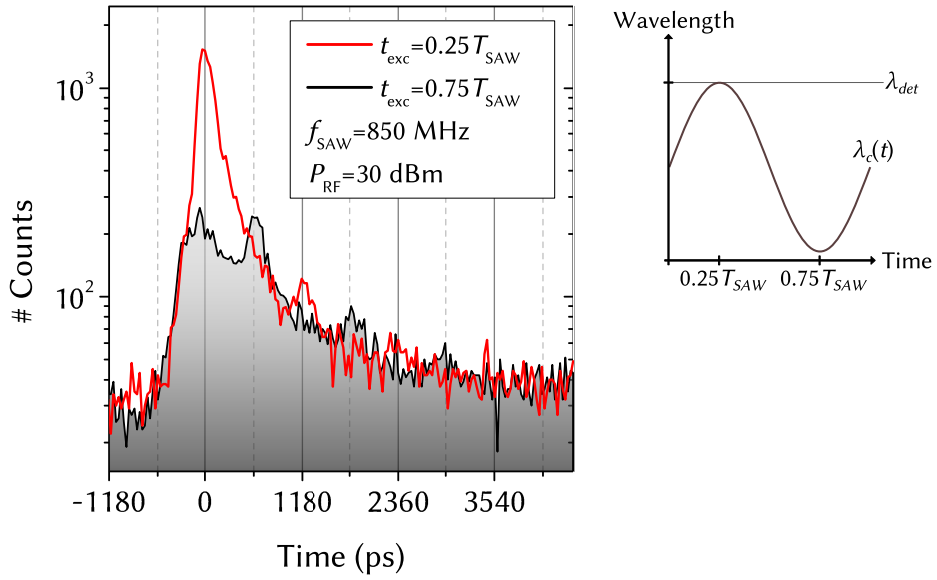

Figure 4.10 – Decay transients recorded at $\lambda_{det} = \lambda_c(t = 0.25\,T_{SAW}) = \lambda_{c,0} + 0.9$ nm, $\lambda_{c,0} = 913.9$ nm, $Q = 3800$. The SAW frequency is $f_{SAW} = 850$ MHz at $P_{RF} = 30$ dBm and $T_{SAW} = 1180$ ps

Detecting the photon emission at $\lambda_{det} = \lambda_c(t = 0.25\,T_{SAW})$ and exciting the QDs at $t_{exc} = t_{couple} = 0.25\,T_{SAW}$ should result in a Purcell-enhanced recombination rate at the time of the laser pulse. This is shown in Fig. 4.10 for a SAW frequency $f_{SAW} = 850$ MHz. The comparison of the decay transients for excitation times $t_{exc} = 0.25\,T_{SAW}$ and $t_{exc} = 0.75\,T_{SAW}$ yields that the state of spectral overlap are spaced by $T_{SAW}/2$ in time. The measurement shows conclusively that the SAW can couple and decouple the cavity mode to and from a QD within the SAW period. It also demonstrates that the time of the resonance condition can be arbitrarily set within the SAW period.

This demonstration is extended in the measurement shown in Fig. 4.11. Here, decay transients are recorded at $\lambda_{det} = \lambda_c(t = 0.25\,T_{SAW})$ while sweeping the excitation time t_{exc} over the SAW period $T_{SAW} = 590$ ps. For $t_{exc} = t_{couple} =$

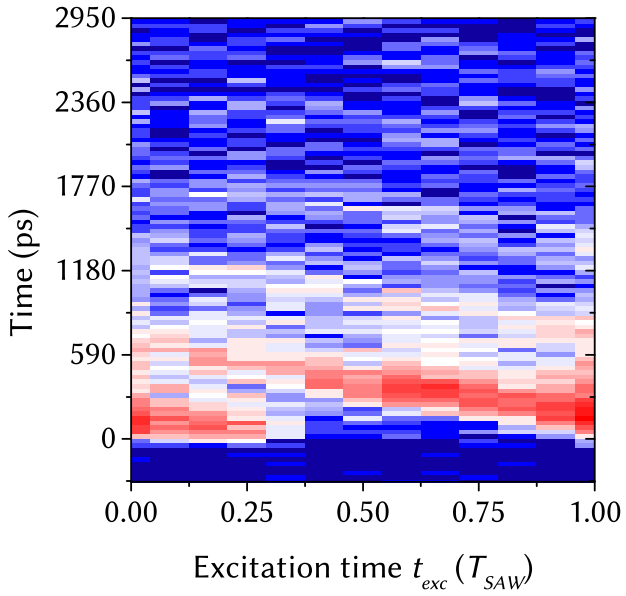

Figure 4.11 – Sweeping the excitation time t_{exc} over the SAW period $T_{SAW} = 590$ ps. Decay transients recorded for $\lambda_{det} = \lambda_c(t = 0.25\,T_{SAW}) = \lambda_{c,0} + 0.6$ nm, $\lambda_{c,0} = 917.0$ nm, $Q = 2300$ for $f_{SAW} = 1704$ MHz and $P_{RF} = 32$ dBm.

$0.25\,T_{SAW}$, a strong luminescence signal resulting from an increased recombination is recorded at $t = 0$ ps and at integer multiples of T_{SAW}. The signal is well resolved for four SAW periods. As t_{exc} is swept over the SAW period the time delay for the mode to overlap with the emitter changes as described in Eq. 4.5. Consequently, when exciting the sample at $t_{exc} = 0.75\,T_{SAW}$ the increased recombination rate is measured $\Delta t = 0.5\,T_{SAW}$ later. Hence, a periodical increase of the recombination rate is observed, the onset of which can be controlled via the excitation time.

As the temporal resolution of the TCSPC measurement of the QD decay improves after the exciting laser pulse this temporal shift of the spectral overlap can be used to improve the temporal resolution of fast recombination events. When the detection wavelength is set to neither $\lambda_c(t = 0.25\,T_{SAW})$ nor $\lambda_c(t = 0.75\,T_{SAW})$, emitters are observed which experience a spectral overlap with the mode twice during the SAW period as depicted for QD2 in Fig. 4.7. Additionally, for $\lambda_{det} < \lambda_c(t = 0.25\,T_{SAW})$ the tuning rate of the mode $|d\lambda_c(t)/dt|$ is higher. Both measurements with $t_{exc} = 0.1\,T_{SAW}$ and $t_{exc} = 0.6\,T_{SAW}$ in Fig. 4.12 exhibit two peaks

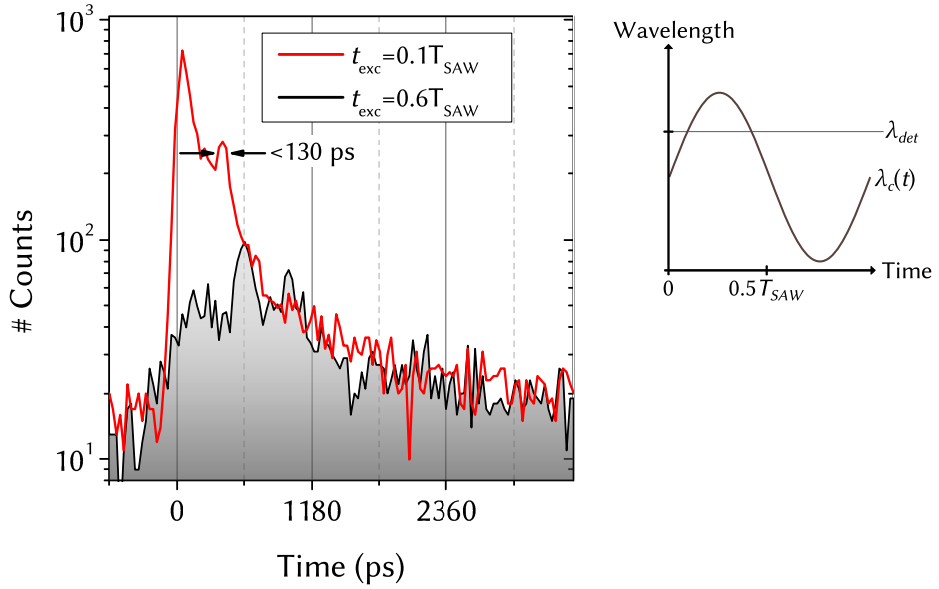

Figure 4.12 – Decay transients recorded at $\lambda_{det} = \lambda_c + 0.3$ nm exhibit two recombination rate maxima during T_{SAW}. $\lambda_c = 922.2$ nm, $Q = 5000$, $f_{SAW} = 850$ MHz, $P_{RF} = 25$ dBm.

of Purcell-enhanced emission rate spaced by $\approx 0.3 \times T_{SAW}$ in the first SAW period ($T_{SAW} = 1180$ ps). In the transient recorded with $t_{exc} = 0.1T_{SAW}$ the first peak is not well resolved. Here, the time resolution is low due to the width of the laser pulse of $\tau_{laser} = 90$ ps. As the mode overlaps with the QD $0.3T_{SAW}$ later a sharp peak with a width of < 130 ps is resolved. For $t_{exc} = 0.6T_{SAW}$ the measurement features two sharp peaks. Both measurements demonstrate an increased temporal resolution by delaying the spectral overlap from the excitation of the system. Additionally, these measurements prove that the SAW tuning mechanism is capable of decoupling and coupling the mode to a QD within a time interval that is shorter than the Purcell-enhanced decay of $\tau_2 \approx 200$ ps. Moreover, manipulation within the inherent timescale is shown.

5 Outlook and conclusion

Integrated optics, i.e. on-chip photonic devices can consist of a network of coupled cavities as demonstrated in [103],[104],[105]. Here, presentation of FDTD simulations of such a coupled system is intended as an outlook to further demonstrate the potential of the SAW control for planar photonic networks. In a simple config-

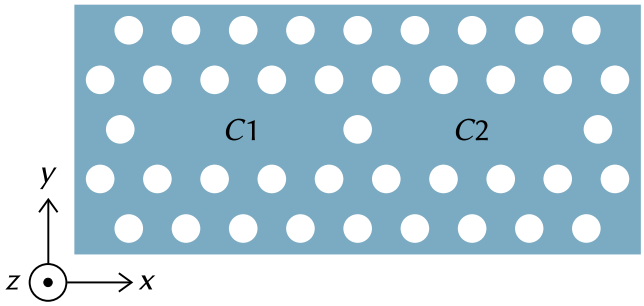

Figure 5.1 – Schematic of two L3 cavity separated by a single airhole barrier.

uration two L3-cavities are separated by a single airhole (see Fig. 5.1). Due to the lateral proximity energy transfer between the cavities is possible. The cavities are coupled in the case of matching resonance frequencies. The energy can be fully transferred between the cavities as shown by the calculated electric field amplitude for cavity $C1$ and cavity $C2$ plotted in Fig. 5.2. The energy transfer is limited by the optical confinement of the cavities which exhibit a Q-factor of $Q = 1100$. The energy is alternately stored in a symmetric (M_S) and antisymmetric (M_A) supermode. Consequently, the simulated spectrum shows two modes with $\lambda_{M_S} = 948.1$ nm and $\lambda_{M_A} = 949.1$ nm. As a result of the cavity coupling the modes are delocalized over the area of both cavities. The lateral distributions of the electric field are shown in Fig. 5.3. The tuning of the cavity resonances are calculated for the photonic crystal being deformed by a surface acoustic wave with $\lambda_{SAW} = 8a$ which is twice the distance between the two cavity centers. At $t = 0\,T_{SAW}$ and $t = 0.5\,T_{SAW}$

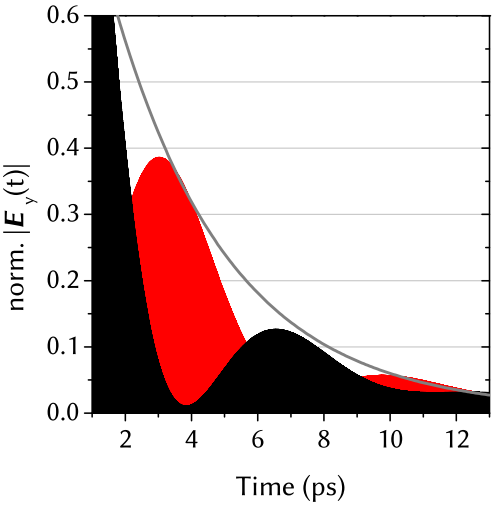

Figure 5.2 – Absolute electric field amplitude $|E_y(t)|$ in cavity $C1$ (black) and cavity $C2$ (red) from FDTD simulations. The energy is exchanged between the coupled cavities limited by the losses of the cavities.

a node of the sinusoidal deformation is exactly between the two cavities. As a result, one cavity is compressed whereas the other is extended and vice versa. This asymmetric deformation results in non-identical cavities and decouples the two cavities. Only at $t = 0.25T_{SAW}$ and $t = 0.75T_{SAW}$ both cavities are equally deformed restoring the cavity coupling. Fig. 5.4 shows that only in these situations two modes are found in the calculated spectrum. At any other time the spectrum only features a single mode. Consequently, the surface acoustic wave can be used to couple, decouple and re-couple two cavities within half of the SAW period.

The previous chapters have demonstrated in time-integrated and time-resolved experiments that the optical mode of photonic crystal nanocavity is tuned spectrally due to the mechanical deformation of the membrane by a coherent beam of electrically generated acoustic phonons. Using this approach, it is possible to reversible manipulate the coupling strength of a QD-cavity system within the period of the surface acoustic wave. The dynamic coupling and decoupling of the cavity mode to the observed QDs has been successfully demonstrated within < 130 ps. Previous tuning approaches have to be considered static compared to the spectral lifetime of the quantum emitters. Moreover, it has been shown that the cavity can be spectrally tuned over the range of 1.5 nm within this time interval. This corresponds to

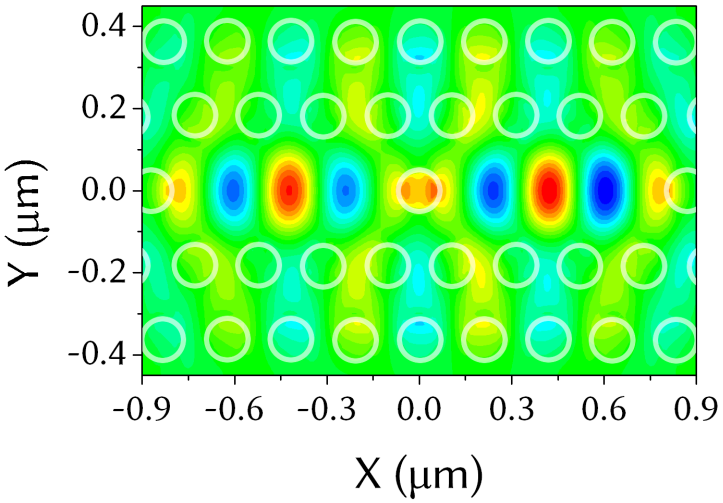

(a)

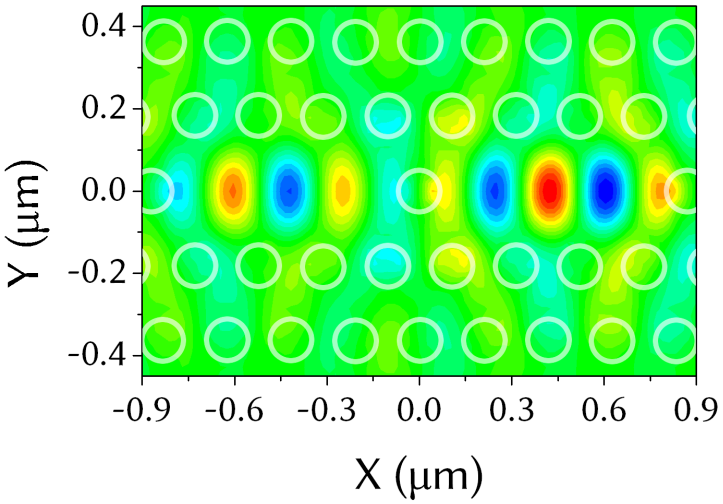

(b)

Figure 5.3 – Calculated spatial mode profiles $\mathbf{E_y}(\mathbf{r})$ of the delocalized supermodes: (a) symmetric mode M_s, and (b) asymmetric mode M_a

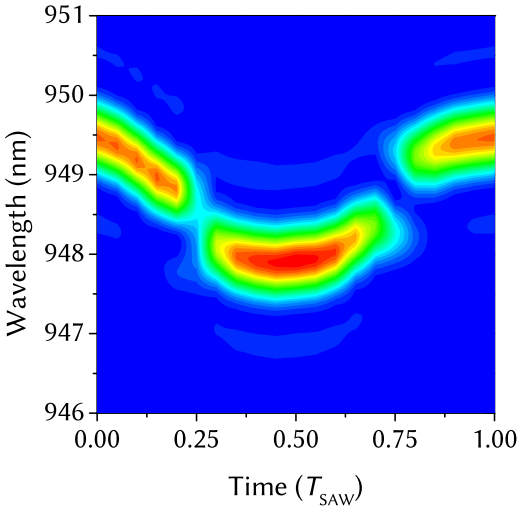

Figure 5.4 – Simulated spectra of the resonances in cavity $C2$ for a photonic crystal membrane deformed by a SAW, $\lambda_{SAW} = 8a$.

more than 13.5 times the spectral linewidth of the unperturbed mode. In addition to the fast tuning rate and effectiveness the SAW tuning mechanism has proven to preserve the quality factor of the mode.

Naturally, subsequent experiments will investigate the coherent control and probing of non-classical states of light created by strongly coupling a single InAs QD to a high-Q L3 cavity. The FDTD domain calculations show that efficient control of the coupling can be exerted at a rate of more than 23 GHz. This SAW frequency exceeds the emitter-photon coupling rate of 18.4 GHz observed in [18]. Clearly, this is faster than the energy transfer between the dressed states $|g;1\rangle$ and $|e;0\rangle$. Such fast manipulation is not an adiabatic change of the coupling strength. It is expected that this fast driving of the system creates entanglement. Another essential experiment is to control the photon blockade in the strong coupling regime. As described in Chap. 1.2, the probability of the coupled QD-cavity system to absorb another photon at the energy $\hbar\omega_c + g_0$ vanishes. Transmission of signals via a network of interconnection optical waveguides and cavities can be controlled by manipulating the coupling strength of QD and cavity by fast spectral detuning of the cavity mode with SAW.

6 Appendix: Experimental setup and sample fabrication

6.1 Experimental setup

The setup used in the experiments described is displayed schematically in Fig. 6.1. The experimental setup can be divided into two functional building blocks. The first block makes up the optical setup consisting of the laser, filters, spectrometer, etc. The second block includes the necessary equipment for the generation of the SAW and its synchronization with the laser pulses. The sample is thermally coupled to an evacuated (10^{-6} mbar) continuous helium flow cryostat (ST-500, Janis Research). The experiments are performed at a sample temperature $T = 7.5$ K in order to assure a high occupation probability of charge carriers in the QDs and to minimize non-radiative decay processes. Charge carriers are non-resonantly excited in the wetting layer (see Chap. 1.4) by a pulsed diode laser (LDH-P-850, PicoQuant) emitting at $\lambda_{Laser} = 855$ nm. The laser pulses have a pulse width of $\tau = 90$ ps. The laser repetition rate is either set internally by the laser controller (PDL-800B, PicoQuant) or by an external trigger with a maximum rate of 80 MHz. The excitation light passes a narrow bandpass filter centered around the laser line. The light intensity is measured via a 50 : 50 beam splitter directing half of the laser light into a power meter. A second beamsplitter with dichroic properties directs the laser light toward the sample while transmitting the collected light from the sample to the spectrometer. A wide aperture objective lens (magnification 50, numerical aperture 0.55) focuses the excitation laser and collects the light emitted by the sample. For coarse alignment of objective lens relative to the sample

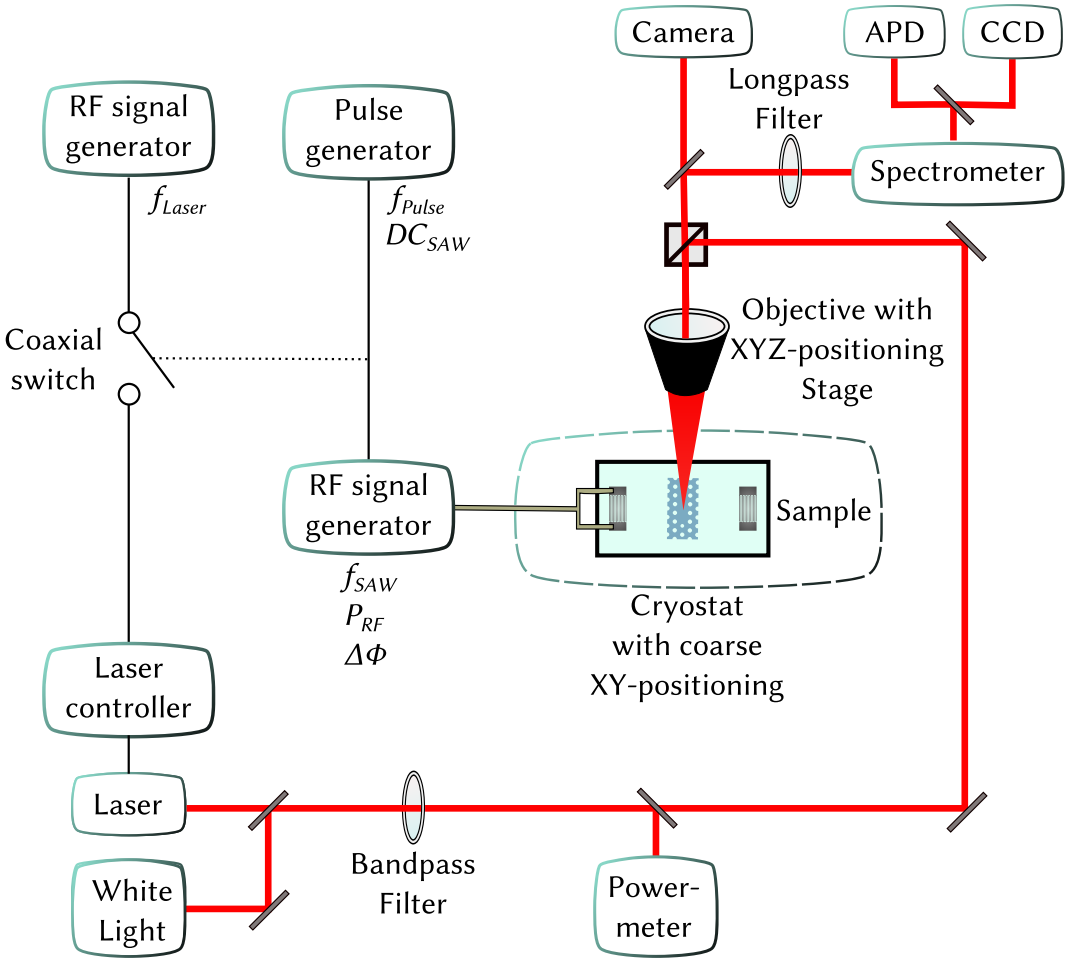

Figure 6.1 – Experimental setup used for μPL-experiments. Important building blocks around the sample inside the cryostat are the RF equipment for generation and timing of the SAW pulses and phase-locked optical excitation as well as the dispersion and evaluation of the light emitted by the sample.

the cryostat is mounted on a micrometer positioning stage. To obtain finer spatial alignment a XYZ-piezostage coupled to the objective lens is used. This alignment is facilitated by a camera and a white light source which can be coupled into the beam path. Before entering the spectrometer most of the laser light is filtered out by a long pass filter (cutoff wavelength 900 nm). After passing the 120 μm entrance slit the monochromator (1200 lines grating) diffracts the light which is directed onto a Si-CCD sensor array cooled with liquid nitrogen (Spec-10:2K, Princeton Instruments) to obtain time-integrated spectral information with a spectral resolution of 70 meV. Time-resolved information is obtained via an avalanche photodiode (APD) which is connected to the spectrometer by an optical fiber. The APD (PDM 50ct, Micro Photon Devices) is able to detect single photons with a timing resolution of < 50 ps with a dead time of 70 ns after each event. For time-correlated single photon counting (TCSPC) the output of the APD is connected to a PicoHarp300 by PicoQuant. The instrument registers the time delay between the exciting laser pulse and the detection event of a photon by the APD. This information is binned and by repeating the excitation/decay process several times a histogram or trace of the decay probability is obtained. The experimental setup, e.g. laser pulse width as well as filter and fiber characteristics, is also contained in the recorded trace. This contribution is measured separately by detecting the laser line with the APD. This so-called *Instrument Response Function* (IRF) and the decay process to be analyzed can be deconvoluted after the measurement.

The second conceptual building block of the experimental setup consists of the RF equipment for SAW generation and triggering of the SAW and the laser pulses. Up to four IDTs on a sample are accessible by coaxial connectors on the cryostat. The SAW frequency f_{SAW} is generated by a RF signal generator (SME03, Rohde& Schwarz) and amplified by a wideband coaxial amplifier (ZHL-4240W, Mini-Circuits) by 38 dBm. Due to limitations of the amplifier the RF power of the signal generator can be set up to -5 dBm resulting in a maximum power of $P_{RF} = 33$ dBm. At such high powers a continuous SAW generation would lead to substantial heat generation on the sample. This would in turn result in sample drift and moreover in a red-shift of the QD emission and the resonance of the PCM nanocavity.

This problem is widely mitigated by pulsing the SAW. The RF signal generator is gated by an external control signal provided by a pulse generator (DG535, Stanford Research Systems). The pulse repetition rate is typically set to a value of $f_{Pulse} = 8$ kHz. For the presented experiments the SAW duty cycle DC_{SAW}, i.e. the ratio of the time the SAW is generated in respect to the pulse period $1/f_{Pulse}$ was less than 1%. The pulse schme of SAW and laser is depicted in Fig. 6.2. The time delay

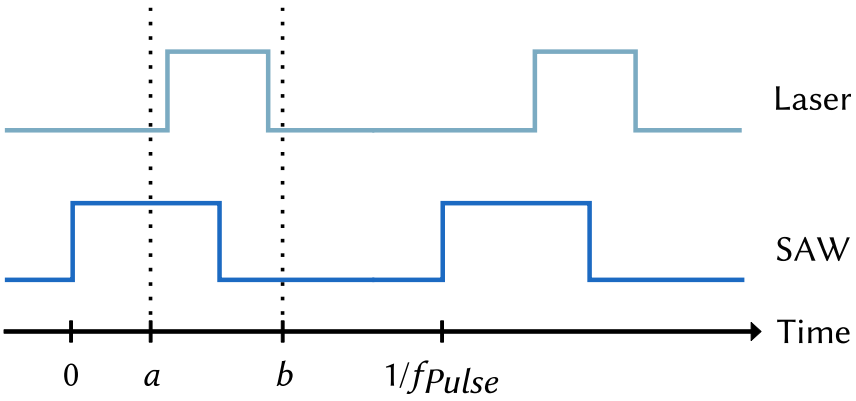

Figure 6.2 – The laser and RF signal generating the SAW are controlled depending on the sample geometry and the PL detection site relative to two opposing IDTs. This is necessary to avoid measurement of the cavity resonance when the PCM is undeformed ($t < a$) or deformed by the SAW interfering with its reflection ($t > b$). This pulse scheme is not to scale.

between the leading edges of the signals controlling the laser and the SAW generation is determined by the time the SAW propagates from the IDT to the PCM. The SAW covers the distance from the IDT to the detection site in $t = a$ (as indicated in Fig. 6.2). Accordingly, the laser pulse delay has to be larger than a in order to avoid measuring the undeformed PCM. Typically the delay was set to $a + 150$ ns. The laser is turned off before the SAW reflected by the IDT on the opposite side of the sample interferes at the detection site at $t = b$.

As described above, the excitation laser was not operating in a CW. The laser was pulsed with either 80 MHz or with f_{Laser} provided by an external source (33250A, Agilent) connected to the laser controller. Here, the DG535 pulse generator controls a coaxial switch gating the input of the triggering signal. For stroboscopic measurement as shown in Fig. 4.5 each 90 ps laser pulse has to be triggered at a fixed time relative to the SAW period. The laser pulse frequency f_{Laser} has to

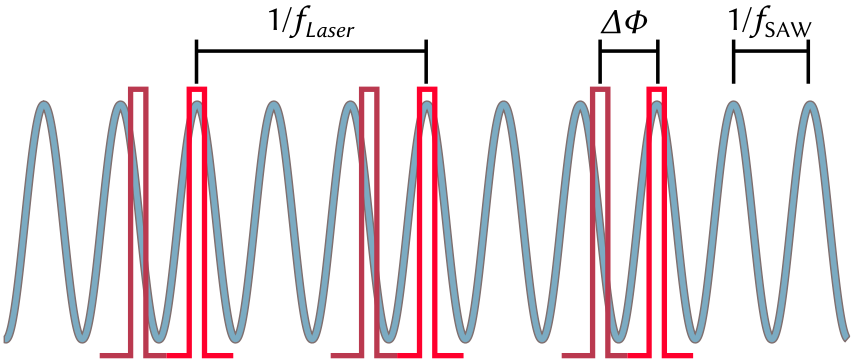

Figure 6.3 – Timing parameters and relations important for stroboscopic SAW-phase-locked measurements: $f_{Laser} = f_{SAW}/n$ ($n = 1, 2, 3...$) and the SAW phase difference $\Delta\Phi$.

be an integer fraction of the SAW frequency to satisfy this condition as shown in Fig. 6.3. Consequently, the sample is excited by each laser pulse at the exact same SAW phase. By scanning the SAW phase Φ_{SAW}, the dynamics of the observed system can be investigated with the benefit of acquiring the full spectral information provided by the CCD.

The detection scheme has been successfully used and developed for probing QDs and Quantum Posts. For an extensive description see [75].

6.2 Sample design

The sample layout is depicted in Fig. 6.4. On the sample the PCMs are arrange in arrays. Each array features 30 PCMs spaced by 50 μm. A PCM array is centered between a pair of IDTs with at a distance of 1650 μm. Each IDT consists of 80 finger-pairs with an aperture of 200 μm. The finger periods used for presented measurements are 7.28, 3.64 and 1.82 μm. The cross-shaped alignment markers were processed together with the PCMs. The markers serve to align the IDTs to the PCM arrays.

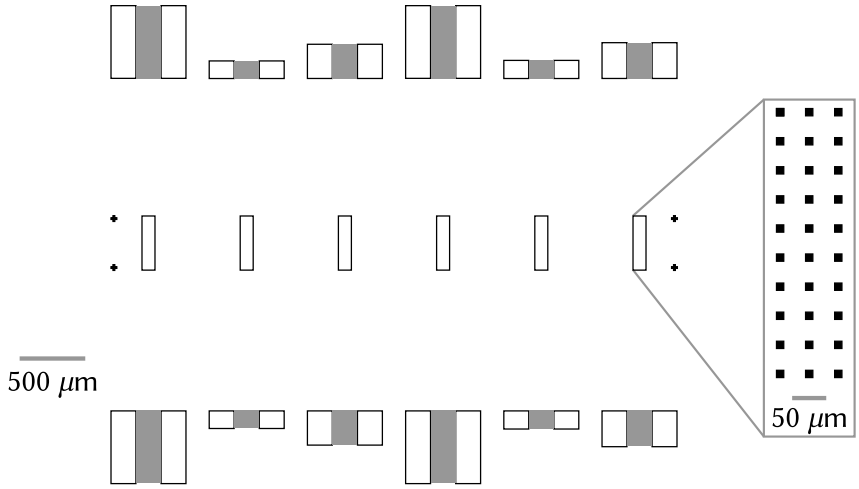

Figure 6.4 – Sample layout with six arrays of PCMs, IDTs and alignment markers: PCM array period 800 μm, PCM period 50 μm, shortest distance IDT-PCM 1650 μm.

6.3 Sample fabrication

Each sample was processed at two facilities. In a first step, the PCMs were fabricated in the clean room facilities (the "Nanotech") of UC Santa Barbara. The IDTs were processed in a second step at the University of Augsburg.

6.3.1 PCM processing

For fabrication of the PCMs operating in the spectral range of the InAs QD emission a resolution of a few nm is necessary. Consequently, patterning is not feasible using UV light and is achieved by electron beam lithography. The PCM pattern is transferred to the wafer material using reactive ion etching. In order create the free-standing membranes essential for good light confinement and thus high Q-factors an undercut is performed by etching a sacrificial layer of AlGaAs with hydrofluoric acid (HF). In Fig. 6.5 these steps are depicted.

The sample wafer material was grown by molecular beam epitaxy (MBE) in the MBE-Lab of Pierre Petroff (UCSB Materials Department) by either Hyochul Kim or Tuan Anh Truong. On top of a bulk GaAs wafer, a layer stack was built consisting of 150 nm of GaAs, 920 nm of $Al_{0.7}Ga_{0.3}As$ and 134 nm of GaAs with embedded InAs QDs. During the growth of the QD layer the wafer rotation was stopped to

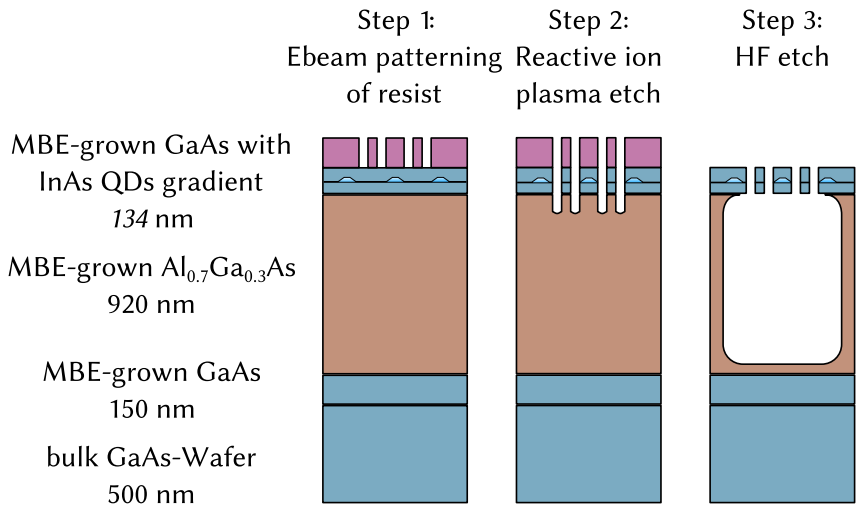

Figure 6.5 – Fabrication of PCMs in a three step process: Electron beam lithography, reactive ion etching and HF etching of the AlGaAs sacrificial layer.

achieve a gradient of the QD density.

After verification of the optical properties of QDs and QD density by μPL an approx. 15 × 15 mm sized piece was cleaved from the wafer (the maximum write area is limited by the sample holder of the electron beam lithography equipment to 12 mm).

For electron beam (EB) lithography the sample was coated with a high resolution positive electron beam resist (ZEP-520A) by the following these steps:

- Cleansing of the wafer piece under running deionized water for 30 s.
- Mounting on resist spinner and blowing dry with N_2 while spinning at 3000 *rpm*.
- Covering the wafer with resist while not spinning.
- Spin coating the wafer for 40 s at 3000 rpm, ramp up 1000 rpm/s, ramp down 1500 rpm/s
- Baking the resist on a hotplate at 170 °C for 120 s.

This results in a uniform coating with resist of approx. 400 nm thickness. The final sample layout consisting of 6 PCM arrays and alignment markers (see Fig. 6.4) were then transferred four times to the resist by EB lithography using a JEOL JBX-6300FS Electron Beam Lithography System. With an acceleration voltage of 100 kV a minimum spot size of 2 nm can be achieved. The write was performed

using a 25 μm aperture and 100 pA write current. Subsequently, the resist was developed by:

- Newly mixed solution of 1 : 1 methyl isobutyl ketone (MIBK) and isopropanol for 65 s.
- Rinsing the sample in a newly mixed solution 9 : 1 MIBK and isopropanol for 15 s.
- Blowing dry with N_2.

The PCM pattern is transferred to the wafer by an inductively coupled plasma-reactive ion etch (ICP-RIE E640, Panasonic) using a reactive plasma created in an atmosphere of BCl_3, Cl_2 and Ar. This process provides excellent isotropic etching properties involving:

- Chamber cleaning: 50 ccm CF_4, 40 ccm O_2 at 800 W ICP source power for 10 min.
- Chamber preparation: 30 ccm BCl_3, 50 ccm Cl_2, 60 ccm Ar at 900 W ICP source power and 200 W RF sample bias source power for 3 min.
- Loading of the sample mounted onto a 6" wafer using a thin film of vacuum oil.
- Etching process: 3 ccm BCl_3, 5.6 ccm Cl_2, 12 ccm Ar at 600 W ICP source power and 72W RF sample bias source power for 125 s.

During the ICP etch "Shipley Microposit Remover 1165" is heated to 80 °C in an aluminum bowl. The amount of oil under the sample is reduced by carefully moving the sample on the supporting wafer before the sample is placed for 10 min in the resist stripper. Subsequently, the sample is rinsed with isopropanol and blown dry with N_2. The last remains of the resist are removed by an O_2-plasma etch at 300 mT, 100 W for 10 s (PE-IIA, Technics).
For the undercut of the PCM layer the sacrificial layer is etched with HF wearing a full face shield, acid resistant gloves and apron. The sample etched in a solution of 5 : 1 deionized water and HF (49%) for 30 s while moving the sample in the etchant using inert tweezers. The etched process is stopped by holding the sample under running deionized water for 30 s.

6.3.2 IDT processing

The samples were further processed at the clean room facilities of the "Lehrstuhl für Experimental Physik I" at the University of Augsburg. The preparation steps include EB lithography of the IDTs and metalization with aluminum as well as bonding the IDTs to the RF connectors of the sample carrier.
The wafer with the PCMs is cleaved into four pieces with six PCM arrays each (see Fig. 6.4). In order to remove any oxide grown on the PCM layer the sample is dipped in deionized water and then in a 1 : 3 HCL acid : H_2O solution for 20 s. The sample is rinsed with water and blown dry with N_2. Subsequently the sample is coated with two layers of EB resist by the following steps:

- On a hotplate heating the sample in a glass dish to 150 °C for 5 min to evaporate any residual water.
- Cover the glass dish and to let the sample cool down to room temperature.
- Mount the sample onto the spin coater and blow with N_2 while spinning.
- The sample is coated with 2 drops of EB positive resist PMMA 150K 4% while spinning at 500 rpm. The spin coater is than accelerated to 5000 rpm for 30s adding 3 more drops of resist in the first seconds.
- Bake the covered sample in a glass dish on a hotplate for 90 s at 190 °C and let it cool down to room temperature.
- Coat the sample with EB positive resist PMMA 500K 2% in the same fashion.
- Again bake the covered sample in a glass dish on a hotplate for 90 s at 190 °C.

The two layers of EB resist are necessary to facilitate a clean lift-off of the superfluous metal after metalization.
The IDT patterns are then written into the EB resist using a Raith eLine 100 Electron Beam Lithography System. The IDT pads requiring less resolution are written with a 60 μm aperture while the IDT fingers are written with a 30 μm aperture. The acceleration voltage is 10 kV. Additional parameters are:

- Area step size 0.02 μm (30 μm aperture), 0.0936 μm (60 μm aperture), using write field size 500.

- Area dose 100 μAs/cm^2
- The IDTs with a period of 1.82 μm are written in ”Line mode” with a line step size of 0.005 μm and line dose of 280 pAs/μm using write field size 200.

The exposed sample is developed in a solution of 3 : 1 MIBK and isopropanol for 30 s. The sample is then rinsed with isopropanol. Subsequently the sample is cleaned in an O_2-plasma etch at 500 mT and 200 W for 12 s to remove remaining exposed resist. Another HCl etch for 5 s is intended to remove new oxide. The sample is then metalized with 5 nm of Ti and 50 nm of Al via electron beam physical vapor deposition at a current of 70 and 40 nA respectively.
For the lift-off process, the sample is submerged in acetone for approx. 12 h. Due to the sensitivity of the PCMs the use of an ultra-sonic bath is not possible. Most of the metal is removed by agitating the acetone on the sample with a pipette. Remaining metal shortening the IDT fingers was carefully removed with a single hair of a fine brush attached to a pair of tweezers using an optical microscope.

Bibliography

[1] Eli Yablonovitch. Inhibited Spontaneous Emission in Solid-State Physics and Electronics. *Physical Review Letters*, 58(20):2059–2062, May 1987.

[2] J L O'Brien, A Furusawa, and Jelena Vuckovic. Photonic quantum technologies. *Nature Photonics*, 3(December):687–695, 2009.

[3] Jon Cartwright. Intel enters the third dimension. *Nature*, May 2011.

[4] T D Ladd, F Jelezko, R Laflamme, Y Nakamura, C Monroe, and J L O'Brien. Quantum computers. *Nature*, 464(7285):45–53, March 2010.

[5] D. Deutsch. Quantum Theory, the Church-Turing Principle and the Universal Quantum Computer. *Proceedings of the Royal Society A: Mathematical, Physical and Engineering Sciences*, 400(1818):97–117, July 1985.

[6] D. Deutsch and R. Jozsa. Rapid Solution of Problems by Quantum Computation. *Proceedings of the Royal Society A: Mathematical, Physical and Engineering Sciences*, 439(1907):553–558, December 1992.

[7] Lov Grover. Quantum Mechanics Helps in Searching for a Needle in a Haystack. *Physical Review Letters*, 79(2):325–328, July 1997.

[8] Daniel Loss and David P. DiVincenzo. Quantum computation with quantum dots. *Physical Review A*, 57(1):120–126, January 1998.

[9] N. A. Gershenfeld. Bulk Spin-Resonance Quantum Computation. *Science*, 275(5298):350–356, January 1997.

[10] H Häffner, W Hänsel, C F Roos, J Benhelm, D Chek-al Kar, M Chwalla, T Körber, U D Rapol, M Riebe, P O Schmidt, C Becher, O Gühne, W Dür,

and R Blatt. Scalable multiparticle entanglement of trapped ions. *Nature*, 438(7068):643–6, December 2005.

[11] L DiCarlo, J M Chow, J M Gambetta, Lev S Bishop, B R Johnson, D I Schuster, J Majer, A Blais, L Frunzio, S M Girvin, and R J Schoelkopf. Demonstration of two-qubit algorithms with a superconducting quantum processor. *Nature*, 460(7252):240–4, July 2009.

[12] B. Lanyon, T. Weinhold, N. Langford, M. Barbieri, D. James, A. Gilchrist, and A. White. Experimental Demonstration of a Compiled Version of Shor's Algorithm with Quantum Entanglement. *Physical Review Letters*, 99(25):250505, December 2007.

[13] A. Imamoglu, D. D. Awschalom, G. Burkard, D. P. DiVincenzo, D. Loss, M. Sherwin, and A. Small. Quantum Information Processing Using Quantum Dot Spins and Cavity QED. *Physical Review Letters*, 83(20):4204–4207, November 1999.

[14] Andrei Faraon, Ilya Fushman, Dirk Englund, Nick Stoltz, and Jelena Vuˇ. Dipole induced transparency in waveguide coupled photonic crystal cavities. *Optics Express*, 16(16):944–947, 2008.

[15] Jonathan C. F. Matthews, Alberto Politi, André Stefanov, and Jeremy L. O'Brien. Manipulation of multiphoton entanglement in waveguide quantum circuits. *Nature Photonics*, 3(6):346–350, May 2009.

[16] Dirk Englund, Andrei Faraon, Ilya Fushman, Nick Stoltz, Pierre Petroff, and Jelena Vucković. Controlling cavity reflectivity with a single quantum dot. *Nature*, 450(7171):857–61, December 2007.

[17] M. Nomura, N. Kumagai, S. Iwamoto, Y. Ota, and Y. Arakawa. Laser oscillation in a strongly coupled single-quantum-dot–nanocavity system. *Nature Physics*, 6(4):279–283, February 2010.

[18] K Hennessy, a Badolato, M Winger, D Gerace, M Atatüre, S Gulde, S Fält, E L Hu, and a Imamoğlu. Quantum nature of a strongly coupled single quantum dot-cavity system. *Nature*, 445(7130):896–9, February 2007.

[19] Andrei Faraon, Arka Majumdar, Hyochul Kim, Pierre Petroff, and Jelena Vučković. Fast Electrical Control of a Quantum Dot Strongly Coupled to a Photonic-Crystal Cavity. *Physical Review Letters*, 104(4):1–4, January 2010.

[20] A. Kress, F. Hofbauer, N. Reinelt, M. Kaniber, H. Krenner, R. Meyer, G. Böhm, and J. Finley. Manipulation of the spontaneous emission dynamics of quantum dots in two-dimensional photonic crystals. *Physical Review B*, 71(24):1–4, June 2005.

[21] Igor V Kukushkin, Jurgen H Smet, Vito W Scarola, Vladimir Umansky, and Klaus von Klitzing. Dispersion of the excitations of fractional quantum Hall States. *Science (New York, N.Y.)*, 324(5930):1044–7, May 2009.

[22] Matt Eichenfield, Jasper Chan, Amir H Safavi-naeini, Kerry J, and Oskar Painter. Modeling dispersive coupling and losses of localized optical and mechanical modes in optomechanical crystals. *Optics Express*, 17(22):1819–1824, 2009.

[23] Saeed Mohammadi, Ali Asghar Eftekhar, William D. Hunt, and Ali Adibi. High-Q micromechanical resonators in a two-dimensional phononic crystal slab. *Applied Physics Letters*, 94(5):051906, 2009.

[24] E. Gavartin, R. Braive, I. Sagnes, O. Arcizet, a. Beveratos, T. Kippenberg, and I. Robert-Philip. Optomechanical Coupling in a Two-Dimensional Photonic Crystal Defect Cavity. *Physical Review Letters*, 106(20):1–4, May 2011.

[25] RJ Thompson. Observation of normal-mode splitting for an atom in an optical cavity. *Physical Review*, 68(8):1132–1135, 1992.

[26] Kerry J Vahala. Optical microcavities. *Nature*, 424(6950):839–46, August 2003.

[27] ET Jaynes and FW Cummings. Comparison of quantum and semiclassical radiation theories with application to the beam maser. *Proceedings of the IEEE*, 1963.

[28] Mark Fox. *Quantum Optics*. Oxford University Press, 2006.

[29] Kerry Vahala. *Optical Microcavities*. World Scientific, 2004.

[30] EM Purcell, HC Torrey, and RV Pound. Resonance absorption by nuclear magnetic moments in a solid. *Physical review*, 69:37–38, 1946.

[31] E. Yablonovitch. Photonic band-gap structures. *Journal of the Optical Society of America B*, 10(2):283, February 1993.

[32] Dirk Englund, David Fattal, Edo Waks, Glenn Solomon, Bingyang Zhang, Toshihiro Nakaoka, Yasuhiko Arakawa, Yoshihisa Yamamoto, and Jelena Vučković. Controlling the Spontaneous Emission Rate of Single Quantum Dots in a Two-Dimensional Photonic Crystal. *Physical Review Letters*, 95(1):2–5, July 2005.

[33] Bryan Ellis, MA Mayer, Gary Shambat, and Tomas Sarmiento. Ultralow-threshold electrically pumped quantum-dot photonic-crystal nanocavity laser. *Nature*, 5(April):297–300, 2011.

[34] T Yoshie, A Scherer, and J Hendrickson. Vacuum Rabi splitting with a single quantum dot in a photonic crystal nanocavity. *Nature*, 432(November):9–12, 2004.

[35] G A Brooker. *Modern Classical Optics*. Oxford University Press, 2003.

[36] DK Armani, TJ Kippenberg, SM Spillane, and KJ Vahala. Ultra-high-Q toroid microcavity on a chip. *Nature*, 421(February):925–928, 2003.

[37] C. Weisbuch, M. Nishioka, A Ishikawa, and Y Arakawa. Observation of the coupled exciton-photon mode splitting in a semiconductor quantum microcavity. *Physical review letters*, 69(23):3314–3317, 1992.

[38] Sajeev John. Strong localization of photons in certain disordered dielectric superlattices. *Physical review letters*, 58(23), 1987.

[39] P Vukusic, J R Sambles, and C R Lawrence. Colour mixing in wing scales of a butterfly. *Nature*, 404(6777):457, March 2000.

[40] Hyoki Kim, Jianping Ge, Junhoi Kim, Sung-eun Choi, Hosuk Lee, Howon Lee, Wook Park, Yadong Yin, and Sunghoon Kwon. Structural colour printing using a magnetically tunable and lithographically fixable photonic crystal. *Nature Photonics*, 3(9):534–540, August 2009.

[41] John D. Joannopoulos, Steven G. Johnson, Joshua N. Winn, and Robert D. Meade. *Photonic Crystals: Molding the Flow of Light (Second Edition)*. Princeton University Press, 2008.

[42] Peter Lodahl, a Floris Van Driel, Ivan S Nikolaev, Arie Irman, Karin Overgaag, Daniël Vanmaekelbergh, and Willem L Vos. Controlling the dynamics of spontaneous emission from quantum dots by photonic crystals. *Nature*, 430(7000):654–7, August 2004.

[43] Susumu Noda, Masayuki Fujita, and Takashi Asano. Spontaneous-emission control by photonic crystals and nanocavities. *Nature Photonics*, 1(8):449–458, August 2007.

[44] Erik C Nelson, Neville L Dias, Kevin P Bassett, Simon N Dunham, Varun Verma, Masao Miyake, Pierre Wiltzius, John a Rogers, James J Coleman, Xiuling Li, and Paul V Braun. Epitaxial growth of three-dimensionally architectured optoelectronic devices. *Nature materials*, 10(9):676–681, July 2011.

[45] Hubert J Krenner, Stefan Stufler, Matthias Sabathil, Emily C Clark, Patrick Ester, Max Bichler, Gerhard Abstreiter, Jonathan J Finley, and Artur Zrenner. Recent advances in exciton-based quantum information processing in quantum dot nanostructures. *New Journal of Physics*, 7:184–184, August 2005.

[46] D. Leonard, M. Krishnamurthy, C. M. Reaves, S. P. Denbaars, and P. M. Petroff. Direct formation of quantum-sized dots from uniform coherent islands of InGaAs on GaAs surfaces. *Applied Physics Letters*, 63(23):3203, December 1993.

[47] M Fricke, A Lorke, J. P Kotthaus, G Medeiros-Ribeiro, and P. M Petroff. Shell structure and electron-electron interaction in self-assembled InAs quantum dots. *Europhysics Letters (EPL)*, 36(3):197–202, October 1996.

[48] H. Drexler, D. Leonard, W. Hansen, J. Kotthaus, and P. Petroff. Spectroscopy of Quantum Levels in Charge-Tunable InGaAs Quantum Dots. *Physical Review Letters*, 73(16):2252–2255, October 1994.

[49] S. Trumm, M. Wesseli, H. J. Krenner, D. Schuh, M. Bichler, J. J. Finley, and M. Betz. Spin-preserving ultrafast carrier capture and relaxation in InGaAs quantum dots. *Applied Physics Letters*, 87(15):153113, October 2005.

[50] Xiaoqin Li, Yanwen Wu, Duncan Steel, D Gammon, T H Stievater, D S Katzer, D Park, C Piermarocchi, and L J Sham. An all-optical quantum gate in a semiconductor quantum dot. *Science (New York, N.Y.)*, 301(5634):809–11, August 2003.

[51] H. Krenner, M. Sabathil, E. Clark, a. Kress, D. Schuh, M. Bichler, G. Abstreiter, and J. Finley. Direct Observation of Controlled Coupling in an Individual Quantum Dot Molecule. *Physical Review Letters*, 94(5):057402, February 2005.

[52] T. Stace, G. Milburn, and C. Barnes. Entangled two-photon source using biexciton emission of an asymmetric quantum dot in a cavity. *Physical Review B*, 67(8):1–15, 2003.

[53] Yasutomo Ota, Masayuki Shirane, Masahiro Nomura, Naoto Kumagai, Satomi Ishida, Satoshi Iwamoto, Shinichi Yorozu, and Yasuhiko Arakawa. Vacuum Rabi splitting with a single quantum dot embedded in a H1 photonic crystal nanocavity. *Applied Physics Letters*, 94(3):033102, 2009.

[54] Yoshihiro Akahane, Takashi Asano, Bong-Shik Song, and Susumu Noda. High-Q photonic nanocavity in a two-dimensional photonic crystal. *Nature*, 425(6961):944–947, October 2003.

[55] Susanna M. Thon, Matthew T. Rakher, Hyochul Kim, Jan Gudat, William T. M. Irvine, Pierre M. Petroff, and Dirk Bouwmeester. Strong coupling through optical positioning of a quantum dot in a photonic crystal cavity. *Applied Physics Letters*, 94(11):111115, 2009.

[56] Andrei Faraon, Ilya Fushman, Dirk Englund, Nick Stoltz, Pierre Petroff, and Jelena Vučković. Coherent generation of non-classical light on a chip via photon-induced tunnelling and blockade. *Nature Physics*, 4(11):859–863, September 2008.

[57] Bong-Shik Song, Susumu Noda, Takashi Asano, and Yoshihiro Akahane. Ultra-high-Q photonic double-heterostructure nanocavity. *Nature Materials*, 4(3):207–210, February 2005.

[58] Eiichi Kuramochi, Masaya Notomi, Satoshi Mitsugi, Akihiko Shinya, Takasumi Tanabe, and Toshifumi Watanabe. Ultrahigh-Q photonic crystal nanocavities realized by the local width modulation of a line defect. *Applied Physics Letters*, 88(4):041112, 2006.

[59] F. S. F. Brossard, X. L. Xu, D. a. Williams, M. Hadjipanayi, M. Hugues, M. Hopkinson, X. Wang, and R. a. Taylor. Strongly coupled single quantum dot in a photonic crystal waveguide cavity. *Applied Physics Letters*, 97(11):111101, 2010.

[60] K Hennessy, A Badolato, A Tamboli, P M Petroff, E Hu, M Atature, J Dreiser, and A Imamoglu. Tuning photonic crystal nanocavity modes by wet chemical digital etching. *Applied Physics Letters*, 87(2):21108, 2005.

[61] Lord Rayleigh. On Waves Propagated along the Plane Surface of an Elastic Solid. *Proceedings of the London Mathematical Society*, s1-17(1):4–11, 1885.

[62] R.M. White. Surface elastic waves. *Proceedings of the IEEE*, 58(8):1238–1276, 1970.

[63] David P. Morgan. *Surface Acoustic Wave Filters: With Applications to Electronic Communications and Signal Processing*. Academic Press, 2007.

[64] S Datta. *Surface Acoustic Wave Devices*. Prentice Hall, 1986.

[65] Ken-Ya Hashimoto. *Surface Acoustic Wave Devices in Telecommunications: Modelling and Simulation*. Springer, 2000.

[66] Eric A. Ash and Edward G. S. Paige. *Rayleigh-Wave Theory and Application*. Springer, 1985.

[67] Steven Simon. Coupling of surface acoustic waves to a two-dimensional electron gas. *Physical Review B*, 54(19):13878–13884, November 1996.

[68] W. Jones J. Campbell. Propagation of Piezoelectric Surface Waves on Cubic and Hexagonal Crystals.

[69] R. M. White and F. W. Voltmer. DIRECT PIEZOELECTRIC COUPLING TO SURFACE ELASTIC WAVES. *Applied Physics Letters*, 7(12):314, December 1965.

[70] A. Wixforth, J. Kotthaus, and G. Weimann. Quantum Oscillations in the Surface-Acoustic-Wave Attenuation Caused by a Two-Dimensional Electron System. *Physical Review Letters*, 56(19):2104–2106, May 1986.

[71] James A H Stotz, Rudolf Hey, Paulo V Santos, and Klaus H Ploog. Coherent spin transport through dynamic quantum dots. *Nature materials*, 4(8):585–8, August 2005.

[72] A. Wixforth, J. Scriba, M. Wassermeier, J. Kotthaus, G. Weimann, and W. Schlapp. Surface acoustic waves on GaAs/AlxGa1-xAs heterostructures. *Physical Review B*, 40(11):7874–7887, 1989.

[73] D. A. Fuhrmann, H. J. Krenner, A. Wixforth, A. Curran, K. A. Prior, R. J. Warburton, and J. Ebbecke. Noninvasive probing of persistent conductivity

in high quality ZnCdSe/ZnSe quantum wells using surface acoustic waves. *Journal of Applied Physics*, 107(9):093717, May 2010.

[74] Stefan Völk, Florian J R Schülein, Florian Knall, Dirk Reuter, Andreas D Wieck, Tuan A Truong, Hyochul Kim, Pierre M Petroff, Achim Wixforth, and Hubert J Krenner. Enhanced sequential carrier capture into individual quantum dots and quantum posts controlled by surface acoustic waves. *Nano letters*, 10(9):3399–407, September 2010.

[75] S. Völk, F. Knall, F. J. R. Schülein, T. a. Truong, H. Kim, P. M. Petroff, a. Wixforth, and H. J. Krenner. Direct observation of dynamic surface acoustic wave controlled carrier injection into single quantum posts using phase-resolved optical spectroscopy. *Applied Physics Letters*, 98(2):023109, 2011.

[76] Florian J. R. Schülein, Kai Müller, Max Bichler, Gregor Koblmüller, Jonathan J. Finley, Achim Wixforth, and Hubert J. Krenner. Acoustically regulated carrier injection into a single optically active quantum dot. *Physical Review B*, 88(8):085307, August 2013.

[77] K. D. Jöns, R. Hafenbrak, R. Singh, F. Ding, J. D. Plumhof, a. Rastelli, O. G. Schmidt, G. Bester, and P. Michler. Dependence of the Redshifted and Blueshifted Photoluminescence Spectra of Single In_{x}Ga_{1-x}As/GaAs Quantum Dots on the Applied Uniaxial Stress. *Physical Review Letters*, 107(21):217402, November 2011.

[78] Paulo V. Santos. Collinear light modulation by surface acoustic waves in laterally structured semiconductors. *Journal of Applied Physics*, 89(9):5060, May 2001.

[79] Mauricio M de Lima Jr and Paulo V Santos. Modulation of photonic structures by surface acoustic waves. *Reports on Progress in Physics*, 68(7):1639–1701, 2005.

[80] M. de Lima, R. Hey, P. Santos, and a. Cantarero. Phonon-Induced Optical Superlattice. *Physical Review Letters*, 94(12):1–4, April 2005.

[81] T. Berstermann, C. Brüggemann, M. Bombeck, a. V. Akimov, D. R. Yakovlev, C. Kruse, D. Hommel, and M. Bayer. Optical bandpass switching by modulating a microcavity using ultrafast acoustics. *Physical Review B*, 81(8):1–5, February 2010.

[82] Hong-Gyu Park, Se-Heon Kim, Soon-Hong Kwon, Young-Gu Ju, Jin-Kyu Yang, Jong-Hwa Baek, Sung-Bock Kim, and Yong-Hee Lee. Electrically driven single-cell photonic crystal laser. *Science (New York, N.Y.)*, 305(5689):1444–7, 2004.

[83] Andrei Faraon, Ilya Fushman, Dirk Englund, Nick Stoltz, Pierre Petroff, and Jelena Vuckovic. Coherent generation of non-classical light on a chip via photon-induced tunnelling and blockade. *Nature Physics*, 4(11):859–863, September 2008.

[84] Daniel A Fuhrmann, Susanna M Thon, Hyochul Kim, Dirk Bouwmeester, Pierre M Petroff, Achim Wixforth, and Hubert J Krenner. Dynamic modulation of photonic crystal nanocavities using gigahertz acoustic phonons. *October*, 5(September):605–609, 2011.

[85] C. P. Michael, K. Srinivasan, T. J. Johnson, O. Painter, K. H. Lee, K. Hennessy, H. Kim, and E. Hu. Wavelength- and material-dependent absorption in GaAs and AlGaAs microcavities. *Applied Physics Letters*, 90(5):051108, 2007.

[86] U K Khankhoje, S-H Kim, B C Richards, J Hendrickson, J Sweet, J D Olitzky, G Khitrova, H M Gibbs, and A Scherer. Modelling and fabrication of GaAs photonic-crystal cavities for cavity quantum electrodynamics. *Nanotechnology*, 21(6):065202, February 2010.

[87] Kane Yee. Numerical solution of initial boundary value problems involving maxwell's equations in isotropic media. *IEEE Transactions on Antennas and Propagation*, 14(3):302–307, May 1966.

[88] A. Taflove and M.E. Brodwin. Numerical Solution of Steady-State Electromagnetic Scattering Problems Using the Time-Dependent Maxwell's Equa-

tions. *IEEE Transactions on Microwave Theory and Techniques*, 23(8):623–630, August 1975.

[89] Allen Taflove. Application of the Finite-Difference Time-Domain Method to Sinusoidal Steady-State Electromagnetic-Penetration Problems. *IEEE Transactions on Electromagnetic Compatibility*, EMC-22(3):191–202, August 1980.

[90] Allen Taflove and Susan C. Hagness. *Computational Electrodynamics: The Finite-Difference Time-Domain Method, Third Edition.* Artech House, 2005.

[91] Lumerical. FDTD Solutions.

[92] C. F. Wang, A. Badolato, I. Wilson-Rae, P. M. Petroff, E. Hu, J. Urayama, and A. Imamoğlu. Optical properties of single InAs quantum dots in close proximity to surfaces. *Applied Physics Letters*, 85(16):3423, October 2004.

[93] A. R. A. Chalcraft, S. Lam, D. O'Brien, T. F. Krauss, M. Sahin, D. Szymanski, D. Sanvitto, R. Oulton, M. S. Skolnick, a. M. Fox, D. M. Whittaker, H.-Y. Liu, and M. Hopkinson. Mode structure of the L3 photonic crystal cavity. *Applied Physics Letters*, 90(24):241117, 2007.

[94] Dirk Englund, Ilya Fushman, and Jelena Vučković. General recipe for designing photonic crystal cavities. *Optics Express*, 13(16):5961, August 2005.

[95] Mitsuru Toishi, Dirk Englund, Andrei Faraon, and Jelena Vucković. High-brightness single photon source from a quantum dot in a directional-emission nanocavity. *Optics express*, 17(17):14618–26, August 2009.

[96] Masahiro Nomura, Satoshi Iwamoto, Toshihiro Nakaoka, Satomi Ishida, and Yasuhiko Arakawa. Cavity Resonant Excitation of InGaAs Quantum Dots in Photonic Crystal Nanocavities. *Japanese Journal of Applied Physics*, 45(8A):6091–6095, August 2006.

[97] M Kaniber, A Neumann, A Laucht, M F Huck, M Bichler, M-C Amann, and J J Finley. Efficient and selective cavity-resonant excitation for single photon generation. *New Journal of Physics*, 11(1):13031, 2009.

[98] Matthew Pelton, Charles Santori, Jelena Vučković, Bingyang Zhang, Glenn Solomon, Jocelyn Plant, and Yoshihisa Yamamoto. Efficient Source of Single Photons: A Single Quantum Dot in a Micropost Microcavity. *Physical Review Letters*, 89(23):1–4, November 2002.

[99] Dirk Englund, Arka Majumdar, Andrei Faraon, Mitsuru Toishi, Nick Stoltz, Pierre Petroff, and Jelena Vučković. Resonant Excitation of a Quantum Dot Strongly Coupled to a Photonic Crystal Nanocavity. *Physical Review Letters*, 104(7):1–4, February 2010.

[100] S Ates, SM Ulrich, A Ulhaq, and S Reitzenstein. Non-resonant dot–cavity coupling and its potential for resonant single-quantum-dot spectroscopy. *Nature*, 3(November), 2009.

[101] Martin Winger, Thomas Volz, Guillaume Tarel, Stefano Portolan, Antonio Badolato, Kevin Hennessy, Evelyn Hu, Alexios Beveratos, Jonathan Finley, Vincenzo Savona, and Ataç Imamoğlu. Explanation of Photon Correlations in the Far-Off-Resonance Optical Emission from a Quantum-Dot–Cavity System. *Physical Review Letters*, 103(20):207403, November 2009.

[102] Zhiliang Yuan, Beata E Kardynal, R Mark Stevenson, Andrew J Shields, Charlene J Lobo, Ken Cooper, Neil S Beattie, David a Ritchie, and Michael Pepper. Electrically driven single-photon source. *Science (New York, N.Y.)*, 295(5552):102–5, January 2002.

[103] Silvia Vignolini, Francesco Riboli, Francesca Intonti, Diederik Sybolt Wiersma, Laurent Balet, Lianhe H. Li, Marco Francardi, Annamaria Gerardino, Andrea Fiore, and Massimo Gurioli. Mode hybridization in photonic crystal molecules. *Applied Physics Letters*, 97(6):063101, 2010.

[104] Silvia Vignolini, Francesco Riboli, Diederik Sybolt Wiersma, Laurent Balet, Lianhe H. Li, Marco Francardi, Annamaria Gerardino, Andrea Fiore, Massimo Gurioli, and Francesca Intonti. Nanofluidic control of coupled photonic crystal resonators. *Applied Physics Letters*, 96(14):141114, 2010.

[105] Kirill a Atlasov, Karl F Karlsson, Alok Rudra, Benjamin Dwir, and Eli Kapon. Wavelength and loss splitting in directly coupled photonic-crystal defect microcavities. *Optics express*, 16(20):16255–64, September 2008.

Acknowledgements

Here, I want to express my gratitude to and acknowledge the people who supported me in my scientific work culminating in this thesis. Additionally, I want to thank everyone who made the time while working on this project so much worthwhile.

- Foremost, I want to thank my adviser Dr. Hubert Krenner. His advice and guidance have been invaluable. Thank you Hubert for numerous prolific discussions, inputs and for giving me the opportunity to present my work at various conferences.

- I want to thank Prof. Dr. Achim Wixforth. I was lucky to receive his support throughout my time as diploma and PhD student working at his chair. His chair's conception allowing me to work efficiently and independently is highly appreciated. His excellent connections within the scientific community have been imperative.

- During my time at UCSB I was guest of the chair of Prof. Dr. Pierre Petroff. Thank you Pierre for taking me in and providing me with everything necessary. I enjoy remembering our discussions at lunch on the UCen lagoon-view terrace.

- Prof. Dr. Dirk Bouwmeester for giving me access to his optics lab at UCSB.

- A huge 'Thank You!' goes to Susanna Thon. Susanna was my main contact at UCSB. Thank you Susanna for your time, help and advice regarding FDTD simulation and PCM processing.

- I want to thank the members of the Bouwmeester group and the Petroff group for their support. I want to thank Tuan-Anh Truong and Hychoul Kim for the growth of the wafer material in the MBE lab at UCSB. Thank you Victor Brasch for being such a good friend!

- I want to thank my fellow members of Hubert's optics group for their collaboration during my PhD and while sharing lab time and space. Special thanks go to Jörg Kinzel and Marcin Malecha for their advice regarding Ebeam lithography and Stephan Kapfinger for his support setting up the fast photon detector.

- I want to acknowledge the help and support of the chair's technical staff providing the fundamental prerequisites regarding the IT, lab and cleanroom infrastructure.

- Thank you my fellow office members for a great and inspiring time. The polarizing discussions on and off scientific topics are a much cherished memory. Thank you Andreas Hartmann, Benjamin Eggart, Dominik Breyer, Florian Strobl, Judith Seibert, Marcin Malecha!

- I want to thank the cluster of excellence Nanosystems Initiative Munich (NIM) for their graduate program allowing me to establish a network with many PhD-student. I also wanted to acknowledge the support I received via the NIM-Seed-Funding.

- I want to thank the organizers and PIs of NIM for the opportunity to plan and organize many activities and events it hands to the members of its graduate program via the elected student board. It was an important and valued experience being a member of this board. Thanks to my fellow student board members Benjamin Eggart, Hubert Krammer, Frauke Mickler and Max Scheible for a great time.

- I want to thank the Bayerischen Forschungsstiftung and acknowledge the fundamental support I received as a scholar.

- I want to thank the Bavaria California Technology Center (BaCaTeC) for the funding and support received.
- I want to thank my family for the love and support they extend towards me.
- Most importantly, I want to thank my wife Michaela. You make everything better!